ADVANCED OPTICAL MATERIALS
www.advopticalmat.de

Chirality and Chiroptical Effects in Metal Nanostructures: Fundamentals and Current Trends

*Joel T. Collins, Christian Kuppe, David C. Hooper, Concita Sibilia, Marco Centini, and Ventsislav K. Valev**

Throughout the 19th and 20th century, chirality has mostly been associated with chemistry. However, while chirality can be very useful for understanding molecules, molecules are not well suited for understanding chirality. Indeed, the size of atoms, the length of molecular bonds and the orientations of orbitals cannot be varied at will. It is therefore difficult to study the emergence and evolution of chirality in molecules, as a function of geometrical parameters. By contrast, chiral metal nanostructures offer an unprecedented flexibility of design. Modern nanofabrication allows chiral metal nanoparticles to tune the geometric and optical chirality parameters, which are key for properties such as negative refractive index and superchiral light. Chiral meta/nano-materials are promising for numerous technological applications, such as chiral molecular sensing, separation and synthesis, super-resolution imaging, nanorobotics, and ultra-thin broadband optical components for chiral light. This review covers some of the fundamentals and highlights recent trends. We begin by discussing linear chiroptical effects. We then survey the design of modern chiral materials. Next, the emergence and use of chirality parameters are summarized. In the following part, we cover the properties of nonlinear chiroptical materials. Finally, in the conclusion section, we point out current limitations and future directions of development.

1. Introduction

Any pair of shapes, or any two arrangements of points, that are mirror images of each other but cannot be superimposed on each other are called "chiral".[1] Chirality is ubiquitous throughout the universe and can be observed at widely different scales: from the shape of galaxies all the way down to sub-atomic particles. In living organisms, chirality is essential and constitutes an important feature of body shapes, organs, tissue and molecular configurations. In order to distinguish them, the two separate entities within a chiral pair are referred to as left-handed and right-handed; this is because the word "chirality" itself derives from a Greek word meaning "the hand". Furthermore, for conciseness, "a pair of chiral molecules" is designated as "enantiomers". Enantiomers have practically the same energy levels with only tiny differences that are due to an effect of the weak force; yet they can have widely different properties.

In living organisms, chirality is widespread, often plays a significant role and, in some instances, it can be of vital importance. In the animal world, the coloration of several butterfly wings (e.g., of species Parides sesostris and Teinopalpus imperialis)[2] and of beetle exoskeletons (Chrysina gloriosa)[3] is due to chiral photonic crystals. Among plants, the Pollia condensate fruit also owes its iridescent colors to chiral gyroid photonic crystals.[4] An amusing example of chirality is that, while one handedness of limonene smells of lemon, the other smells of oranges. Such differences in smell can have important consequences, as in the case of the fruit fly pheromone olean, where one handedness attracts females and the other attracts males.[5] Chirality is also crucial for pesticides. The molecules mecoprop and dichlorprop are components of many commercial weed killers, however only one handedness of each is the herbicide; the other handedness is inactive.[6] Moreover, for the pharmaceutical industry, chirality can be vital. The drug Thalidomide has become tragically famous because one enantiomer is effective as relief medication for morning sickness in pregnant women, while the other causes severe birth defects.[7] Other examples include Naproxen, an effective anti-inflammatory drug, whose mirror image causes liver poisoning;[8] Levodopa, used to treat Parkinson's disease, whose mirror image affects the blood and leads to chronic bacterial infection;[9] Penicillamine, used to treat arthritis, whose mirror image is a neurotoxic;[10] Ketamine, an active anaesthetic, whose mirror image causes hallucinations; Methorphan, a cough suppressant, whose mirror image is an opioid narcotic drug; Ethambutol, effective for treating tuberculosis, though its mirror image causes

J. T. Collins, C. Kuppe, D. C. Hooper, Dr. V. K. Valev
Centre for Photonics and Photonic Materials and Centre for Nanoscience and Nanotechnology
Department of Physics
University of Bath
Claverton Down, Bath BA2 7AY, United Kingdom
E-mail: v.k.valev@bath.ac.uk
Prof. C. Sibilia, Dr. M. Centini
Universita' di Roma "La Sapienza"
Dip. di Scienze di Base e Applicate per l'Ingegneria (SBAI)
Via A. Scarpa 16, 00161 Roma, Italy

DOI: 10.1002/adom.201700182

blindness. In all of these cases, the importance of chirality can be traced down to a fundamental property of life itself. All the functional amino acids (building blocks for proteins) in living organism are chiral. Moreover, they all have the same chirality in humans, animals, plants and bacteria alike. The same is true for sugars, including deoxyribose, which gives its name to the deoxyribonucleic acid, also known as DNA. The difference is that while amino acids are all left-handed, sugars are all right-handed. This tendency of life to have evolved on the basis of a single chirality is referred to as "homochirality". Currently, the homochirality of life is regarded as a necessary mechanism for achieving efficient biochemistry of life; a mechanical equivalent would be the invention of a standard screw for the development of efficient manufacturing. However, the exact process by which homochirality evolved is still unclear and it is considered one of the most prominent scientific questions of all, since it is intrinsically linked to the very origin of life.[11] One of the most promising interactions that could have resulted in homochirality is the interaction between molecules and circularly polarized light in order to achieve enantiomeric excess.[12,13] Even a small enantiomeric excess could have been sufficient, if followed by auto-amplification.[14,15] In order to determine the likelihood of this mechanism, it is necessary to thoroughly understand the interaction between molecules and circularly polarized light.

Chiroptical (chiral-optical) effects were discovered in 1848, by Pasteur,[16] who studied two types of tartaric acid crystals "that look at each other in the mirror". From the works of Aragot, Herschel and Biot, it was already known that such crystals can rotate the direction of polarization of light in opposite directions. Pasteur observed the same to be true for dissolved crystals and deduced that the constitutive molecules must have the same property as the crystals, i.e. they are mirror images. In 1850, a commission headed by Biot confirmed Pasteur's findings.[17] The observed phenomenon of optical rotation was said to occur in materials that are "optically active". For historic reasons, "optical activity" is sometimes used synonymously with "optical rotation", which can be confusing since optically active materials can exhibit other chiroptical effects and sometimes no optical rotation at all. In this review, we will use the term "chiroptical effects" synonymously with "optical activity" in the most general sense of the latter.

Nowadays, chiroptical effects are largely used to characterize the chirality of molecules. In particular, they serve to estimate the level of chiral purity of enantiomers for pharmaceuticals, agrochemicals, fragrances and food additives. In this review, we present an overview of several linear chiroptical effects, such as optical rotation, circular dichroism, Raman optical activity and vibrational optical activity. We also take a look at some of the second harmonic generation (SHG) chiroptical effects, such as SHG circular dichroism, SHG optical rotation and SHG linear difference. Nevertheless, it should be pointed out that there are other, higher order, chiroptical effects that are based, for instance, on sum/difference frequency generation, on third harmonic generation and on higher order harmonic generation. Here, we limit the discussion to SHG, because it is the first nonlinear optical term in the higher harmonic expansion and it is often the largest nonlinear optical effect.

Molecular chiroptical interactions are usually small, largely due to the difference in scale between the chiral pitch of molecules and the wavelength of light. Recently, plasmonics has enabled the confinement of light to the nanoscale, which has resulted in dramatically increased chiroptical interactions. The research field of plasmonics is based on the study of surface plasmon resonances. The latter are coherent collective excitations of free electrons that occur at the interface between two materials, where the real part of the permittivity changes sign. Typically, such resonances are observed at metal-dielectric interfaces. In metal nanoparticles (NPs), the electrons are confined and yield localized surface plasmon resonances; whereby free electrons at the surface of the NPs are displaced in response to the force from the electric field of light. Consequently,

Joel T. Collins obtained his M.Phys. degree in 2015 from the University of Southampton. He is currently pursuing a Ph.D. in the Centre for Photonics and Photonic Materials at the University of Bath, under the supervision of Dr. Ventsislav Valev. His current research interests include linear and second-order nonlinear chiroptical effects in both nano- and meta- materials.

Christian Kuppe graduated with an M.Phys. degree at the University of Bath in 2015. Under the supervision of Dr. Ventsislav Valev, he is now pursuing his Ph.D. His research interest lies in the plasmonic enhancement of the optical activity of chiral molecules combined with periodic quasi-planar nanostructures.

Ventsislav K. Valev is a Research Fellow of the Royal Society and Reader in the Department of Physics, at the University of Bath, UK, where he heads the MultiPhoton NanoPhotonics group. Prior to taking up this post, he was a Research Fellow in the Cavendish Laboratory, at the University of Cambridge. He received his Ph.D. in 2006 from Radboud University Nijmegen in the Netherlands. His research focusses on the application of chiral plasmonic nano/metamaterials to achieve enhanced chiroptical effects, especially in nonlinear optics.

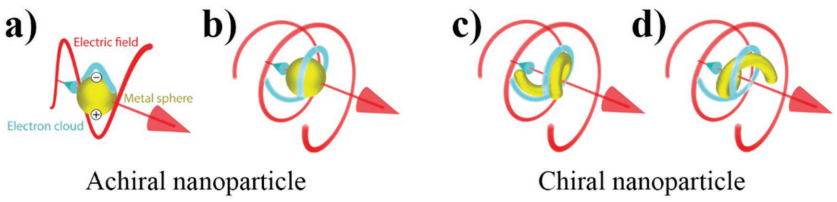

Figure 1. a) Linearly polarized light causes localized resonant plasmon oscillations at the surface of a metal nanosphere. b) For circularly polarized light the surface plasmons follow a helix. c) A chiral nanoparticle's shape can accommodate the plasmonic helix generated by CPL, yielding strong chiroptical interaction. d) An unphysical mismatch between the shape of the nanostructure and the ideal plasmonic helix, by contrast, yields a weak chiroptical interaction. Adapted with permission.[344] Copyright 2016, Optical Society of America.

the electron cloud oscillates at the frequency of light and, depending on the size of the NPs, their material and the surrounding medium, a resonance can be achieved, see **Figure 1**a. At resonance, energy is stored in the NPs leading to strong enhancements of the local electromagnetic fields, which in turn can benefit molecules.

Figures 1 provides an intuitive understanding to the chiroptical interaction between light and chiral plasmonic nanoparticles. Upon changing the polarization of incident light from linear to circular, the surface electrons on a spherical gold NP follow a helical path that is counter-propagating to that of the electric field of light, see Figure 1b. A chiral, helix-shaped NP of a matching handedness could accommodate the path of the electron helix, as in Figure 1c. However, as the unphysical illustration of Figure 1d indicates, the chiral helix-shaped NP of opposite handedness would be mismatched with the would-be ideal electron helix. The difference in interactions, schematized in Figure 1c and Figure 1d, yields a circular dichroism effect.

Chiral metal NPs have attracted a lot of interest because they offer a range of potential applications to nanotechnology, in general, and to nanophotonics in particular. These applications include chiral sensing and catalysis,[18,19] nanorobotics,[20,21] and optical components. The latter comprise super- and metalenses,[22] circularly polarized light polarizers and absorbers,[23] as well as miniaturized advanced optical components.[24] Such optical components would be useful for light processing using circularly polarized light, which could in turn find applications in spintronics[25] and quantum-optical computing.[26,27] Two key phenomena that have been associated with chiral metal NPs are negative refractive index and superchiral light. While the former derives from the possibility to tune the geometric chirality parameter in these NPs, the latter derives from the possibility to tune the optical chirality parameter. Both phenomena are briefly presented in this review.

Chirality and chiroptical effects in metal nanostructures have attracted considerable interest in recent years, with many potential applications in diverse areas of industry. A major driving force for their development is the progress of nanofabrication. Modern nanofabrication allows chiral metal NPs to tune geometric and optical chirality, which are key for negative refractive index materials and superchiral light. The field is growing quickly and has branched out into numerous noteworthy areas of research. There have been several recent reviews focusing on various aspects of ongoing exploration.[28–39] Our goal here is to outline four main areas of research interest, which are linear chiroptical effects, design of chiral materials, chirality parameters and nonlinear chiroptical effects. Within these areas, we then identify current trends that we believe are of particular promise. These trends are: surface-enhanced Raman optical activity, nanoparticle systems, planar chiral systems, multilayered chiral systems, three-dimensional chiral networks, helical materials, DNA materials, extrinsic chirality, magnetochiral materials, superchiral light, negative refractive index, chiral optical forces and nonlinear chiroptical materials. This list is not exhaustive and other interesting research trends include, but are not limited to, toroidal chirality,[40,41] nanorobotics,[21,42–45] and quantum dot research.[46–48]

2. Linear Chiroptical Effects

2.1. Optical Activity

Optical activity (OA) is associated with all phenomena accompanying the difference in the interaction of a chiral medium with left circularly polarized (LCP) and right circularly polarized (RCP) light.[49] The measured signal associated with OA is often referred to as a chiroptical (chiral optical) response. Molecular chirality is a fundamental property of molecules that is due to geometry. As chirality is due to the geometry of the sample, symmetry arguments can be applied to differentiate the chirality.[50,51] Optical activity is further differentiated into the two "classical" types electronic OA (EOA) and vibrational OA (VOA).[49] EOA is associated with electronic transitions in the visible and ultraviolet (UV) spectrum,[51–53] while VOA refers to vibrational transitions, that occur in the infrared spectral region.[54,55]

2.2. Electronic Optical Activity

2.2.1. Optical Rotation

Optical rotation (OR) refers to a rotation of the plane of polarized light due to an interaction with a chiral medium.[56–58] It is a phenomenon similar to linear birefringence. In the case of linear birefringence, a difference in the phase velocity of light can be observed along two crystallographic directions of propagation for linearly polarized light. In the case of OR, a difference in the phase velocity of light can be observed for left and right circularly polarized light, hence the effect is also referred to as circular birefringence.[56,58,59]

On the microscopic level, infinitesimal rotations of the plane of polarized light can be observed for both chiral and achiral materials, however in the achiral case the statistical net effect is zero. The reason for this is based on the symmetry of achiral media, as every infinitesimal rotation by symmetry has an associated anti-rotation. In a chiral medium, the symmetry is broken and therefore these small rotations accumulate and result in a measurable rotation of the plane of polarized light.

Here, we can assume that the incident electromagnetic (EM) wave is linearly polarized and is transmitted by an optically active medium. In this case, we can represent linearly polarized light as a combination of two circularly polarized waves. Furthermore, we assume that the optically active medium has a refractive index that is different for RCP and LCP light, but the extinction coefficient is the same for both. The refractive index can be described by $n = c/v_p$, where c is the speed of light and v_p is the phase velocity. Therefore, a difference in the refractive index for LCP and RCP light can only be due to a change in the phase velocity. While the phase for LCP and RCP light is different, the amplitude remains the same. The resulting wave is visualized in **Figure 2**a. Propagating through the optically active medium, LCP (σ^-) and RCP (σ^+) light have different angular velocities; here σ^- is slower than σ^+. The difference in angular velocity is called retardation and, upon exiting the material, the resulting wave is rotated by an angle ϕ with respect to the vertical direction. This angle measures the optical rotation in degrees or radians.[60,61]

Circularly polarized light can also be represented by a set of linear waves

$$\left[\begin{cases} E_x^- = A\cos(kz-\omega t) \\ E_y^- = -A\sin(kz-\omega t) \end{cases} \begin{cases} E_x^+ = A\cos(kz-\omega t) \\ E_y^+ = A\sin(kz-\omega t) \end{cases}\right], \tag{1}$$

where E_x and E_x are the x- and y-components of the electromagnetic wave, in a three dimensional coordinate system in which the wave is propagating in the z-direction, for left (–) and right (+) circular polarization, A is a constant amplitude, k is the wave number, z the direction of propagation, ω the angular frequency and time t.

The refractive index can be expressed as the average of the refractive index for right (+) and left (–) circularly polarized light, so that

$$n = \frac{c}{v_p} = \frac{ck}{\omega} = \frac{n^+ + n^-}{2}. \tag{2}$$

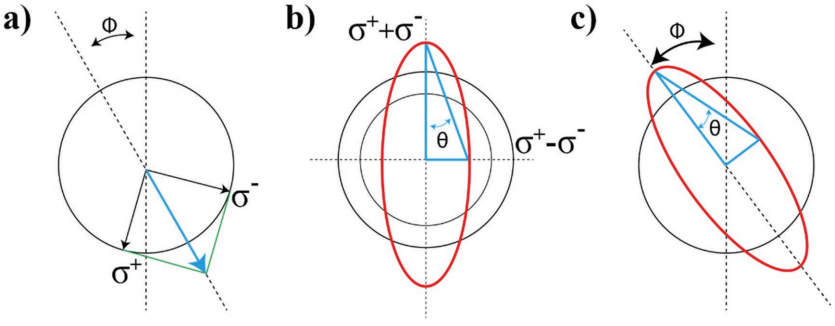

Figure 2. Schematics of a) optical rotation with left (σ^-) and right (σ^+) circularly polarized light propagating with different phase velocities in the optically active medium. As a result, the plane of polarization of the transmitted wave is rotated by an angle Φ. In (b), the phenomenon of circular dichroism is shown. As within the chiral material, the extinction coefficient for LCP (σ^-) and RCP (σ^+) light are different, upon exiting the material, the electric field of the transmitted wave describes an ellipse (red), with an angle of ellipticity θ (blue). In the general case both optical rotation and circular dichroism happen simultaneously, which is shown in (c).

Rearranging (1) and applying (2), then combining x- and y-components results in the following expression for the optical rotation ϕ

$$\tan(\phi) = \frac{E_x}{E_y} = \frac{2A\cos\left[\frac{\omega}{c}(nz-ct)\right]\cos\left[\frac{\omega}{2c}(n^+-n^-)z\right]}{2A\cos\left[\frac{\omega}{c}(nz-ct)\right]\sin\left[\frac{\omega}{2c}(n^+-n^-)z\right]} = \tan\left[\frac{\omega}{2c}(n^+-n^-)z\right], \tag{3}$$

with

$$\phi = \frac{\omega}{2c}(n^+-n^-)z = \frac{\pi}{\lambda}(n^+-n^-)l, \tag{4}$$

where ϕ is expressed in radians, λ is the wavelength of the EM wave, and l is the length of the medium travelled through by light.

The refractive index of a medium is generally wavelength-dependent, i.e. dispersive, and therefore the differential refractive index, i.e. $n^+ - n^-$ is also wavelength-dependent. The wavelength-dependent change in OR (i.e., the OR spectrum) is defined as optical rotatory dispersion (ORD).[49,62]

2.2.2. Circular Dichroism

Whereas OR is sensitive to the geometric arrangement of the electromagnetic field, on the molecular or nanostructure level, CD is sensitive to chirality in energy transitions. The two effects are complementary.[49] In the case of OR spectra, the refractive index affects the phase velocity of LCP (σ^-) and RCP (σ^+) light differently, while the extinction coefficient is the same for both. For the case of CD, the phase velocities of LCP and RCP light are the same, while the extinction coefficient is different, as is shown in Figure 2b. The difference in the extinction coefficient leads to different amplitudes for LCP and RCP light. The result is that the electric field vector of light describes an ellipse in the plane perpendicular to the direction of propagation. The ellipticity θ representing the typical measure of CD is given in degrees. This is a result of unit conversion rather than direct measurement, as commercial CD spectrometers usually do not measure the ellipticity directly.[49]

Mathematically, the ellipticity is given by the following relation

$$\tan(\theta) = \frac{|\sigma^+| - |\sigma^-|}{|\sigma^+| + |\sigma^-|}. \tag{5}$$

Most CD experiments measure differences in intensities, so Equation (5) must be rearranged to be in terms of left (–) and right (+) circularly polarized light (CPL) intensities (I^- and I^+, respectively), which can be expressed as

$$\tan(\theta) = \frac{\sqrt{I^+} - \sqrt{I^-}}{\sqrt{I^+} + \sqrt{I^-}}. \tag{6}$$

In the small angle approximation, this reduces to

$$\theta = \frac{\sqrt{I^+} - \sqrt{I^-}}{\sqrt{I^+} + \sqrt{I^-}}. \tag{7}$$

OR and CD are both expressions of the optical activity of a material and both are routinely used in characterizing chiral materials.[50]

In the general case both the extinction coefficient and refractive index would be different for LCP and RCP light, which leads to the simultaneous occurrence of OR and CD. The resulting wave is schematically shown in Figure 2c. In the early 1960s, Moscowitz found that OR and CD are strongly correlated. This was later formalized in the Kramers-Kronig relation, as in Equation (8), owing to the fact that OR and CD relate to the real and imaginary parts of the complex refractive index, respectively:[49]

$$\begin{aligned}\left[\phi(\omega)\right] &= \frac{2}{\pi} PV \int_0^\infty \frac{\omega' \left[\theta(\omega')\right]}{\omega'^2 - \omega^2} d\omega' \\ \left[\theta(\omega)\right] &= -\frac{2\omega}{\pi} PV \int_0^\infty \frac{\left[\phi(\omega')\right]}{\omega'^2 - \omega^2} d\omega\end{aligned} \tag{8}$$

where ω' is the excitation frequency and PV denotes the Cauchy principal value of the integral.[62] Using these formula, it is possible to obtain the ORD from measuring the spectrum of CD and vice versa.

2.3. Localized Surface Plasmon Resonances

Surface plasmons are observed at the interface between a pair of materials where the real part of the permittivity changes sign across the interface.[63] Typically, such pairs are made of dielectrics (often air, water, various solvents, various polymers, etc.) and metals (often Au, Ag, Cu or Al). Metals are not always necessary though as graphene, semiconductors, and doped quantum dots can also support surface plasmons.[64] When the surface plasmons are confined within a nanoparticle of diameter smaller than the wavelength of light, they are referred to as localized surface plasmons. The latter represent coherent oscillations of the surface electrons that can be driven by the electric field of light. At a given wavelength, these oscillations can reach a resonance, depending on the size of the nanostructures, their material constitution, their geometry, their surroundings and their distance from each other. For noble metals, the resonance is situated in or near the visible part of the electromagnetic spectrum, which makes them attractive for color-changing applications. At resonance, the nanoparticles store energy in the form of strong electromagnetic near-fields; correspondingly strong absorption and scattering can be observed. In Mie's theory, for a spherical nanoparticle this light-matter interaction is characterized by the extinction coefficient:

$$C_{ext} = \frac{24\pi^2 R^3 \varepsilon_m^{3/2} N}{\lambda \ln(10)} \frac{\varepsilon_i}{(\varepsilon_r + 2\varepsilon_m)^2 + \varepsilon_i^2} \tag{9}$$

where R is the radius of the nanoparticle, such as $R/\lambda \ll 1$ (with λ wavelength of light). N is the electron density, ε_m is the dielectric constant (relative permittivity) of the surrounding medium and $\varepsilon = \varepsilon_r + i\varepsilon_i$ is the complex permittivity of the bulk metal. It can be seen that, for a spherical nanoparticle, the resonance condition is $\varepsilon_r = -2\varepsilon_m$, i.e., the permittivity changes sign across the interface.

The resonance condition is also clearly seen in the polarizability of the nanoparticle at a given wavelength:

$$\alpha(\lambda) = 4\pi\varepsilon_m(\lambda) R^3 \frac{\varepsilon(\lambda) - \varepsilon_m(\lambda)}{\varepsilon(\lambda) + 2\varepsilon_m(\lambda)} \tag{10}$$

This polarizability is an expression of the idea that the surface electrons are driven by the electric field of light. Because the permittivity is wavelength-dependent, the formula yields plasmonic and chiroptical spectra depending on the nanoparticle geometry.

For non-spherical nanoparticles, the resonance condition becomes $\varepsilon_r = -\chi\varepsilon_m$, where χ is the shape factor, which is equal to 2 in the case of a sphere and increases with the aspect ratio. For chiral nanoparticles, the shape factor includes an achiral term $\overline{\chi}$ and chiral term $\delta\chi_R = -\delta\chi_L$ corresponding to right (R) and left (L) handed nanostructures. For a spherical chiral plasmonic nanoparticle the extinction coefficient becomes then:[65]

$$C_{ext}^{\pm} = \frac{24\pi^2 R^3 \varepsilon_m^{3/2} N}{\lambda \ln(10)} \left(\frac{\varepsilon_i}{\left[\varepsilon_r + \left(\overline{\chi} \pm \delta\chi_{D/L}\right)\varepsilon_m\right]^2 + \varepsilon_i^2} \right) \tag{11}$$

where + and − denote RCP and LCP, respectively, and the CD effect is proportional to $C_{ext}^- - C_{ext}^+$. Mie's theory was extended by Bohren to calculate expressions for CD and OR in an optically active sphere.[66] Nowadays, these quantities are usually calculated with the help of Maxwell equations' solvers, such as MAGMAS,[67,68] Lumerical,[69] MEEP,[70] RSoft's DiffractMOD,[71] etc.

Physically, in molecules, OR is related to the spatial variation of the electromagnetic fields of light at the length scale of the molecules. Due to the large difference between the wavelength of light and the chiral pitch of the molecules, molecular chiroptical effects are usually very weak. In the case of plasmonic nanoparticles though, light is effectively confined to the nanoscale, with the plasmon wavelength being much shorter than the wavelength of light. Consequently, the plasmonic chiroptical effects achieve a much better match between chiral pitch of the nanostructure and electromagnetic wavelength, which results in much stronger chiroptical effects. For similar reasons, we can intuitively understand that the confinement of light to plasmonic nanostructures can also benefit the OR of molecules near plasmonic nanoparticles, though the actual molecule-nanoparticle interactions are significantly more complex.[30]

For its part, in molecules, CD is related to different absorption of LCP and RCP and it is most pronounced near molecular energy transition levels. As we have seen in Figure 1, the case of the plasmonic nanostructures is analogous, with strong CD often observed at the wavelength that satisfies the resonance condition.[72]

In the next section, we will see how other plasmonic effects, namely hybridization can lead to bisignate chiroptical responses.

2.4. Bisignate Nature of Optical Activity

Chiroptical effects change sign over the wavelength spectrum of incident light, often several times, frequently resulting in bisignate regions, where a negative peak is observed close to a positive peak.[73] For instance, close to excitation frequency resonances, where CD is usually strongest, it is observed that the optical rotation changes sign. This particular sign change is known as the Cotton effect.[74,75] It originates from the Kramers-Kronig relationship between CD and OR. For an intuitively appealing image, we can consider a driven mechanical oscillator near resonance. At the lower energy side of the resonance, the oscillations are in phase with the driving force. At the higher energy side of the resonance, the oscillations are out of phase with the driving force. It can be seen that, at resonance, the amplitude of the oscillations is large and the phase undergoes a sharp 180° transition. CD and OR can be seen as analogous to the amplitude and phase of the oscillator because CD is related to the extinction coefficient and OR is related to the phase velocity for circularly polarized light. It is therefore not surprising that when the CD is maximum, the OR undergoes a sharp variation.

The bisignate nature of optical activity was highlighted in 1930, when Kuhn stated a sum rule that requires the value of optical activity to be zero when integrated over the full spectrum of available resonances.[76] Kuhn considered a mechanical model for molecular bonds, where two linear oscillators are positioned perpendicularly and on top of each other. When the resonators are coupled, each experiences a small force from the other. As a consequence, the resonances of both oscillators shift, due to the coupling term. For two oscillators of different frequency, the sign of the optical activity in the first oscillator depends on whether the resonant frequency of the second oscillator is higher or lower. Naturally though, from the point of view of the second oscillator coupling to the first one, the situation is opposite. It follows that at the two resonance frequencies, the optical activities always have opposite sign. This principle can be extended to any number of coupled oscillators.

Bisignate CD is also observed in exciton-coupled chromophores.[77] For two identical chromophores, the dipole transitions can couple, resulting in an energy splitting of the transitions: the more energetically favorable state is represented by a spectral resonance at lower energy and the more unfavorable state leads to a spectral resonance at higher energy. For each resonance, the electric dipole of one molecule can couple to the magnetic dipole of the other molecule, which produces optical activity. For geometric reasons, the OA at both resonances are always opposite. As a consequence, the CD spectra of these exciton coupled chromophores are bisignate. Guerrero-Martinez et al.[78] pointed out that the bisignate line shape of the CD resulting from two coupled nanorods is strongly reminiscent of the exciton coupling response between two chromophores, albeit there is a difference in scale.

Fan and Govorov developed a model to explain the CD in plasmonic nanoparticles.[79] They studied various geometrical arrangements of plasmonic nanoparticles (NPs), such as a helices, tetramers, pyramids and tetrahedra. They remarked that the CD spectrum has both positive and negative bands (bisignate CD) and attributed this effect to the NP-NP Coulomb coupling in chiral nanoparticle assemblies. This coupling was thought to create preferentially left-handed collective plasmonic modes on one side of the plasmon resonance and right-handed modes on the other side.

Auguié et al. drew a parallel between exciton coupling in molecules and the coupling of two gold nanorods.[80] Their work extends the model proposed by Fan and Govorov by considering anisotropic NPs, i.e., nanorods. Each nanorod can then be idealized as a dipole, the couple forming a hybrid dimer. The hybridization results in an energy splitting of the two modes: parallel/symmetric/bright mode and antiparallel/anti-symmetric/dark mode. Coulomb interactions place the former mode at higher energy and the latter mode at lower energy. The difference in direction of the induced plasmonic displacement currents within the nanorods, between the two modes, results in opposite chiroptical behavior for the modes, i.e., bisignate CD.

2.5. Vibrational Optical Activity

Vibrational optical activity (VOA) is due to the differential response of a medium to LCP and RCP light at wavelengths corresponding to vibrational transitions, i.e., in the IR. Generally, there are two types of VOA, vibrational circular dichroism (VCD) and vibrational optical rotation. Although it is possible to use IR radiation to measure these effects, it is often more practical to make use of Raman optical activity (VROA or usually just ROA).[49] Vibrational transitions can be extremely complex depending on the molecule or molecular assembly in question. However, the principle of vibrational modes can be demonstrated with the methylene- end group (CH_2), which is common in organic compounds. If the covalent bonds are assumed to behave like springs, described by Hooke's Law, there are six possible vibrational modes, which are shown in **Figure 3**a.

VOA is sensitive to the vibrational modes of distinct groups, which are associated with the vibrational transition in the sample, providing three-dimensional structural information.

2.5.1. Vibrational Circular Dichroism

The VCD effect is based on different vibrational absorption for LCP and RCP electromagnetic waves. The excitation energy for vibrational transitions lies in the IR spectrum. In contrast to electronic CD, the photons are truly absorbed, causing non-symmetric vibration, as shown in Figure 3a. This causes a non-symmetric charge density distribution around the center, i.e., it induces a dipole moment of the sample. The VCD is therefore defined as the absorbance of LCP – RCP light for a molecule undergoing the transition from the zeroth (0) to the first (1) vibrational level of the ground electronic state g, such that the differential absorption ΔA is expressed as

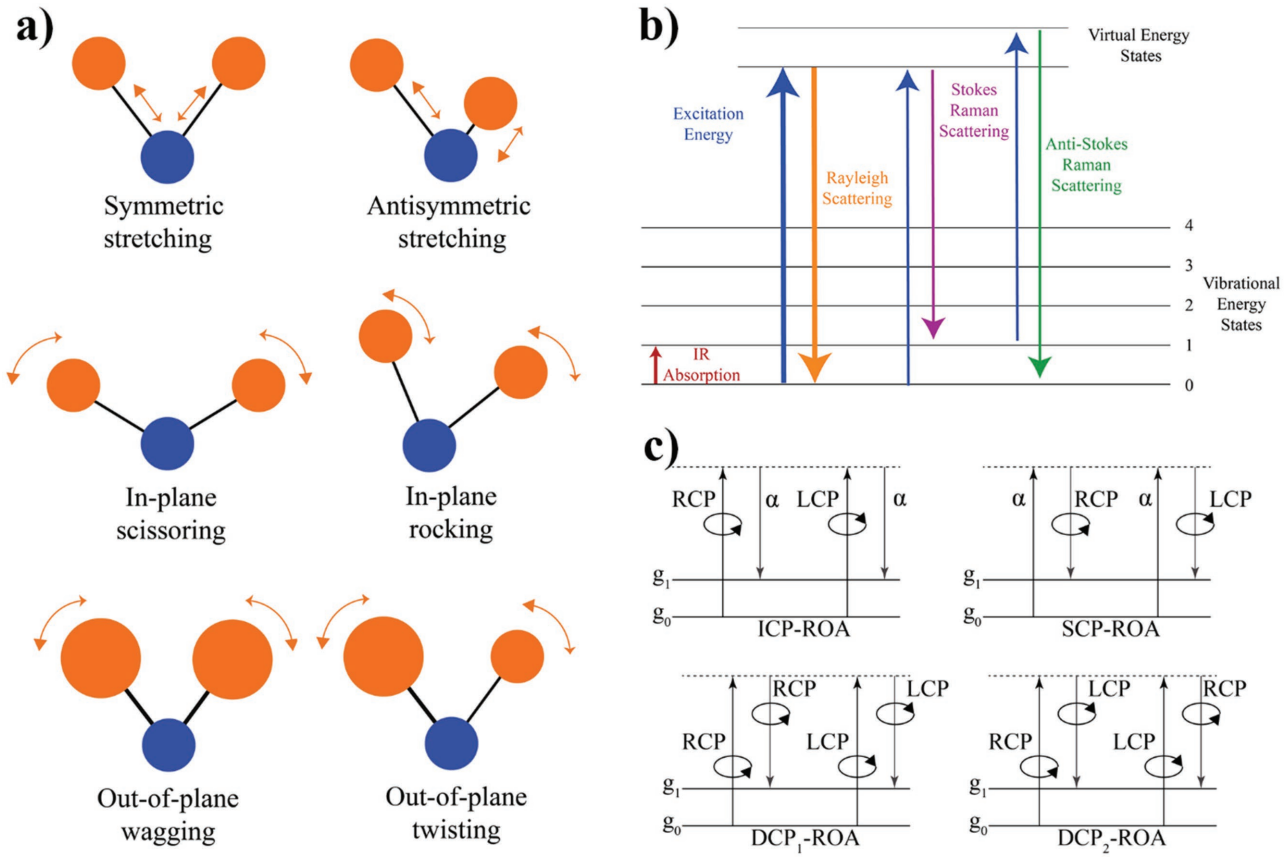

Figure 3. a) Vibrational modes of methylene group. b) Energy diagram showing the difference between Raman scattering and IR absorption. c) The four forms of Raman optical activity (ROA) measurements with CPL.

$$(\Delta A)^{a}_{g1,g0} = (A_L)^{a}_{g1,g0} - (A_R)^{a}_{g1,g0}. \quad (12)$$

In this definition, the total intensity of the vibrational transition with the label a (superscript) is measured. Experimentally, VCD is determined by measuring the differential absorption as a function of the radiation frequency, associated with each individual vibrational transition.[49]

2.5.2. Raman Optical Activity

Raman optical activity (ROA) is defined as the difference in Raman scattering for RCP and LCP light. The different kinds of scattering are visualized in Figure 3b. When a photon is scattered from an atom, this scattering can either be elastic (unchanged kinetic energy, changed direction) or inelastic (changed kinetic energy, changed direction). In the scattering process, the atom's vibrational state is excited by the absorption to a virtual energy state. If the re-emitted photon has the same energy, the photon is Rayleigh-scattered. In the much rarer case (every 1 out of 10^7 photons) the energy of this photon will be changed, as the molecule is undergoing a vibrational transition from the zeroth into the first vibrational state. This process is called Raman scattering. When the energy of the scattered photon is smaller than that of the incident photon, the process is called Stokes-scattering. When the energy of the scattered photon is larger than that of the incident photon, the process is called Anti-Stokes-scattering. The change in energy of the photon induces a vibrational transition, as shown in Figure 3a.

For ROA measurements the Stokes-scattering process is used, which leads to a red-shift of the scattered radiation. There are four types of ROA measurements, see Figure 3c. The initial and final states of the transitions are the same as for the VCD case, however there is a range of possible configurations. The original ROA measurement is called incident circular polarization (ICP) ROA. ICP- ROA uses an input beam modulated between equal amounts of LCP and RCP light, and measures either the linear polarized or unpolarized Raman intensity. The second form is called scattered circular polarization (SCP) ROA, which uses linear or unpolarized incident light and measures the differential Raman intensity for LCP and RCP light. The third form is in-phase dual circular polarization (DCP_1) ROA. Here both polarizations are switched simultaneously, i.e., for RCP light input, the Raman intensity for RCP light is measured. The fourth and last case is the out-of-phase dual circular polarization (DCP_2) ROA, where the measured Raman intensity is of opposite handedness with respect to the input beam.[49]

ROA measurements are linearly proportional to the input beam intensity and the molar concentration, which is often used to find the molecular cross-section ROA measurement.

Alternatively, in analogy to VCD the spectrum can be obtained by summing over all individual transitions.

2.5.3. Surface-Enhanced Raman Optical Activity

As early as 1983, Efrima showed how it is possible to combine surface enhanced Raman scattering (SERS) with ROA to achieve surface enhanced Raman optical activity (SEROA) for chiral molecules adsorbed onto a metal surface. This gave signals of the circular intensity difference (CID) one order of magnitude larger than regular Raman scattering. Mathematically CID is defined as

$$CID = \frac{I_R - I_L}{I_R + I_L}, \tag{13}$$

where I_R and I_L are the scattering intensity for incident RCP and LCP light, respectively.[81,82]

More recently, experimental proof of the advantage of SEROA was given, for example by Kneipp et al. who demonstrated improvement of signal-to-noise ratios upon measuring SEROA for adenine in a silver colloidal solution. The experiment addressed the difference of SERS, which measures the sum of LCP and RCP light intensities, and SEROA, which is a measure of the difference of LCP and RCP light intensities. The resulting values were nearly one order of magnitude larger than typical ROA measurements, in agreement with the earlier theoretical work on SEROA.[83]

In another example, Ostovar Pour et al. used the two enantiomers of ribose, forming a polyacrylic acid, to control colloid aggregation. They measured both enantiomers with ROA and SEROA and compared Raman and ROA spectra. According to the authors, this is the first experimental proof of SEROA, because the spectra for both enantiomers were recorded. It was also noted that control over the aggregation and various artefacts reduce the effect of plasmon resonance-induced changes in the CPL, which usually makes it difficult to interpret SEROA spectra.[84]

In order to reduce artefacts in the SEROA spectra, Sun et al. proposed remote excitation of ROA by illuminating Ag nanowires with laser light. The nanowires act as a waveguide and allow the light to be coupled into nearby nanoantennas, i.e., using an alternative method to achieve SEROA. The CID signal of the ROA was shown to be controllable by changing the input angle between the Ag nanowires.[85] This improvement method has further been addressed.[86]

Interest in SEROA is currently growing. Koktan et al. investigated Ag nanoparticles attached to supramolecular cysteine and its derivatives. They probed the adsorption of three different chiral compounds by means of SEROA. The spectra were used to determine the concentration of adsorbed molecules.[87] Additionally, Ostovar Pour et al. examined the protein-ligand binding via SEROA spectra in the vicinity of a plasmon resonance from an achiral metallic nanostructure. The authors observe a "chirality transfer" whereby the stereochemical response of a chiral analyte is transmitted to an achiral dye molecule, in proximity of an achiral metallic NP that is excited at the plasmon resonance. The authors probed different enantiomeric pairs with SEROA and observed the bisignate feature expected from OA behavior.[88]

3. Design of Chiral Materials

Although the variety of chiral designs that have been studied so far are very numerous, they have the common objective to exploit plasmonic enhancements of the chiroptical response. As described in Section 2.3, surface plasmons are collective excitations of the free electrons, commonly observed at metal-dielectric interfaces.[63] Recently, plasmonics has attracted a lot of research interest, chiefly because of the associated large electromagnetic field enhancements at the surfaces of nanostructures. Correspondingly, large chiroptical effects have been associated with plasmonic chiral nanostructures.[50] Although an ideal spherical nanoparticle is not chiral, real single nanoparticles can be chiral due to shape imperfections or crystalline order. In conjunction with chiral molecules, single plasmonic nanoparticles can exhibit enhanced chiroptical effects. In particular, these effects can be enlarged for chiral molecules upon bringing two plasmonic nanoparticles in close proximity; this results in concentrating the electromagnetic fields in the gap for an increased light-molecule interaction. Nanoparticles can both increase the chiroptical response of chiral molecules and yield an intrinsic chiroptical signal, for instance in the case of two plasmonically coupled nanorods. Similar intrinsic plasmonic chirality can be observed in systems consisting of larger number of nanoparticles that are arranged in chiral patterns. The increasing complexity of design yields a plethora of chiral plasmonic systems, which will be outlined in the following sections of this review.

3.1. Nanoparticle Systems

The chiroptical response of most chiral molecules is very weak and difficult to measure. The measurement usually requires large quantities of the molecules, as in the case of commercial CD spectrometers. An active area of research focuses on enhancing the natural chiroptical response of those molecules by combining them with nanoparticles (NPs), in various geometric configurations. Exploiting the plasmonic nature of some metallic nanoparticles, such as gold or silver, it has been shown that large enhancements of the chiroptical effects are achievable. Nanoparticle systems offer a variety of physical mechanisms by which the chiroptical response of molecules can be enhanced. Furthermore, the nanoparticles themselves can show pronounced and useful chiroptical properties.

3.1.1. Single-Nanoparticle System

The minor shape variations in single metal nanoparticles (diameter >10 nm) produced by chemical methods, are generally not sufficient to exhibit a measurable chiroptical response. They are therefore considered achiral. However, chiral molecules exhibit enhanced OA by benefiting from the plasmonic resonances of the NPs. One example of this is shown

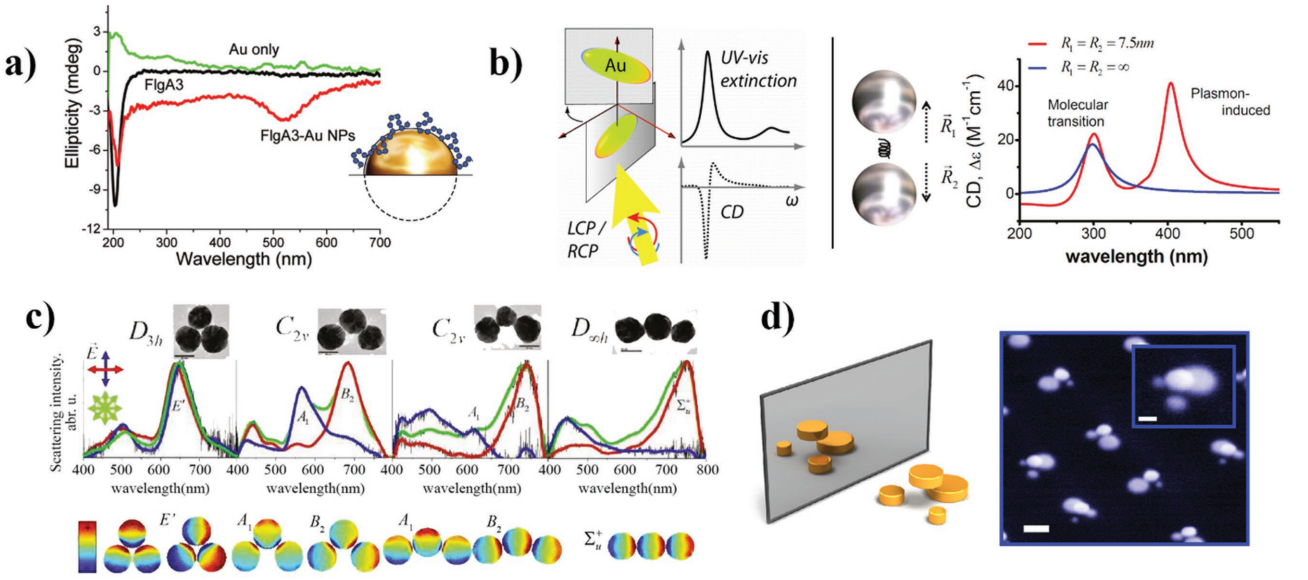

Figure 4. a) CD measurement for gold nanoparticle without (green) and with (red) chiral peptide in proximity, compared to just peptide (black) showing clear plasmonic enhancement of CD away from peak wavelength for peptide alone. Reproduced with permission.[53] Copyright 2011, American Chemical Society. b) Double-nanoparticle systems present two very significant aspects. In the left panel, a nanorod dimer is chiral and can yield plasmonic chiroptical effects. In the right panel, a nanoparticle dimer produces a strongly localized electromagnetic hotspot in the gap, where chiral molecules can experience enhanced interaction with light. (Left) Reproduced with permission.[80] Copyright 2011, American Chemical Society. (Right) Reproduced with permission.[94] Copyright 2011 American Chemical Society. c) (Top) Transmission electron micrographs of plasmonic nanoparticles in a trimer arrangement, with varying vertex angles. (Middle) Scattering intensity spectra for each vertex angle. (Bottom) Coupling of the plasmon modes between particles breaks the symmetry of the local electric field, resulting in a chiral system. Reproduced with permission.[97] Copyright 2011, American Chemical Society. d) Schematic representation (left) and SEM image (right) of tetramer chiral clusters. Reproduced with permission.[101] Copyright 2012, American Chemical Society.

in **Figure 4**a, where Slocik et al. used peptide ($FlgA_3$) as the chiral molecule (8.6 μM), combined it with gold nanospheres (1.14×10^{13} particles/mL), and investigated in the UV–vis spectral range.[53] In such a system, the resulting absorbance is greatly enhanced due to the gold NPs. The authors found that this leads to a decrease of the maximum CD signal at the characteristic frequency of the peptide. In contrast, close to resonance frequency of the gold NPs (525 nm), the CD is greatly enhanced. Such CD enhancements at plasmon resonance were also reported in silver NPs.[89]

The addition of plasmonic NPs into a chiral molecule's environment causes a shift in the characteristic peak in the CD signal of the isolated molecule. This is due to the chiral molecules forming chiral nanocomposites with the nanospheres. The control of the molecule's peak shift (either towards higher or lower frequencies) and of the plasmonic peak with respect to different degrees of chiral ordering was studied by Govorov's group, and by Oh et al.[29,90,91]

Furthermore, the mechanisms that govern the change of the CD spectrum of chiral molecules, when combined with achiral metal NPs, were described by Govorov et al.[52] The authors used gold as well as silver NPs, in combination with chiral molecules, to investigate the difference in the plasmon-induced change in the CD spectrum. They identified two main mechanisms responsible – the first is a plasmon-induced change of the electromagnetic field inside the chiral molecule. The second is due to the optical absorption of the NP-molecule complex, due to chiral currents inside the metal NP, which are induced by the dipole of the chiral molecule.

Fan and Govorov studied single nanocrystals (NCs) in various shapes. Their theoretical analysis was based on the Drude model with narrow plasmonic lines. The authors state that a large plasmonic damping constant leads to a merging of the plasmonic lines and the formation of the bisignate spectrum typical for chiroptical effects. This effect only appears for chiral shapes. This is physically explained by chiral surface distortions - the more distorted the shape the greater the splitting and the stronger the chiroptical effect.[92]

3.1.2. Two-Nanoparticle System

Often referred to as "dimers", two-nanoparticle systems possess two main aspects that are relevant to chiroptical effects.

First, as shown in the left panel of Figure 4b, two nanorods can couple plasmonically to form a chiral entity. This is achieved when the nanorods are in close proximity and are rotated with respect to each other at an angle that is different from 0° (and multiples of 90°). Auguié et al.[80] demonstrated that the plasmonic interaction in such nanorod dimers is analogous to energy level hybridization and leads to a bisignate response (see Section 2.4). Wang et al.[93] also studied the effect experimentally and theoretically. The authors investigated circular differential scattering (CDS), which measures the difference in scattered light for LCP and RCP light, and CD using dark field microscopy. The dimers consisted of equally sized gold nanorods (homodimer) with varying twist angles. It should be noted that chirality can be introduced in another way, by

using a size-mismatch between nanorods (heterodimer). Both hetero- and homodimers yield a clear CD signal, although only heterodimers showed the conventional bisignate line shape described in Section 2.4.

Second, plasmonic dimers can efficiently concentrate the electromagnetic fields into the gap regions achieving local field enhancements that are orders of magnitude stronger than those of single-nanoparticles, see the right panel in Figure 4b. Govorov theoretically investigated the plasmon-induced CD of a chiral molecule in the proximity of metal nanocrystals. Figure 4b (right) shows the author's findings using silver dimers with a chiral molecule in between them, varying the effect of the distance between the dimers. They found strong enhancements of the CD signal for inter-particle separations smaller than the wavelength of light. In this case, the dimer induces an enhancement of the CD based on the molecular transition and further produces a plasmon-induced CD peak at the resonance frequency of the silver NPs.[94]

A classical analogue to understand the mechanisms that lead to optical activity in dimers has been demonstrated by Yin et al. The authors state that the natural OA in chiral media can be understood using the Born-Kuhn model, explaining the occurrence of OA based on two identical vertically displaced coupled oscillators. In analogy, they explain the origin of OA in dimers based on two identical corner-stacked gold nanorods (NRs). Depending on the handedness of the circularly polarized light used for illumination, dipoles are induced in the rods. If the two rods are considered at the stacking points (points for which the rods are closest to each other) the dipolar charge can either be identical or opposite, which is known as antibonding and bonding mode respectively, based on hybridization theory. This approach was tested by experiment using NRs with 223 nm length, 40 nm height and 40 nm width and a separation of 60 nm (and 120 nm) embedded in a dielectric. The spectral region was 1150–1500 nm with an absorption maximum at 1300 nm, giving a maximum ORD of up to 40°. Other studies used dark field scattering microscopy to analyze NR dimers with similar results, validating this analogy.[61,95]

3.1.3. Three-Nanoparticle System

Also known as "trimers", three-nanoparticle systems can exhibit strong chiroptical effects, as was shown, for instance, by Wang et al., in silver nanoparticle aggregates. The authors compared dimer and trimer configurations with a particle radius of 40 nm and an interparticle separation of 1 nm. For the trimer, the third NP is placed next to one of the other two, forming an L-shaped structure. For both of these systems the near-field response for LCP and RCP light was investigated numerically and, for the trimeric system, up to 1000 times larger enhancements for LCP than for RCP light was found. The tunability of the chiroptical response was shown by changing both the relative angle and particle separation of the third NP relative to the dimer configuration.[96]

Chuntonov and Haran also studied the optical response of plasmonic trimers. They found that for three NPs that are arranged in the same plane forming a tringle, the plasmon mode splitting can be tuned by gradually opening the angle between the middle NP and the two corner NPs, called the vertex angle. This leads to a symmetry breaking. The authors demonstrated dipolar plasmon eigenmodes based on hybridization theory; bonding and antibonding modes were identified at different energies, see Figure 4c.[97] Somewhat similar emergence of chirality due to the strength of electromagnetic coupling has been observed at microwave frequencies.[98]

Additionally, Toroghi et al. numerically studied multi-material trimers, made of gold nanoparticles surrounded by two silver nanoparticles, to measure the system as a function of NP size and interparticle spacing. The authors found that for specific sizes (80 nm Ag – 10 nm Au – 80 nm Ag) and separation (20 nm edge-to-edge) of such a system, the Au optical field enhancement is about 12 times larger than for isolated Au nanoparticles.[99]

3.1.4. Four-Nanoparticle System

A four-nanoparticle system is the minimum geometric requirement for perfectly spherical nanoparticles, of identical size and independently from a substrate, to be chiral. In practice though, producing such identical tetramers (consisting of four NPs) and positioning them precisely is quite difficult. Ogier et al. studied macroscopic layers of chiral plasmonic NP trimers and tetramers using colloidal lithography. They used closely spaced Ag and Au nanodiscs of different heights. Bisignate CD was identified and CD values of up to 2° were found. The authors describe the fabrication method for producing large areas of chiral trimer and tetramer nanostructures. Individual elements that compose the respective designs can be fabricated from different materials, which allows a high degree of control over the field enhancement. These strong field enhancements are localized in the gap between the discs.[100]

Another example of tetramers has been investigated by Hentschel et al., who studied 3D chiral plasmonic oligomers consisting of tetramers with two layers. The first layer comprises of three particles arranged in an L-shape, while the second layer contains a single disc, which is shown in Figure 4d. The position of this disc determines the handedness of the structure. The incident light (800–1600 nm) excites real currents flowing in the discs and is coupled with displacement currents between the elements. At the resonant frequency, the associated dipole moments and currents are increased, resulting in a strong plasmon-induced circular optical response, which is highly tuneable, depending on the geometry of the metallic discs.[101]

Starting with tetramers and increasing the number of nanoparticles, it is possible to create arrangements of helical geometry. This geometry is treated in Section 3.5.

There are numerous examples of studies involving higher number nanoparticles (>4). As an illustration, Layani et al. addressed the importance of the electromagnetic hotspots in the gap between silver nanoparticles within small aggregates.[102] The NPs have chiral surfactant molecules and aggregation was controlled by the pH, such that at larger pH values the nanoparticles separated. The authors observed a CD effect in the aggregated state only; upon separation of the nanoparticles the strong hotspots disappeared and the effect vanished. Further control of the nanoparticle hotspots can be achieved

by varying their shape. For instance in the case of silver nanocubes, hotspots occur at the vertices.[103] Shape is key for planar chiral systems.

3.2. Planar Chiral Systems

With modern nanofabrication techniques, it is possible to endow planar chiral nanostructures with virtually any conceivable symmetry. This results in a great variety of structure designs and possible orientations. Among the desirable properties of these materials are strong localized chiroptical enhancements (chiroptical hotspots) and large continuous regions of chiroptical enhancements.

At first glance, the term "planar chiral" could seem an oxymoron, since the word "planar" implies that the nanostructures are two-dimensional, whereas chirality is a three-dimensional property. And indeed, initially, there was some confusion with 2D chirality, which is the chirality of 2D objects placed in a 2D mathematical plane. These mathematical constructs would be truly chiral in a hypothetical 2D universe but are not truly chiral in our physical universe; the reason is that a 2D chiral shape in the x–y plane can be "picked up" and rotated, using the z-direction, to become superimposable on its mirror image. Nevertheless, because planar chiral nanostructures can be only a few nanometres thick, there was a question as to whether they might be considered two-dimensional with respect to their optical properties.

The question was first addressed by Kuwata-Gonokami et al. who investigated non-diffracting gratings consisting of chiral gold nanostructures, grown by electron beam lithography on a glass substrate, see **Figure 5**a. The dimensions are: pitch of the array = 500 nm, line width = 80 nm, Au thickness = 95 nm, followed by a Cr capping layer of 23 nm. Figure 5a shows three sample designs—two enantiomorphs and an achiral pattern. For each of these designs, the angle of optical rotation Δ is shown upon azimuthal rotation of the sample, measured by the angle φ. The observable offset (θ) depends on the chirality of the nanostructures and measures the chiroptical effect. Importantly, the chiroptical effects did not change sign upon flipping the sample, i.e., light incident from both the glass/Au interface and from the Cr/Au interface produced the same sign of chiroptical effect. This behavior is consistent with true 3D chirality. According to the authors, the three-dimensionality of the sample arises from the physical difference between the air-sample and sample-substrate interfaces. The measured CD was of the order of 4° per mm, in the 400–900 nm spectral range, and showed strong frequency dependence, characteristic of surface-plasmon enhancement.[104]

The OA in gammadion-shaped nanoparticle arrays was also studied theoretically by Bai et al.[105] The materials consisted of metal and dielectric, diffracting, nanoparticle arrays. The authors used the effective-medium approach in order to investigate the effect of the arrays on the polarization of the diffracted light. It was shown, that giant polarization rotations, up to tens of degrees, are achievable. According to the authors, their results were due to the circular birefringence (CB) of the nanostructures, which was enhanced by the plasmonic resonance. In dielectrics, the enhancement is due to a guided-mode resonance, whereas in metals the enhancement is due to surface-plasmon resonances. The authors confirmed that the polarization effects in their materials are reciprocal and that they vanish for symmetrically layered structures, in agreement with the paper from Kuwata-Gonokami.

Using again the gammadion shape, Arteaga et al.[106] considered more carefully the physical shape of the nanostructures and found that the fabrication procedure can play a very important role. In Figure 5b, the scanning electron micrograph on the left does not reveal any 3D features, however the angled and zoomed in view on the right shows that the nanostructures are more rounded on the top than at the bottom. This breaks the symmetry along the axis of the sample normal and renders the nanostructures 3D, regardless of the nature of the substrate. This study is important because it is well-known that deviations from optimal exposure during electron beam lithography can easily result in under- or over-etching. Even the slightest such deviations would be expected to produce 3D effects on the nanostructures.

Planar chiral nanostructures can yield chiroptical effects that are orders of magnitude larger than similar thickness molecular films. A good example is the work from Wu et al.,[107] who studied silver films with perforated S-shaped holes, showing a tuneable optical rotation of up to 90° depending on the thickness of the sample. The authors used experimental and numerical simulations to show that a superposition of electromagnetic waves from localized surface plasmons (LSPs) and surface plasmonic polaritons (SPPs) causes the large polarization rotation. The tunability is based on the fact that the metallic structures can be designed to supply specific electric field components through LSP resonances, while a phase retardation is controlled by the SPP wave, which allows for any desired optical rotation.

Planar chiral nanostructures can be positioned very precisely on the surface of the substrate, which allows them to benefit from lattice and Fano resonances in order to increase the chiroptical response. For instance, Zu et al.[108] prepared chiral planar heptamers made of gold, see Figure 5c. The authors systematically investigated the chiroptical response upon gradually changing the inter-particle rotation angles and separation distance in order to tune into the Fano resonance. They achieved a maximum response of 30% for the normalized CD in scattered light. Similar geometries have been investigated theoretically.[109]

Another chief advantage of planar chiral nanostructures is that their optical near-fields are accessible to scanning probe techniques, which provide high resolution in experimental mapping. Near-field circular dichroism imaging,[110] pioneered by the Okamoto group, is based on scanning near-field optical microscopy (SNOM) using LCP and RCP light. The resolution is below the diffraction limit, as can be seen in the recent work from Narushima et al.,[60] see Figure 5d. The authors imaged achiral gold C-shaped nanostructures, as a function of separation distance, until a chiral S-shaped nanostructure was formed. The 35 nm thick structures were fabricated by electron beam lithography on a glass substrate, using a 2 nm thick chromium adhesion layer. The outer and inner diameters of the C-shaped particles were 750 and 375 nm, respectively and the combined S-shaped particle extended to 1300 nm along its longest dimension. In Figure 5d, the near-field CD image on the left was

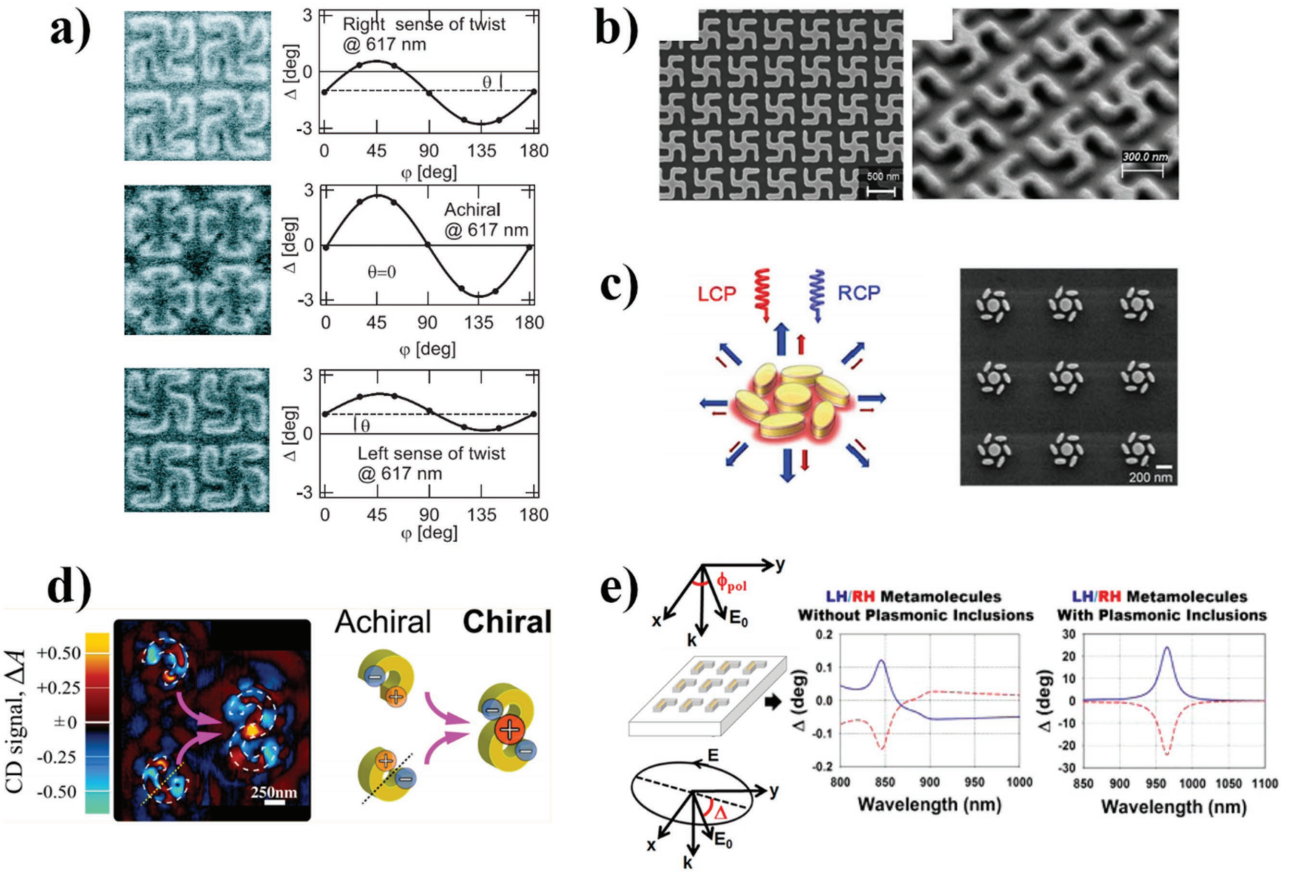

Figure 5. a) Planar chirality relies on the substrate achieve three-dimensionality. For each micrograph of the sample arrays, the optical rotation (Δ) as a function of sample rotation angle is shown. The observable offset (θ) measures the chiroptical effect. Reproduced with permission.[104] Copyright 2005, American Physical Society. b) Three-dimensionality of planar chiral nanostructures can originate from asymmetric fabrication. In the left panel, a zoomed-out view, from the direction of the normal shows no 3D features. In the right panel, a zoomed in, tilted view reveals that the top of the structures is more rounded than the bottom. Adapted with permission.[106] Copyright 2016, Optical Society of America. c) Strong control over position of neighboring structures gives access to lattice and/or Fano resonances to enhance the chiroptical signal. In these gold heptamers, the angle and separation distance have been tuned to the Fano resonance, in order to optimize the CD in scattered light. Adapted with permission.[108] Copyright 2016. The Royal Society of Chemistry. d) Planar chirality is convenient for experimentally mapping chiral hotspots with high resolution using surface probe techniques. Here, near-field circular dichroism imaging, at 785 nm, reveals chiral hotspots in achiral and chiral gold nanostructures. Adapted with permission.[60] Copyright 2014, American Chemical Society. e) Chiral metasurfaces could lead to ultra-thin optical components. Here, the optical rotation (Δ) of a dielectric, chiral metasurface is significantly enhanced upon embedding plasmonic gold nanorods within the long arm of the L-shaped nanostructures. Adapted with permission.[115] Copyright 2014, American Chemical Society.

obtained at the wavelength of 785 nm and the CD was evaluated through the measured quantity ΔA, which corresponds to the difference in absorbance of LCP and RCP, not normalized. Features that are smaller than 100 nm can be clearly distinguished. For the achiral particles, two opposite chiral hotspots can be distinguished at each end of the C-shape. Once combined into a chiral S-shape, the central hotspot becomes dominant, as illustrated in the right part of Figure 5d. In a subsequent paper by Okamoto's group, the authors attached additional C-shaped nanoparticles to the S-shaped ones and further confirmed that the dominant hotspots determine the far-field CD.[111] It should be pointed out that, Figure 5d constitutes a good illustration of several concepts that had been addressed previously by the Okamoto group. Indeed, it had already been established that opposite chiral hotspots can coexist within a single chiral enantiomorph.[112] Moreover, it had been reported that, for nanostructures with very small measured CD in the far-field, the near-field could exhibit chiral hotspots, where the CD effect is, locally, orders of magnitude larger than in the far-field.[113] In the extreme case, it had also been shown that for achiral nanostructures, where the far-field CD is zero, there are strong chiral hotspots in the near-field, whose effects cancel in the far-field.[114] Another example of the interplay between near- and far-fields is metasurfaces.

Metasurfaces are very thin, artificially structured materials, whose dimensions are smaller than the wavelength of light. For the optical and near-infrared regimes, they are usually made from planar nanostructures. Metasurfaces can affect the polarization, phase, or direction of light and can serve as ultra-thin optical components. Chiral metasurfaces make use of the chiroptical effects. Because metals exhibit high loss, metasurfaces tend to be constructed from dielectrics. However, combining dielectrics and metals can sometimes provide a significant improvement to the desired functionality. Such

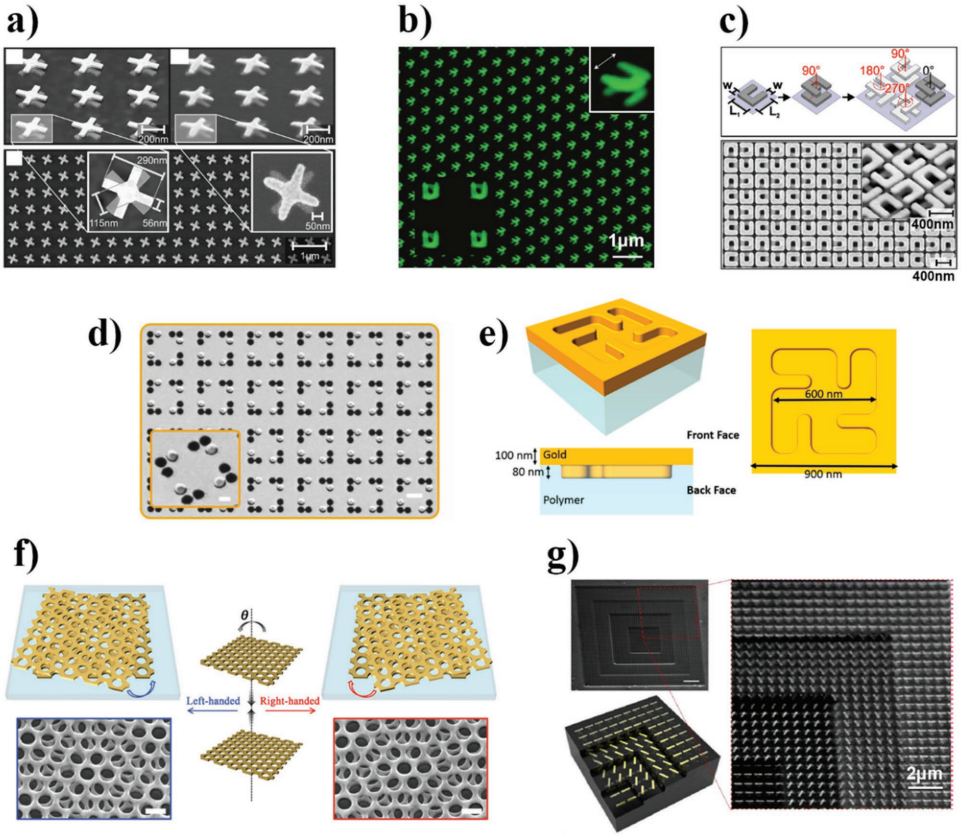

Figure 6. a) A pioneering double-layer chiral system that consists of two gold crosses, twisted at an angle with respect to each other. Adapted with permission.[116] Optical Society of America. b) Double-layer of U-shaped gold nanostructures whose electric and magnetic dipole resonance determine the chiroptical effects. Adapted with permission.[117] Copyright 2009, Nature Publishing Group. c) Schematic diagram and SEM image of a four-fold rotationally symmetric double-layer, composed of U-shaped gold nanostructures. Adapted with permission.[59] Copyright 2010, Optical Society of America. d) A double-layer of gold discs and disc-shaped voids in a gold film uses Babinet's principle to achieve chiroptical effects. Adapted with permission.[120] Copyright 2013, American Chemical Society. e) A gammadion-shaped gold nanostructure with a similarly shaped void directly above it form the unit cell of this double-layer chiral system. Babinet's principle is employed here to enhance optical chirality. Adapted under the terms of the Creative Commons Attribution 4.0 License.[121] f) An ingenious double-layer chiral system based on Moiré patterns. The angle between the two golden thin-films with circular voids determines the handedness. Reproduced with permission.[124] Copyright 2017, John Wiley and Sons. g) SEM view of a four-layer stack of gold nanorods prepared by conventional lithography techniques. The gold nanorods in each subsequent layer are rotated at 60° with respect to the layer underneath. Reproduced with permission.[125] Copyright 2012, Nature Publishing Group.

improvements are demonstrated by Alali et al.,[115] and are shown in Figure 5e. The authors investigated numerically a chiral metasurface of dielectric L-shaped nanostructures with gold nanorod inclusions. The dielectric had a refractive index on 1.6, consistent with conventional negative photoresist SU8. The L-shaped nanostructures were 200 nm thick, with a wire width of 300 nm. The long arm of the L measured 350 nm in length and the short arm 180 nm. The nanorods were 200 nm long and 80 nm wide. As the spectra in Figure 5e demonstrate, the plasmonic inclusions yielded much larger polarization rotation (Δ) than the corresponding purely dielectric chiral metasurface.

3.3. Multilayered Chiral Systems

For all their advantages, planar chiral nanostructures (see Section 3.2) exhibit limited chiroptical effects in the far-field. This limitation is in part due to the small thickness of material involved in the light-matter interaction. Another, more important, reason is that whereas chirality is a three-dimensional property, the three-dimensionality of planar nanostructures is intrinsically limited. It is very straightforward to conceive that by stacking multiple layers of chiral nanostructures, the thickness can be increased, and the chirality of the material would become more pronounced. In practice though, these multi-layered chiral systems often require advanced nanofabrication techniques.

Figure 6a shows an early example of a chiral double-layer, with sub-wavelength dimensions for the optical part of the spectrum. Decker et al,[116] prepared these gold crosses, where the lines are 56 nm wide, 315 nm long and 25 nm thick. Within each layer, the crosses are disposed in a square lattice, whose constant is 500 nm. An individual cross is not chiral, however when it is placed on top of another cross and tilted at an angle different from 0° (and multiples of 90°), chirality develops along the direction normal to the sample surface. This superposition was achieved by two-step electron-beam lithography, where the alignment of the materials for both steps was key.

This chiral double-layer achieved an optical rotation of 4° at the wavelength of 1.36 μm.

Similarly, U-shaped nanostructures are not chiral on their own, yet, when placed on top of each other, at an angle different from 0° (and multiples of 180°), they become chiral, see Figure 6b. Liu et al.[117] prepared these U-shaped nanostructures using gold, with thickness 50 nm, length and width 250 nm, wire width 90 nm and vertical separation 50 nm. The fabrication involved electron-beam lithography and ion-beam etching. The U-shaped geometry is also referred to as split-ring resonators (SRRs). This is because light can cause electric currents in the metal loop, which acts as an inductor (L). Furthermore, the electric currents are stopped at the ends of the loop, where charge accumulates, as in a capacitor (C). This miniature electric LC circuit can resonate at a particular frequency of light. When two such resonators are in close proximity, as in Figure 6b, their electric and magnetic dipoles can experience plasmonic coupling, which leads to hybridization. Depending on the twist angle between the SRR layers, the orientation of these electric and magnetic dipoles tunes the chiroptical effects. This very powerful idea has been used in subsequent works and has been elaborated upon.

SRRs can also be oriented in a chiral pattern within a single layer. Decker et al.[59] prepared an array of SRRs, where the unit cell is made of 4 SRRs, each rotated at 90° with respect to its neighbors. Consequently, the unit cells are chiral and propeller-shaped. Moreover, a second layer of SRRs is placed on top of the first one, in such a way that each top SRR is rotated at 90° with respect to the SRR underneath it. The result can be seen in Figure 6c. The fabrication procedure was similar to that in reference,[116] using two-step electron-beam lithography. The SRRs were made of gold, with length 380 nm, width 350 nm, wire width 115 nm and thickness 60 nm. The spacer layer was 85 nm thick and the lattice constant in each layer was 885 nm. It should be pointed out that the purpose of the propeller-shaped unit cells was neither to increase the chiroptical effect by using this additional chirality, nor to benefit from side-by-side coupling of the SRRs. Instead, the aim was to achieve four-fold rotational symmetry, as it was recognised that the arrangement in Figure 6b leads to strong linear birefringence that complicates the chiroptical response. Optical rotation of 30° was achieved at the wavelength of 3 μm. Similar geometries where used to construct devices for longer wavelengths.[118,119]

Besides SRRs, another efficient way to affect the interplay between electric and magnetic dipoles is by using Babinet's principle. Whereas the electromagnetic properties of solid nanostructures (such as gold discs on a substrate) are conveniently described in terms of electric dipoles, for inverted structures (such as disc-shaped holes in a continuous gold thin-film) the description is more convenient in terms of magnetic dipoles. A superposition of discs on top of a layer with disc-shaped holes would therefore present a convenient playground for the interactions between electric and magnetic dipoles. Hentschel et al.[120] introduce such solid-inverse structures made of gold, see Figure 6d. A two-step electron beam exposure was used and the inverse layer was fabricated by argon milling. Each structure (hole or disc) had a 200 nm diameter, a thickness of 40 nm and the interparticle spacing was 20 nm. The vertical separation was 30 nm. Just as in the previous paragraph, the structure has a C_4 symmetry to suppress linear birefringence. A small but measurable bisignate CD response was observed in the region from 1 to 1.7 μm.

A much more explicit interplay between electric and magnetic dipoles through Babinet's principle was achieved by Jack et al.,[121] see Figure 6e. Contrary to the fabrication methods discussed before, the process here is much more cost-effective and yields a large-scale material; it is based on a technique for Blu-Ray manufacturing.[122] The material is produced by indenting a polymer substrate with the shape of the nanostructures. The dimensions of the structures are shown in Figure 6c and the gammadions are disposed in a square array with periodicity 900 nm. Subsequently, 100 nm thick Au layer is deposited on top of the indented substrate, covering the film and filling in the indented regions. The result is a hybrid solid-inversed double-layer, with solid nanostructure and an identically shaped void directly above it. It follows that the symmetry equivalent electric and magnetic modes of the solid and inverse structures are in the immediate neighborhood of each other and can couple, yielding strong chiroptical effects. One way to look at the interaction is to consider that such coupling can lead to increased optical chirality (i.e., achieve superchiral light, see Section 4.3), where collinear electric and magnetic fields are necessary. For longer wavelengths, Hannam et al. added another degree of freedom to this kind of solid-inverted double-layers, by rotating the solid structure with respect to the underlying inverted one.[123] As the metamaterial studied had C4 symmetry, the authors were able to extract effective parameters including the chirality parameter (see Section 4.1).

Another example where a double-layer achieves superchiral light is shown in Figure 6f. Wu and Zheng[124] made an ingenious use of Moiré patterns upon combining two identical achiral gold nanohole arrays. This fabrication process also produces large-scale nanostructuring and is cost-effective. Using nanosphere lithography, individual achiral free-floating films were prepared and were subsequently placed on top of each other, at an angle to one another, through a wet-transfer method. The handedness of the double-layer depends on the value of the angle. When single layers are illuminated, numerical simulations reveal electromagnetic hotspots at the edge of the holes. Due to the relative displacement between the holes in each individual layer, some of the holes in the double-layer are strongly reduced in size, which causes a dramatic enhancement of the hotspots and leads to locally enhanced optical chirality. The principle of coupling one layer to the next in order to achieve chirality can be extended well beyond double-layers.

Zhao et al.[125] constructed a four-layer stack of gold nanorods, where each layer was rotated at 60° with respect to the one underneath it, see Figure 6g. The authors made use of conventional lithographic techniques to prepare the nanorods that were 250 nm long, 60 nm wide 5 nm thick. A CD was measured in the spectral region 600 nm to 1200 nm.

We have seen that a variety of multi-layered chiral systems are emerging, with a focus on manipulating the interplay between electric and magnetic dipoles in the nanostructures. These systems face important challenges for their fabrication. Electron beam lithography is a prime tool in this context, with several examples reported in the literature[126,127] requiring two[59,116]

and more[57] steps. Fine alignment is required between the steps and the addition of layers can cause issues with the focus of the electron beam.[118] Electron beam alignment is crucial for obtaining nanostructures with straight vertical sides, which are necessary to avoid creating accidental chirality due to the fabrication process (see Section 3.2). However, less sophisticated fabrication processes are also emerging and are making successful use of techniques, such as templated substrates and conventional lithography. Other fabrication methods are focusing at directly producing extended 3D networks.

3.4. Three-Dimensional Chiral Networks

Three-dimensional chiral designs offer the opportunity to create large, periodic, self-standing chiral systems without requiring a substrate. A prominent aspect of these networks is the large volume of light-matter interactions, compared to planar chiral or multi-layered systems. An important factor to consider though is that the extra dimension adds complexity; for instance, within the same material competing chiral arrangements can form. Although the present fascinating shapes, 3D chiral networks are challenging to fabricate and understand. Different fabrication methods for plasmonic and dielectric chiral networks have been reviewed by Hossain and Gu.[128]

A self-assembled chiral optical metamaterial with 3D-structure, was presented by Vignolini et al., see **Figure 7**a. The authors used electrodeposition of gold and self-assembly to create a gyroid with features on the 10-nm length scale. The experimentally tested sample was 200 nm thick and formed domains with sizes varying between 10–100 μm. The anisotropy was demonstrated by illuminating the gyroids with linearly polarized light, resulting in clear color changes across different domains, due to the birefringence of the sample. In order to investigate the chiroptical behavior, the gyroids were tilted by 35° and rotated around the [110] surface normal. By illuminating with LCP and RCP light the spectral regions with the least spectral variations were indicated and averaged. Plotting the resulting gyrotropic transmission over the sample rotation yields two maxima for the sample rotation angles of 0° and 180°, indicating optical activity.[129]

A different approach was taken by Radke et al., who used direct laser writing and electroless silver plating to produce the bichiral crystals shown in Figure 7b. The resulting structure is reported to be highly isotropic, which has been proven by demonstrating only a weak dependence on the angle of incident light for the measured transmission spectrum. A large difference in the transmittance of LCP and RCP light was shown in the mid-infrared (3–5 μm) with a difference in the transmission of LCP/RCP with a relative bandwidth $\Delta\lambda/\lambda = 29\%$.[130]

A similar method was used by Kenanakis et al. creating a three-dimensional network based on two perpendicular split-cube resonators. The authors demonstrate strong asymmetric transmission in the infrared spectrum with up to 90° optical rotation. Further, it was shown that the design was also scalable to provide asymmetric transmission in the optical region.[131]

Unfortunately, electron beam lithography and laser writing are rather expensive fabrication methods to produce chiral

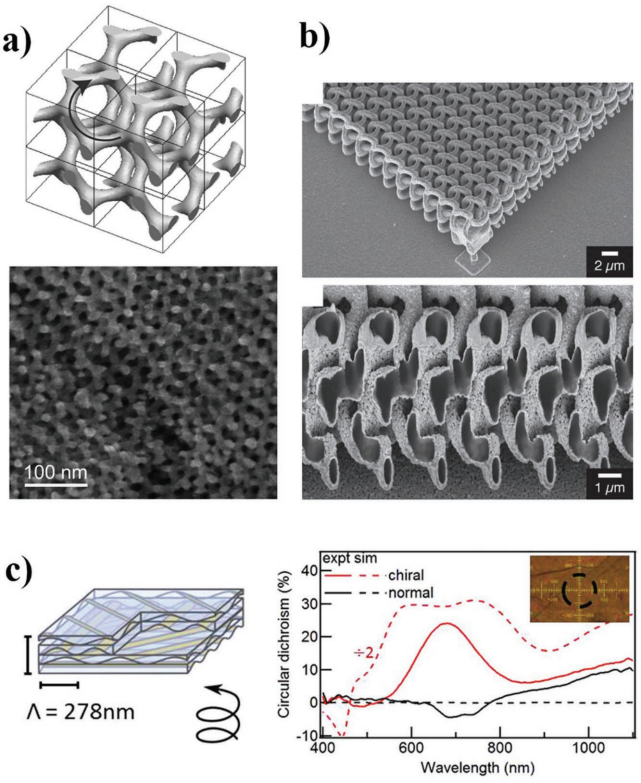

Figure 7. a) Schematic showing a chiral self-assembled gold gyroids optical metamaterial. The spirals in the light path depend on the angle of incidence (top). SEM image of the gyroids (bottom). Adapted with permission.[129] Copyright 2011, John Wiley and Sons. b) (Top) SEM image (top view) of bichiral crystals fabricated by using direct laser writing and silver plating. (Bottom) cross-section of the network. Adapted with permission.[130] Copyright 2011, John Wiley and Sons. c) (Left) Schematic of chiral gold nanowire woodpile stacking. (Right) Resulting spectrum of CD vs. wavelength for the chiral (red) and achiral (black) arrangement of gold nanowires. The dashed line represents the simulated results, while the solid line denotes the experimental result. The inset displays a reflection image and the dashed circle outlines the 50 μm collection spot. Adapted under the Creative Commons Attribution License.[132]

designs. Ibbotson et al. suggested a different approach based on multiple stacking of gold nanowires to form woodpile photonic crystals. The authors imprinted gratings into a sacrificial polymer layer. At a glancing angle, gold was deposited onto the polymer layer forming nanowires with a width of 50 nm, thickness of 30 nm and multiple cm in length. After transferring the nanowire-grating onto a different polymer, the authors were able to stack multiple layers on top of each other. Every second layer was rotated by either 45° (see Figure 7c (left)) or 90° to form plasmonic gratings. The result is a large scale single-domain 3D optically active medium, yielding a CD of about 25% for the chiral arrangement (45° rotation of every second layer), which can be seen in the spectrum shown in Figure 7c (right).[132]

Three-dimensional chiral networks are still at a very early stage of their development as plasmonic materials. By contrast, the research into helical materials, which are also pronouncedly three-dimensional, is much more advanced.

3.5. Helical Materials

The helix is the archetypal chiral geometry and, not surprisingly, it attracts considerable attention. Helices can be made, for instance, from continuous metal wire, from continuous helical grooves on a metal cylinder or from individual particles that are disposed in a helical arrangement. The helical geometry offers considerable freedom of design, as it is possible to vary the material, the wire diameter, the loop diameter, the pitch, the number of pitches or the lattice parameters, as well as to intertwine multiple helices and to change the handedness of the helix within the same structure. These variations in design allow fine tuning of both geometrical and optical chirality (see Section 4).

The electromagnetic properties of metallic helices have attracted interest at various length scales and wavelengths of radiation. In the later 1940s, Kraus invented the helical antenna,[133] which is widely used today (for instance, in Wi-Fi networks). He considered that the helix is a fundamental shape, of which the straight line and the loop are extreme cases. Correspondingly, he described two separate radiation modes: the normal radiation mode, where the maximum radiation is normal to the helix, and which occurs for helices much smaller than the wavelength, and the beam radiation mode, where the maximum radiation is in the direction of the helix axis, and which occurs for helices whose diameter is comparable to the wavelength. This importance of the size of the helices compared to the wavelength of radiation is significant throughout the electromagnetic spectrum. Another feature of the helical antenna, highlighted by Kraus, is that it is very broadband. This is again true throughout the electromagnetic spectrum; for instance, whereas most chiral plasmonic nanostructures exhibit enhanced chiroptical effects near resonances, nanohelices have much larger operation bandwidth.

Tinoco and Freemann[135] studied oriented arrays of macroscopic copper helices with microwaves, as a function of the wavelength. Their hope was that this model system could provide insight into the interaction between light and chiral molecules. They addressed birefringence, scattering effects and diffraction, all of which could contribute apparent optical rotation that is not directly related to chirality. The data were discussed in terms of the Drude equation, which fitted well the measurement results. In the same year, the linear optical response of metallic helices was described by Kauzmann within a classical model as a one-electron system, bound to a helix.[136] A few years later, Tinoco and Woody used a somewhat similar model:[137] one electron free to move on a helix. The model starts with the coordinates of a particle on a helical path and proceeds to calculate the kinetic energy in order to obtain the Hamiltonian for a particle in a one-dimensional box, with the arc length along the helix as the coordinate. This model predicts that the optical rotation will be positive, for the longest wavelengths, in right-handed molecules or helices. Although the model could be applied to both conjugated molecules and metal helices, it assumes that the helices are much smaller than the wavelength of light. It is only in 1980 that the model was extended to include helices that are large compared to the wavelength,[138] i.e., a case that is comparable to the original experimental work with microwaves.

It is worth noting that the above-mentioned one-electron on a helix models can be seen as special cases of the one-electron model proposed by Condon et al.[139] The latter constitutes a seminal work because, whereas previous models saw optical activity as emerging from the dynamic coupling between several electronic oscillators, in the one-electron model, optical activity results from a single electron moving in an asymmetric field. Such fields can be observed, for instance, around asymmetric carbon atoms, where the field causes a helical torsion on the electron cloud, leading to a chiroptical response.

Plasmonic nanohelices typically exhibit chiroptical effects in the IR and visible part of the spectrum and they are said to enter the metamaterial regime when their dimensions are significantly smaller than the wavelength of light. Despite the small size involved, it became possible to visualize the regions of local electromagnetic enhancements within metal helices, with the help of numerical simulation tools. A good example is the work by Zhang and Zhao, where such enhancements are investigated as function of the geometry of the helices and as a function of polarization of the incident light.[140] Interestingly, these tools seem to bring about a return to the coupled electron oscillator models. For instance, Zhang and Zhao proposed a periodic effective dipole model to explain the chiroptical behavior of Ag nanohelices, where the dipoles are situated along the wire.[141] Similarly, Li et al. proposed a plasmon hybridization model, where the electric dipoles are situated along the wire and extend along half a pitch of the helix.[142] Nevertheless, attempts have also been made to evaluate analytically the chirality parameters in helical structures.[143]

In the nonlinear regime, a classical model for the second harmonic generation response has been proposed by including an anharmonic term to the classic oscillator.[144] A similar SHG model later highlighted the importance of magnetic terms in the SHG chiroptical response.[137] Furthermore, the one-electron on a helix system has also been treated quantum mechanically.[145] Until recently though, helical structures have been very challenging to produce at the nanoscale.

Nowadays, there are several examples of chiral plasmonic and nano/meta-materials. Famously, gold helices have been proposed as broadband circular polarizers. The helices were made by direct laser writing, they measured several microns and chiroptical effects were demonstrated in the range 3.5 to 6.5 microns.[146] Further optimization was discussed in terms of loop radius, wire radius, pitch, number of pitches and lattice constant. Helical antenna behavior was also described in terms of emission of CPL and in terms of CPL conversion.[23]

As we mentioned in Section 2.4, Fan and Govorov studied theoretically a helical assembly of nanoparticles with the aim to optimize the CD response of the system.[79] The influence of helical pitch, major radius of the helix and minor radius (size of the nanostructures) was discussed. It was also found that the chiroptical response is very stable against defects in the arrangements, such as missing nanoparticles in the helical arrangement[147] Extinction ratio is also improved upon switching from a cylindrical helix to a conical one.[148] Furthermore, the extinction ratio and the bandwidth could be enhanced simultaneously by tapering the helix radius along the helix axis.[149] Experimentally, such helical assemblies were realized using dielectric scaffolds, such as twisted fibers[78] and peptides.[150] A different

methods, using glancing angle deposition, was adapted by the Ghosh group.[151–153]

Several authors have investigated the effects of increasing complexity of the helices. For example, implementing a double helix geometry was predicted to broaden the bandwidth of circular polarizers by 50%.[154] Song et al. used peptide-directed assembly to construct a double helix superstructure of electromagnetically coupled (mainly dipole-dipole) gold nanoparticles. The observed CD was of the order of 40 mdeg. in the visible spectrum. As expected, the chiroptical response was found to be tuneable depending on the structural parameters of the double helix.[155] Triple interlocked helices were fabricated by Esposito et al. using focused ion beam-induced deposition. The composition of the helices was expected to be 40% platinum and 60% carbon. The device demonstrated up to 37% CD in the spectral range 500 nm to 1 µm. An optical rotation of 8° was also reported.[134] Later, the same group reported triple nanohelices with higher platinum content and compared their chiroptical properties to those of purely dielectric phenanthrene ($C_{14}H_{10}$) triple helices. The effect of wire length on single helices was also investigated.[156] Kaschke et al. examined a design of four intertwined helices within the context of a circular polarizer and reported that CPL conversion in both reflection and transmission is completely eliminated. However, in such quadruple helices, metal losses are required to preserve the behavior of the CPL polarizer effect, which limits the frequencies of application.[157]

Plasmonic helical nanostructures can also naturally give rise to large regions of high optical chirality, in which chiroptical interactions are enhanced due to parallel electric and magnetic field components (see Section 4.2). These regions are situated in the space inside the helix (**Figure 8**a), and it has been shown that better confinement of the fields inside the helix can be obtained by interlocking multiple helices.[158] Nair et al.[142] calculated a very strong optical chirality in helices made of SiO_2 and decorated with Au (8 m) and Ag (15 nm) nanoparticles. The authors studied the effects of coupling between the nanostructures and in particular the transition from purely dipolar interactions to a regime where multipolar contributions play an important role. This transition was observed at $r/a = 2.3$, where r is the center-to-center distance between nanoparticles and a is the nanoparticle radius. It was found that the strength of the chiroptical interaction increases almost exponentially as the nanoparticles where brought closer together, which also caused a shift and a broadening of the CD spectrum. Two-photon-induced photo-luminescence CD was also reported from this kind of systems.[159]

Helical nanostructures typically result in CD spectra in the visible and NIR regions, where the plasmon resonances are situated. For instance, Esposito et al. made use of focussed ion and electron beam induced deposition to prepare platinum helices with up to 22% CD in the visible spectrum. These techniques allow very fine control over the dimensions of the structures and highly ordered arrays of helices, within small arrays (Figure 8b).[160] In the same year, the same group reported near 40% of CD in the NIR region.[161] He et al. obtained continuous helices by helically stacking plasmonic layers. This was achieved with glancing angle deposition (GLAD), starting with polystyrene spheres (diameters 200, 350 and 500 nm). Then Ag and SiO_2 vapours were deposited as alternating layers (nominal thickness of 30 nm) at different rotation angles to the polystyrene spheres, resulting in an overall helical structure. The process allows tuning independently the helix pitch and diameter, and was demonstrated to tune the CD in the visible and NIR regions.[162] The Zhao group made use of various shadowing deposition growth methods to fabricate helical composite Ti/Ag thin films,[163] metal composite (Ti/Ag) and metal/dielectric composite materials (Ag/MgF_2) nanoscale helices,[164] and titanium-doped silver chiral nanorod arrays.[165] Although the individual structures were not very well resolved,

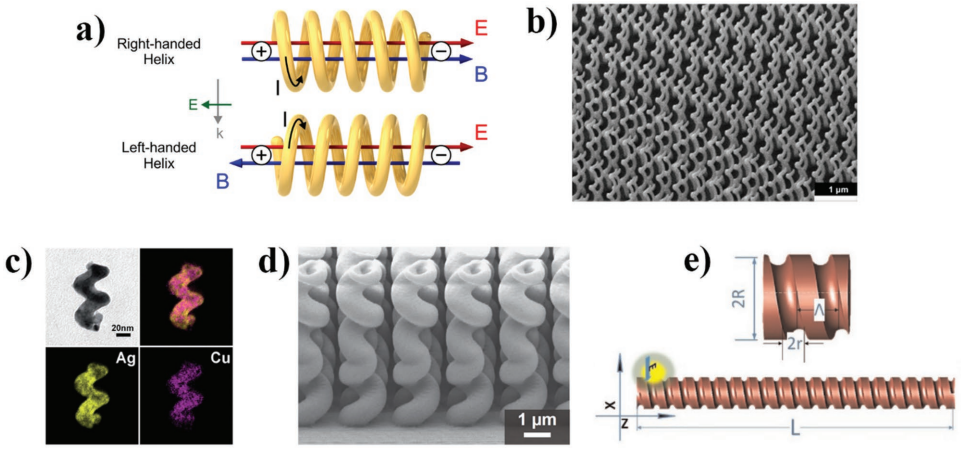

Figure 8. a) Schematic diagrams of left- and right-handed helices. An electric field (E), parallel to the axis of the helices causes charge splitting. The induced current give rise to magnetic fields, whose direction depends on the handedness of the helix. Reproduced with permission.[158] Copyright 2014, American Chemical Society. b) Platinum helices produced by focused ion and electron beam deposition. Reproduced with permission.[160] Copyright 2015, American Chemical Society. c) Energy-filtered TEM (EF TEM) chemical mapping of a metal, Ag–Cu 50:50 alloy, nanohelix. The false color representations of the Ag and Cu are shown as a mixture (top-right) and independently (bottom-left and bottom–right, respectively). The scale bar measures 20 nm. Reproduced from[167] with permission of The Royal Society of Chemistry. d) Heterochiral helices, with reversing handedness half-way along the structure. Reproduced with permission.[171] Copyright 2015, John Wiley and Sons. e) Helically grooved metal wire waveguides, conceived for studies at the THz frequency. Reproduced with permission.[174] Copyright 2015, Elsevier.

the large-scale continuity of the films allowed for characterization with ellipsometry, which is very useful in order to separate the various anisotropic contributions from the actual chiral response. Combining good fabrication resolution of individual helices and large area production, the continuous metal nanohelices manufactured in Fischer's group are currently among the most interesting chiroptical materials (Figure 8c).[43,166,167] Crucial for the success of this method is that the shadow growth proceeds from seed elements that are disposed in a regular lattice. As a consequence, the helices can be well separated from their neighbors. This method yields both chiral thin films[21,43,167,168] and metal nanohelical suspensions in liquids.[21,43,45,169] The nanohelices can be produced from various materials, including noble metals,[45,65,167,168] magnetic materials,[21,169] and, most recently, magnesium[170] which has promising UV properties.

A "heterochiral" helical structure was proposed by Wegener's group. This structure consists of a helix that changes handedness halfway along the helix axis. At first look, such a design appears to be achiral overall, assuming cancelation from the opposite handedness in the upper and lower parts of the helix (Figure 8d). In practice though, CPL interacts selectively with either the upper or the lower part. The physical connection between the two parts breaks the symmetry, because it allows more current to flow in the "forbidden" part depending on relative position. This dissymmetry allows the structure to function as a broadband polarization converter.[171] Deng et al. also investigated heterochiral helices. They started by using GLAD to construct Ag nanohelices with a pitch of 200 nm. These nanohelices exhibit a bisignate CD response, with one clear peak in the UV (around 375 nm) and anther in the visible part of the spectrum.[73] The CD effect in the UV was attributed to absorption and that in the visible part of the spectrum was attributed to scattering. Heterochiral helices were then produced and it was shown that the CD was very different, depending on the number of turns in the helices and depending on the length of the wire (varied in the range below one full pitch).[172]

Yao and Zhong investigated numerically an original helical geometry—they studied helically grooved metal wire waveguides and characterized their response at THz frequencies. It was reported that a linear Gaussian beam of light, incident on the structure, gives rise to a surface plasmon wave whose chirality is determined by the helicity of the groove. It was reported that a circularly polarized electromagnetic wave can emerge from this structure (Figure 8e).[173,174] Another interesting aspect of helices is that they constitute a mechanical spring. This was explored by Slobozhanyuk et al. at GHz frequencies (1 GHz is $\lambda \approx 30$ cm) showing an interesting interplay between elastic and electromagnetic properties.[175]

Helical arrangement is also observed for molecules in liquid crystals and it is possible to benefit from this order in constructing chiral plasmonic nanomaterials. Wang et al. constructed a system consisting of Au nanorods dispersed within liquid crystals. Due to the photothermal effect, heating of the nanorods, with IR light, at plasmon resonance, was shown to reverse the chirality of the liquid crystal assembly. Upon cooling the liquid crystal switched to its initial chiral state. This study demonstrated a strong CD effect in the visible that is due the switching of the liquid crystal's chirality.[176]

Another example of a helical structure is the DNA molecule that is treated in the next section.

3.6. DNA Materials

The DNA molecule is one of the best known helical structures and it has been associated with chiral plasmonic materials in a variety of manners. For instance, DNA strands can serve as building blocks for assembling chiral architectures at the nanoscale, such as pyramids, nanohelices, nanorod dimers, trimers, twisted strings, etc. In each of these cases, DNA allows very precise positioning of the nanoparticles, which improves control and tuneability of the chiroptical properties. DNA has also been used as a template for plasmonic nanoparticles, upon which a chiral shell of a different plasmonic material can be grown. This building mechanism allows the chiroptical response to be tuned between the plasmon resonances of the two materials. Furthermore, plasmonic nanoparticles have been used to strongly enhance the chiroptical properties of DNA, significantly lowering the limits of DNA detection. Additionally, the plasmon enhanced chiroptical response of DNA can be instrumental for monitoring the actuation of nanorobots. All of these examples are treated in this section.

In an early work, a double-stranded DNA scaffold was used as template on which Ag nanoparticles (≈10 nm) were grown. A large CD was reported at the wavelength of the Ag nanoparticle resonance.[177] In the same year, DNA origami was proposed as a method for assembling arbitrary geometrical shapes at the nanoscale. The methods consist of weaving a thread of single strand DNA into the desired pattern. The pattern is then held in place by selecting appropriate complementary strands (the staples). The method allows control of assembly at the sub 40 nm scale, which is hard to access with top-down techniques. No chiral designs were included in the initial publication on the subject.[178]

Sharma et al. proposed to assemble four rectangular tiles, made of DNA, into a sheet that was subsequently rolled into a tube. Some of the DNA tiles carried Au nanoparticles (5 nm). Depending on the way the tube was rolled, it was possible to achieve helical arrangements of the nanoparticles in single, double or nested helical geometries. The authors did not present a strict characterization of the chiroptical response of their structures.[179]

Chiral nanostructures were also assembled by building a DNA pyramid with Au nanoparticles of different size at each tip. The nanoparticles were 5 nm, 10 nm, 15 nm, and 20 nm in size. The pyramid was assembled with single strand DNA running through all sides of a triangle, tracing a single face of the pyramid. By this method, it is possible to choose the chirality of the structure simply by switching the position of Au nanoparticles of different size, depending on the linker molecules on the surface of the NPs. No remarkable chiroptical behavior was reported, likely due to lack of plasmonic coupling, since the nanoparticles were far apart (**Figure 9**a).[180]

Much more rigid tetramers were assembled by Shen et al. using a DNA origami sheet, with dimensions 90 nm × 60 nm × 2 nm. The Au nanoparticles were all of the same size (20 nm) and their position was precisely determined on the DNA sheets,

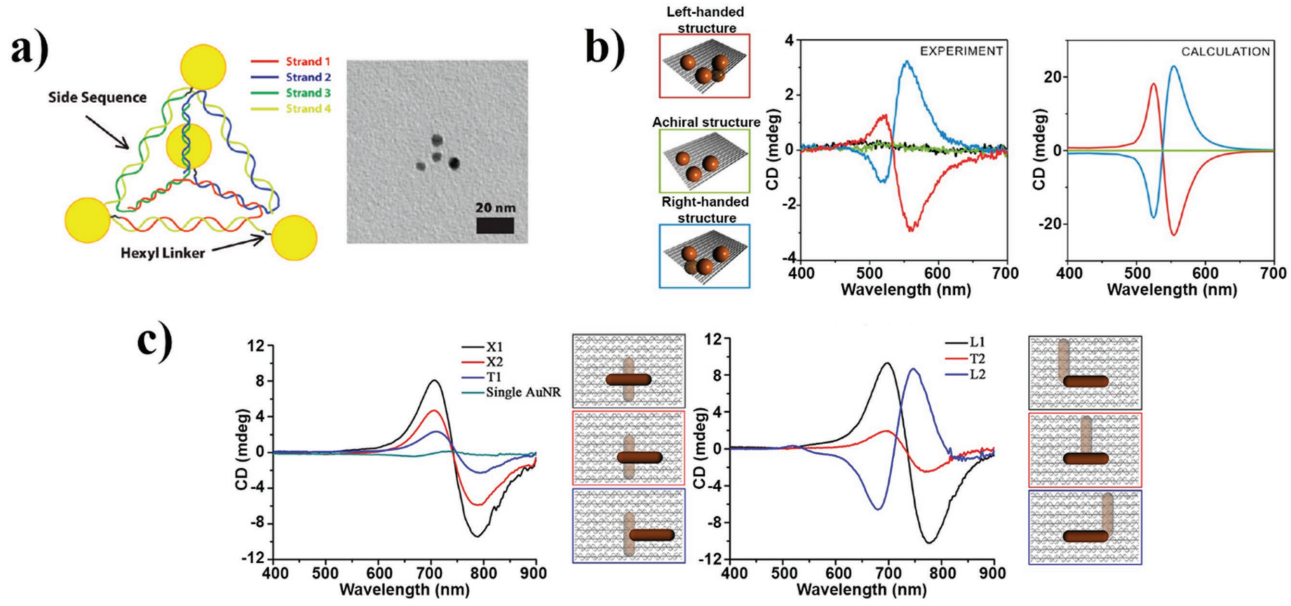

Figure 9. a) (Left) schematic diagram and (right) TEM of a DNA nanocrystal pyramid. Reproduced with permission.[180] Copyright 2009, American Chemical Society. b) A DNA origami template is used to precisely assemble a pyramid from four gold nanoparticles (diameter 20 nm). The experimental and calculated CD spectra show a clear CD that depends on the handedness of the structures. Reproduced with permission.[181] Copyright 2013, American Chemical Society. c) Two gold nanorods are positioned precisely with respect to each other using a DNA origami template. The CD spectra for orientations X1, X2 and T1 demonstrate chiroptical response originating from the DNA molecules and being transferred to the surface plasmon of the nanorods via dipole-plasmon Coulomb interaction. The CD spectra for orientation L1, T2 and L2 demonstrate chiroptical response originating from the nanorods dimer, i.e., plasmon-plasmon interaction due to the chiral geometry. Reproduced with permission.[188] Copyright 2013, American Chemical Society.

using helper and binder single strand DNA. Three nanoparticles were positioned on the same side of the sheet and the forth was situated on the opposite side. A strong CD was demonstrated in the spectra for both enantiomorphs, with a peak or a dip positioned at the wavelength of plasmon resonance, depending on the enantiomorph (Figure 9b).[181] In another work by the same authors, similar rectangular DNA origami sheets were used. On the surface of each sheet, the authors designed 15 binding cites that ran in two parallel lines diagonally to the sheet. Then they functionalized Au nanoparticles (10 nm and 13 nm in diameter) with complementary DNA, which allowed the nanoparticles to bind precisely at their designated locations on the DNA origami sheet. Finally, they stapled the edges of the DNA sheets to form tubes. The result was a well-organized helix of Au nanoparticles that exhibited maximum CD at a wavelength corresponding to the plasmonic resonance of the nanoparticles.[182] Significantly smaller DNA origami tubes have recently been produced by Cecconello et al.[183]

In 2012, Kuzyk et al. reported on a DNA origami scaffold designed to hold Au nanoparticles (10 nm) into a tight helical structure, where direct plasmon coupling was enabled. The nanostructures exhibited a bisignate CD with the positive peak corresponding to the plasmon resonance. The negative dip was attributed to the isotropic arrangement of the helices, whereby the longitudinal and transverse plasmon modes are both excited. Longitudinal and transverse modes were reported as typically exhibiting opposite chirality.[184] In a subsequent work, the selective excitation of either the longitudinal or transvers modes of the nanohelices was enabled resulting in switchable CD. The procedure involved emptying and filling up a quartz cuvette, where the nanohelices were attached to the walls, in order to achieve switching. Clearly, this was not the most practical switching mechanism but the group reported that the dimensions of the nanohelices were remarkably small: helical pitch 57 nm, diameter 34 nm, and overall length 79 nm.[185] A more practical method of switching was proposed by Kuzyk et al. based on an X-shaped gold nanorod dimer. Each nanorod (38 nm × 10 nm) was placed on a DNA origami bundle (80 nm × 16 nm × 8 nm). The relative angle between the bundles and hence the chirality of the dimer could be switched with DNA locks, which resulted in switchable CD.[186]

Plasmonic resonances can also be used to detect the chirality of DNA. Upon functionalizing gold nanorods (aspect ratio of 3) with single strand DNA, it was demonstrated that DNA assembling into double strands aggregated the nanorods. This resulted in strong near-field hotspots, which in turn lead to strong CD at the plasmonic resonance wavelengths. The process was reversible, depending on temperature and a detection limit of 75 nM was reported for DNA.[187]

An interesting interplay between the chirality of DNA and that of the nanostructures was demonstrated by Lan et al. Au nanorods (11 nm × 37 nm) were assembled into dimers using bifacial DNA origami. The DNA sheets had a rectangular shape with dimensions 90 nm × 60 nm × 2 nm. A nanorod was precisely positioned on each side of the DNA sheet, in a way that allowed the position of one nanorod to be tuned with respect to the other. Tuning the relative positions of the nanorods within the dimers lead to clear differences in the CD spectral response. Interestingly, the authors demonstrated bisignate CD spectra, which were predominantly due to the chirality of DNA

(in X-shaped nanodimers) and to the chirality of the NR geometry (in L-shaped nanostructures) (Figure 9c).[188] Using slightly different Au nanorods (12 nm × 40 nm), on a similarly sized DNA sheet (90 nm × 60 nm × 2 nm), Shen et al.[189] suggested a physical origin for the sign change in the bisignate CD between L-shaped enantiomorphs. Drawing a parallel with Kuhn's classical oscillator mode, they invoked a physical mechanism based on symmetric and antisymmetric hybrid modes, which was found to be in good agreement with the experimental results. Furthermore, they demonstrated a CD response due to a single gold NR on the DNA origami sheet and showed that the CD reverses depending on whether the NR was parallel or perpendicular to the DNA molecules.

Plasmonic nanostructures can thus be employed to detect the chirality of DNA. Ma et al. investigated the chiroptical response from Au nanorods (62 nm length, 22 nm diameter), side-by-side assembled with DNA. It was shown that the DNA caused a twist between adjacent nanorods, which produced a strong bisignate CD in the plasmonic part of the spectrum. The reported limit of DNA detection in this manner was 3.7 aM. This scheme worked only for short chains of nanorods and upon increasing the number of nanorods above 20, the CD disappeared.[190]

Wu et al. covered Au NPs (20 nm and 15 nm) with DNA and then grew a silver shell on the Au NPs by adding silver ions (Ag^+) that attached to the DNA. This DNA templating of the Ag shell resulted in a thickness of up to 8 nm for the shell and a strong CD was observed at ~400 nm, i.e., close to the plasmon frequency of Ag.[191]

Urban et al.[20] demonstrated an example of nanorobotics, where two plasmonic walkers (Au NRs of 35 nm × 10 nm) positioned on a DNA origami sheet (58 nm × 42 nm × 7 nm). On the opposite side of the DNA, a third Au NR (the stator) was positioned perpendicularly to the previous two. The trimer was thus initially H-shaped and achiral (only a small CD was observed, likely due to the DNA molecules of the origami sheet). However, once one walker took a step towards the other, the trimer becomes chiral and this gave rise to a significant CD (40 mdeg.). Depending on which walker took the first step, the sign of the CD changed. Here the chiroptical response of the walkers was instrumental for measuring their performance.

3.7. Extrinsic Chirality

It is possible to obtain a chiroptical response in plasmonic nanostructures that exhibit neither 3D nor 2D chirality. Instead, chirality is introduced by the geometry of the experiment itself; the wave-vector, the surface normal and the direction of curvature on the sample form a chiral triad. Plum et al. measured a chiroptical response from achiral split-ring structures in the microwave and optical regimes (**Figure 10**a top and bottom respectively).[192] These structures were shown to exhibit both circular dichroism and circular birefringence when illuminated at oblique incidence. At normal incidence, no significant optical activity was measured for either structure. The circular birefringence resulted in rotation of linear polarization exceeding 60° for microwaves. For the visible part of the spectrum, rotation of 1° was measured, which is larger than that of many intrinsically chiral structures. Later observations, directly comparing extrinsic and intrinsic chirality, confirmed that the former can yield significantly stronger response.[193]

More generally, it was shown that extrinsic optical activity effects can be observed from any lossy, periodically structured surface that is illuminated at an oblique angle.[194] The fundamental mechanism for this optical activity is shown in Figure 10b. When illuminated at normal incidence, the structure geometry remains unchanged when projected onto the transverse plane of the incident light, see Figure 10b left. However, when the sample is illuminated at an oblique angle the projection of the structure geometry onto the transverse plane of incident light becomes distorted. Under inversion, the structure's projection can no longer be superimposed onto itself, and is therefore chiral, as shown in Figure 10b right. Plum et al. showed that asymmetric transmission (circular difference) can occur in any array of nanostructures whose projection onto the transverse plane of incident light is 2-dimensionally chiral and anisotropic. It is therefore possible to achieve chiroptical effects utilizing simpler structures than those that are intrinsically chiral; the latter being limited by the fabrication complexity.

Cao et al. demonstrated, experimentally and numerically, strong circular dichroism in the mid-IR region (~2.4 μm), resulting from extrinsic chirality in achiral nanostructures.[195] The structures consisted of a rectangular array of thin gold squares, separated by a dielectric layer (GaAs) atop a continuous gold film (Figure 10c). They demonstrated that both enantiomers of the structure can be obtained by tilting the sample at opposite angles. This fact, it is suggested, can be utilized to simplify experiments requiring both enantiomers of a nanostructure, by removing the need to fabricate two separate structures.

In order to better understand the mechanism behind the previously observed extrinsic chiroptical response, Hu et al. performed a numerical analysis of "nanorice heterodimers" (Figure 10d). It was found that pairs of parallel "nanorices" made of different materials exhibit circular dichroism when illuminated at oblique angles.[196] The authors show that the structures exhibit Fano resonances due to coupling between the nanorices, the spectral positions of which can be varied by changing the structure's dimensions and materials. Around the Fano resonances, strong CD is observed. Changing geometric properties of the heterodimers causes both the Fano spectral profile and the CD spectrum to change correspondingly. Structures showing large Fano asymmetry also exhibit the strongest CD signal. It is therefore proposed that the Fano resonance causes an enhancement in the CD.

Further work by Hu et al. aimed to analytically describe extrinsic chirality in plasmonic nanostructures.[197] An achiral split-ring structure was numerically analyzed to demonstrate that, at oblique angles, such an achiral structure will exhibit large CD at NIR wavelengths. By analyzing the simulated surface charge distributions, it was shown that, at oblique angles, the circular current within the split-ring caused the ring to behave like a magnetic dipole around resonant modes. These magnetic modes interact with the electric plasmonic modes resulting in a mixed magneto-electric polarizability and hence non-zero chirality. This mixing of magnetic and electric dipoles is then responsible for the large CD. Recently, Belardini et al.

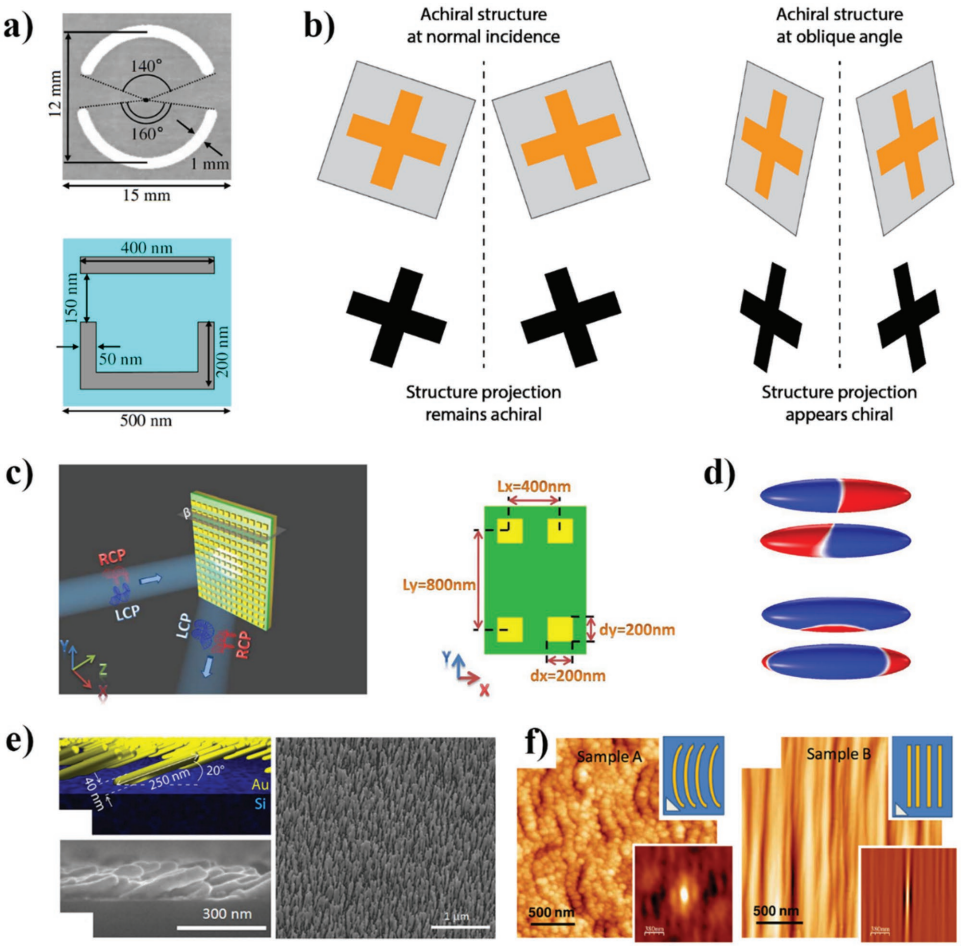

Figure 10. a) Achiral split ring resonator structures used to demonstrate extrinsic chirality at microwave (top) and optical (bottom) frequencies. Reproduced with permission.[192] Copyright 2009, American Physical Society. b) Schematic representation of extrinsic chirality in an achiral structure. c) Rectangular array of achiral gold nanostructures separated from a gold film by a dielectric layer. Adapted with permission.[195] Copyright 2014, Macmillan Publshers. d) In these two "nanorice" dimers the nanorods are parallel and lack intrinsic geometric chirality. Chirality is introduced by a combination of the arrangement of materials within the dimers (schematically Au, blue; Ag, red) and through extrinsic chirality due to an oblique angle of incidence of light. Adapted under the Creative Commons Attribution License from[196] e) 3D model (top left) and SEM images of a surface of tilted gold nanowires. The tilt of the wires causes extrinsic chirality, depending on the illumination direction. Adapted under the Creative Commons Attribution License from[198] f) AFM morphology images of curved (left) and straight (right) nanowire surfaces. The curved wires were shown to exhibit strong extrinsic chirality, whereas the straight wire surface gave no significant chiral response. Reproduced with permission.[200] Copyright 2011, American Physical Society.

have demonstrated strong chiroptical effects at optical wavelengths from a surface of tilted nanowires (Figure 10e).[198] The extrinsic chirality was measured using a combination of optical reflectance and photoacoustic absorbance. While optical reflectance measurements served to demonstrate the linear dichroism resulting from the anisotropic structure geometry, circular dichroism measurements relied upon a photoacoustic technique. In this technique, the heat produced and transferred to the structure surroundings is measured in order to directly probe the material absorption of incident light; scattered light does not affect the signal as only absorbed energy is measured. Upon rotating the sample by 180°, the measured extrinsic chirality reverses. The selective absorbance of circularly polarized light can therefore be controlled by varying the structure orientation relative to the incident beam. The CD measurements were found to correspond well to optical rotation measurements, with the same reversal being demonstrated.

The same work also reported that extrinsic chirality affects nonlinear optical measurements. By continuously varying the orientation of a quarter wave plate acting on 800 nm linearly polarized light, the second harmonic generation CD (SHG-CD), at 400 nm, was measured for various sample orientations. The SHG-CD was also measured as a function of the angle of incidence of light, for opposite orientations of the nanowires. As expected, the opposite orientations resulted in a reversal of the SHG-CD, and an optimal value for the angle of incidence was found at around 50°. Additional work showed the same dependency of the SHG-CD on the angle of incidence of pump light, demonstrating that extrinsic chirality is induced by the relative angle between the light and the surface normal.[199] A theoretical analysis of the effective nonlinear susceptibility tensor describing the system showed that different tensor components become non-zero depending on the wire orientation, but reversing the wire orientation by rotating through 180° caused

the tensor components responsible for the chiroptical response to reverse sign. Importantly, the authors found that the CD measured in the nonlinear case was around 50 times larger than the linear measurements. Previous work by Belardini et al. had demonstrated similar results in an array of curved nanowires (Figure 10f).[200] In an array of similarly fabricated nanowires without a curve, inversion symmetry holds even at oblique angles of incidence. However, when curved, extrinsic chirality results in a measurable CD signal. Linear optical measurements were taken and again found to be significantly weaker than their nonlinear counterparts.

For applications requiring manipulation of light polarization, such as optical rotation or circular dichroism, it may be possible to use extrinsic instead of intrinsic chirality. The relative simplicity of fabrication for achiral nanostructures could open the field to more readily available and easier to mass-produce geometries. The key here would be to consider the experimental geometry as a whole.

3.8. Magnetochiral Materials

In the previous sections, it has been discussed how chirality breaks inversion symmetry and leads to optical activity. However, it is possible to rotate the polarization of light without chirality. Applying a magnetic field to a transparent dielectric, such as glass, causes the plane of polarization of transmitted light to be rotated. This phenomenon is known as the Faraday effect. In general, magneto-optical and chiro-optical effects are distinct and separate. However, it is possible to couple magnetism and chirality in the linear optical regime. This is achieved by breaking both time-reversal and inversion symmetry simultaneously with the application of a magnetic field onto a chiral medium which leads to a higher order optical response, termed magnetochirality.[201]

The magnetochiral term can be seen in the dielectric tensor of a homogeneous chiral medium under an applied magnetic field, **B**, by expanding out to first order in wave vector **k** and **B**,[202]

$$\varepsilon_{\pm}^{L,R}(\omega,\mathbf{k},\mathbf{B})=\varepsilon_0(\omega)\pm\alpha_{NCD}^{L,R}(\omega)k\pm\beta_{MCD}(\omega)B+\gamma_{MChD}^{L,R}(\omega)\mathbf{k}\times\mathbf{B}. \quad (14)$$

Here, the superscripts L and R indicate the handedness of the medium, ± indicates the eigenmodes for RCP and LCP light. In general, the material parameters ε_0, α, β, and γ are complex. The term $\alpha_{NCD}^{L,R}(\omega)k$ is the contribution from natural circular dichroism (NCD) with no applied magnetic field. The term $\beta_{MCD}(\omega)B$ is the contribution from magnetic circular dichroism (MCD). The cross term $\gamma_{MChD}^{L,R}(\omega)\mathbf{k}\times\mathbf{B}$ describes the magnetochiral response, which has three key features. Firstly, it depends on the relative orientation between the wave vector **k** and magnetic field **B**. Secondly, it depends on the handedness of the material. Thirdly, it is independent of the polarization of incident light meaning magnetochiral effects occur for unpolarized light. This gives rise to magnetochiral birefringence in refraction.[203] In absorption, it manifests as a magnetochiral dichroism (MChD), where unpolarized light is preferentially transmitted in one direction. The differential absorption due to each of these effects is quantified by the following equations:[204,205]

$$CD=2\frac{A_{RCP}-A_{LCP}}{A_{RCP}+A_{LCP}}, \quad (15)$$

$$NCD=CD(\mathbf{B}=0), \quad (16)$$

$$MCD=CD(\mathbf{B})-NCD, \quad (17)$$

$$MChD=A(\mathbf{k}\uparrow\uparrow\mathbf{B})-A(\mathbf{k}\uparrow\downarrow\mathbf{B}), \quad (18)$$

where A in the final equation for MChD is the absorbance of unpolarized light, $A=(A_{RCP}+A_{LCP})/2$. The terms $A(\mathbf{k}\uparrow\uparrow\mathbf{B})$ and $A(\mathbf{k}\uparrow\downarrow\mathbf{B})$ denote the absorbance when **k** and **B** are parallel or anti-parallel, respectively. It is also useful to compute anisotropy factors for all these effects such that they are normalized to the total absorbance:[206]

$$g_{NCD}=\frac{NCD}{A(\mathbf{B}=0)}, \quad (19)$$

$$g_{MCD}=\frac{\partial}{\partial B}\frac{MCD}{A(\mathbf{B}=0)}, \quad (20)$$

$$g_{MChD}=\frac{\partial}{\partial B}\frac{MChD}{A(\mathbf{B}=0)}. \quad (21)$$

Detection schemes for magnetochiral effects have been demonstrated utilizing an alternating magnetic field and phase sensitive detection methods to measure changes in absorbance as a function of varying applied magnetic field. By also measuring the total absorbance of unpolarized light, in the absence of an applied magnetic field, the anisotropy factor, g_{MChD}, can be calculated. An experimental configuration for the detection of magnetochiral effects is shown in **Figure 11**a (left). An alternating magnetic field is directed either parallel or antiparallel to the direction of propagation of the light. Transmitted light is then phase sensitively detected with respect to the frequency of the alternating magnetic field. Designs for a magnetochiral spectrometer have also recently been put forward in order to promote the investigation of MChD.[207] There are two major contributions to magnetochiral effects probed by these detection schemes. The first is from the imaginary part of the material parameter γ and is termed the pure magnetochiral contribution. The second contribution stems from an interplay between the imaginary parts of the parameters α and β and is known as the cascaded contribution.[203]

The promise of engineering meta/nanostructures with magnetochiral responses has already been anticipated.[208] MChD has been observed in natural materials such as multiferroic chiral-lattice magnets.[209] It has also been demonstrated that chiral meta-molecules can exhibit MChD in the microwave region of the spectrum.[210] The first experimental demonstration of MChD in the visible spectrum with substantially subwavelength ($\lambda < 10$) metallic nanostructures was

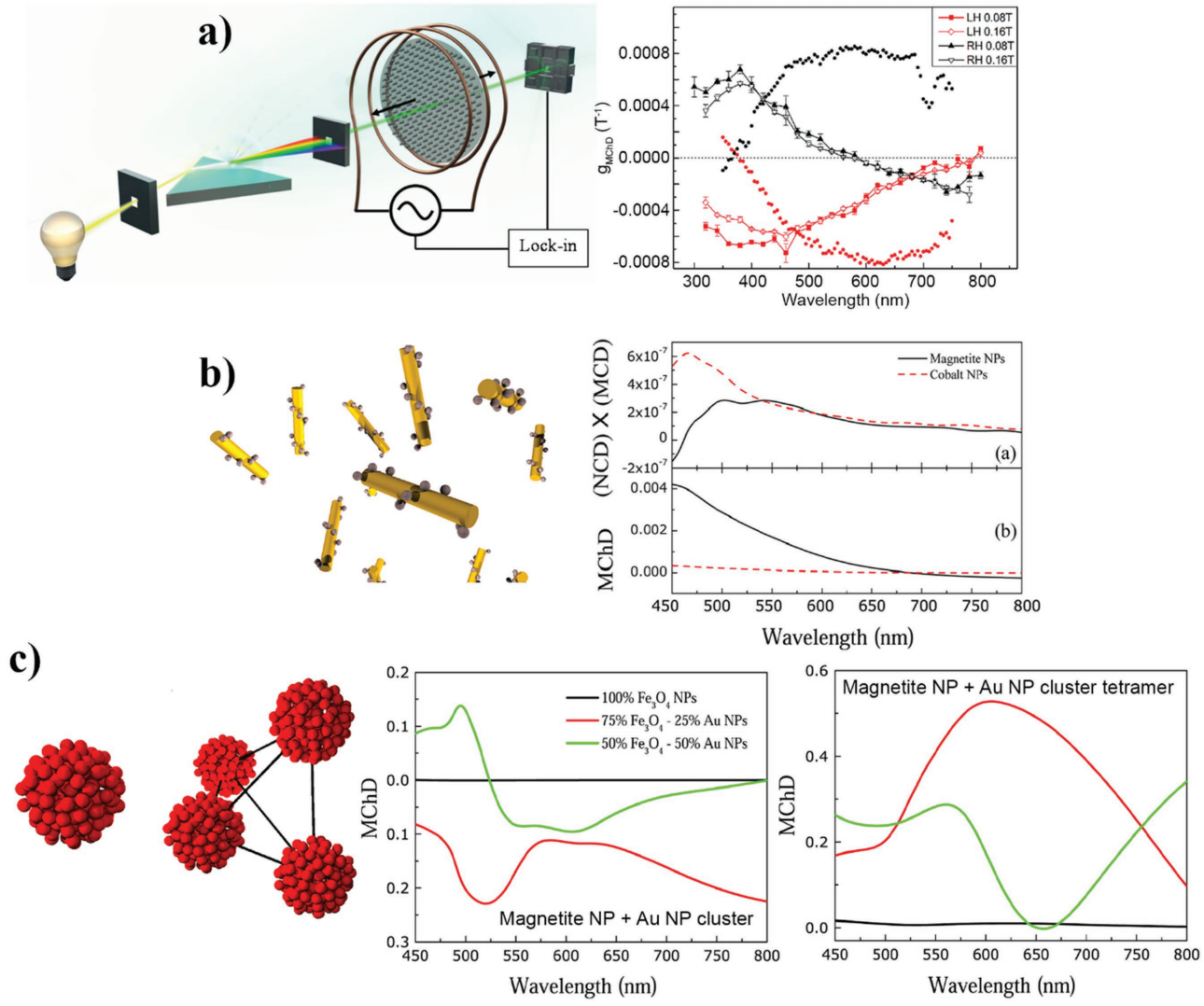

Figure 11. a) Left, diagram of an experimental configuration for measuring magnetochiral dichroism. Right, the magnetochiral dichroism anisotropy factor, g_{MChD}, for the left-handed (red) and right-handed (black) nanohelix suspensions. Scattered solid circles correspond to the approximation of g_{MChD} using NCD×MCD at 0.16 T. Reproduced with permission.[206] Copyright 2014, American Chemical Society. b) Left, schematic diagram of a dilute suspension of magnetoplasmonic nanohelices formed of magnetic nanoparticles coiled around gold nanorods. Right, comparison of NCD×MCD with MChD for magnetite (black) and cobalt (red) nanohelices. Reproduced with permission.[204] Copyright 2015, American Chemical Society. c) Left, A cluster of magnetite nanoparticles alongside a tetramer of clusters. Middle, MChD for magnetite NP clusters with a proportion of NPs substituted with Au NPs. Right, same as middle with a tetramer of clusters. Reproduced with permission.[205] Copyright 2015, Elsevier.

provided by Eslami et al.[206] Experiments were conducted on a film consisting of an array of nickel nanohelices ~100 nm in length. The geometric constraint of Ni nanomagnets helps to suppress the formation of multiple domains and leads to local surface plasmon resonances. Measurements of the NCD, MCD and g_{MChD} were performed on both enantiomorphs, that is arrays of left- and right-handed nanohelices. To first order, the anisotropy factors for NCD, MCD, and MChD are related by $g_{MChD} \approx 1/2 g_{NCD} g_{MCD}$ and can be used to predict the strength of a magnetochiral response where cascaded contributions are expected to dominate.[202] The calculated estimate and experimentally determined values of g_{MChD} for the Ni nanohelices are shown in Figure 11a (right). The estimated and experimental values do not match, suggesting the main contribution to the MChD is due to pure rather than cascaded effects.

Suspensions of randomly orientated helices made from magnetic nanoparticles coiled around a gold rod, as shown in Figure 11b (left), have been investigated theoretically.[204] Freestanding helices of magnetic nanoparticles (magnetite and cobalt) were considered first. The effect of inserting a gold nanorod into the center of the freestanding helix is then studied. The surface plasmon resonance supported by the gold nanorod increases all differential absorptions, NCD, MCD, and especially MChD. Unexpectedly, the MChD of the magnetite-gold helix is higher than the cobalt-gold helix. This cannot be explained by a cascaded effect associated with the product of NCD and MCD. The inability of a cascaded effect to explain

the discrepancy is demonstrated in Figure 11b (right), where NCD×MCD is contrasted against the MChD for magnetite and cobalt nanohelices. The calculated estimate of MChD for cobalt is stronger or at least on par with magnetite, however this is not reflected in the measured MChD. In addition to pure magnetochiral contributions to the MChD, a toroidal moment induced change in the dielectric function is proposed to also contribute to the non-reciprocal propagation of light. The toroidal moment in the nanohelix system is defined as $\mathbf{T} = \mathbf{p}_{rod} \times \mathbf{m}_{hel}$ where $\mathbf{p}_{rod}$ is the electric dipole moment of the gold rod and $\mathbf{m}_{hel}$ is the magnetic dipole moment of the helix formed by the NPs. This toroidal moment induces a change in the dielectric function of the form $\Delta\varepsilon = \eta^{L,R}_{toroid}(\omega)\mathbf{k}\cdot\mathbf{T}$ which, similarly to the magnetochiral term, depends on the direction of propagation of light. In turn, this contributes to the non-reciprocal propagation of light through the nanohelix suspension. The authors also point out that suspensions similar to the ones studied have already been fabricated using bottom up approaches such as supramolecular self-assembly, peptide- and DNA-assisted self-asse mbly.[53,179,182,184,211,212]

Clusters of magnetite nanoparticles (NPs) interspersed with gold nanoparticles, shown in Figure 11c (left), have also been studied theoretically.[205] Initially, single clusters of magnetite NPs are modelled, their MChD response is given by the black line in Figure 11c (middle). The single clusters demonstrate an increased MChD compared to single magnetite NPs due to interparticle interactions. Substituting a portion of the magnetite NPs for gold NPs in the cluster further increases the MChD and the other types of differential absorption, NCD, and MCD. This is explained by the local field enhancements provided by the Au-NPs. The MChD responses of clusters with different proportions of Au-NPs are shown in Figure 11c (middle) and suggest that the proportion of Au-NP substitution provides a degree of tuneability to the MChD. Larger scale structural chirality is introduced into the system by arranging four magnetite-gold NP clusters into a tetramer. This has the effect of, again, increasing all types of differential absorption, NCD, MCD, and MChD. The MChD of tetramer structures with different proportions of Au-NPs is shown in Figure 11c (right). It is also mentioned by the author that clusters resembling the ones studied have been fabricated by bottom up self-assembly.[213]

4. Chirality Parameters

4.1. Structural Chirality Parameters

In the simple case of a linear, isotropic medium with no magnetoelectric coupling, the macroscopic electromagnetic response of the material is described by the constitutive relations given in Equation (22). These relate the material's internal electric displacement field $\tilde{\mathbf{D}}$ and magnetic field strength $\tilde{\mathbf{D}}$ to the driving electric and magnetic fields $\tilde{\mathbf{E}}$ and $\tilde{\mathbf{B}}$. Here, ε and μ are complex (denoted by a tilde) scalars and correspond to the isotropic electric permittivity and magnetic permeability of the material.

$$\begin{aligned}\tilde{\mathbf{D}} &= \tilde{\varepsilon}\tilde{\mathbf{E}}\\ \tilde{\mathbf{B}} &= \tilde{\mu}\tilde{\mathbf{H}}\end{aligned} \tag{22}$$

In the general case however, we cannot assume isotropy and a lack of magnetoelectric coupling. For a bi-anisotropic medium, the constitutive relations take the form of Equation (23).[214,215] Here, $\tilde{\varepsilon}$, $\tilde{\mu}$, $\tilde{\xi}$ and $\tilde{\zeta}$ are 3×3 matrices due to the anisotropy of the material, and the second-order tensors $\tilde{\xi}$ and $\tilde{\zeta}$ describe the magnetoelectric cross-coupling.

$$\begin{bmatrix}\tilde{\mathbf{D}}\\ \tilde{\mathbf{B}}\end{bmatrix} = \begin{bmatrix}\tilde{\varepsilon} & \tilde{\xi}\\ \tilde{\zeta} & \tilde{\mu}\end{bmatrix}\begin{bmatrix}\tilde{\mathbf{E}}\\ \tilde{\mathbf{H}}\end{bmatrix} \tag{23}$$

In the case of a non-gyrotropic material (one in which inversion symmetry holds due to an absence of any gyrotropic currents), Equation (23) has the additional constraints given in Equation (24).[215]

$$\begin{aligned}\left[\tilde{\xi}\right]^t &= -\left[\tilde{\zeta}\right]\\ \left[\tilde{\varepsilon}\right]^t &= \left[\tilde{\varepsilon}\right]\\ \left[\tilde{\mu}\right]^t &= \left[\tilde{\mu}\right]\end{aligned} \tag{24}$$

The expressions shown in Equation (22) are a special case of Equation (23), where no magnetoelectric cross-coupling is present, so $\tilde{\xi} = \tilde{\zeta} = 0$ and due to isotropy, the dyads $\tilde{\varepsilon}$ and $\tilde{\mu}$ become scalars. In the case of an achiral anisotropic material, $\tilde{\xi} = \tilde{\zeta} = 0$ however $\tilde{\varepsilon}$ and $\tilde{\mu}$ remain as matrices. Most relevant in this discussion however is the special case of an isotropic chiral (bi-isotropic) medium. In this case, the matrix components relating $\tilde{\mathbf{D}}$ and $\tilde{\mathbf{B}}$ to $\tilde{\mathbf{E}}$ and $\tilde{\mathbf{H}}$ reduce to complex scalars, but all four components remain. The constraints given in Equation (24) apply, and thus $\tilde{\xi} = -\tilde{\zeta}$. There are several ways to write the remaining relations for a reciprocal bi-isotropic medium, including Post's relations,[214] the Drude-Born-Fedorov (DBF) relations,[216,217] and Tellegen's relations[214,218,219] as given in Equation (25).

Tellegen's relations

$$\begin{bmatrix}\tilde{\mathbf{D}}\\ \tilde{\mathbf{B}}\end{bmatrix} = \begin{bmatrix}\varepsilon_0\tilde{\varepsilon}_r & i\tilde{\kappa}\sqrt{\mu_0\varepsilon_0}\\ -i\tilde{\kappa}\sqrt{\mu_0\varepsilon_0} & \mu_0\mu_r\end{bmatrix}\begin{bmatrix}\tilde{\mathbf{E}}\\ \tilde{\mathbf{H}}\end{bmatrix}$$

Post's relations

$$\begin{bmatrix}\tilde{\mathbf{D}}\\ \tilde{\mathbf{H}}\end{bmatrix} = \begin{bmatrix}\tilde{\varepsilon}_p & i\tilde{\xi}_c\\ i\tilde{\xi}_c & \tilde{\mu}_p^{-1}\end{bmatrix}\begin{bmatrix}\tilde{\mathbf{E}}\\ \tilde{\mathbf{H}}\end{bmatrix}$$

DBF relations

$$\begin{aligned}\tilde{\mathbf{D}} &= \tilde{\varepsilon}_{DBF}(\tilde{\mathbf{E}} + i\tilde{\chi}\tilde{\mathbf{B}})\\ \tilde{\mathbf{B}} &= \tilde{\mu}_{DBF}(\tilde{\mathbf{H}} - i\tilde{\chi}\tilde{\mathbf{D}})\end{aligned} \tag{25}$$

Tellegen's relations appear most widely used when discussing chiral metamaterials, and so this form will be adopted here, however the various forms are still equivalent. Here, $\tilde{\varepsilon}_r$ and $\tilde{\mu}_r$ are the relative permittivity and permeability of the material, respectively, and $\tilde{\kappa}$ is known as the chirality parameter. This chirality parameter is key when considering effects such as negative refractive index. Solving Maxwell's equations for a monochromatic plane wave propagating in the z-direction

through the chiral medium results in two eigenwaves with wavenumbers given by Equation (26),[220,221] where k_0 is the wavenumber in vacuum. In a chiral medium, these eigenwaves of wavenumber k_+ and k_- correspond to right and left circularly polarized waves respectively.

$$\tilde{k}_{\pm} = \tilde{k}_0 \left(\sqrt{\tilde{\mu}_r \tilde{\varepsilon}_r} \pm \tilde{\kappa} \right) \tag{26}$$

From this, the refractive indices for LCP and RCP light are given by Equation (27).[50,214,221]

$$\tilde{n}_{\pm} = \sqrt{\tilde{\mu}_r \tilde{\varepsilon}_r} \pm \tilde{\kappa} \tag{27}$$

Like the refractive index $\tilde{n}$, the chirality parameter $\tilde{\kappa}$ is a complex quantity. In the case of refractive index, the real part corresponds to the phase velocity of propagating light, and the imaginary part describes the attenuation of propagating light (the extinction coefficient). It follows from Equation (27) that the real part $\mathrm{Re}(\tilde{\kappa})$ describes the difference in phase velocity between LCP and RCP light, and the imaginary part $\mathrm{Im}(\tilde{\kappa})$ describes the difference in attenuation of LCP and RCP light. The complex nature of $\tilde{\kappa}$ thus leads to two directly measurable effects: a non-zero real part results in optical rotation (circular birefringence), and a non-zero imaginary part results in circular dichroism.

Additionally, Equation (27) shows that within an isotropic chiral medium, if the chirality parameter $\tilde{\kappa}$ is large enough (specifically when $|\tilde{\kappa}| > \sqrt{\tilde{\mu}_r \tilde{\varepsilon}_r}$), the refractive index for either LCP or RCP light can become negative. However, both cannot be simultaneously negative in this case.

We now consider the induced electric and magnetic dipoles $\tilde{\mathbf{p}}$ and $\tilde{\mathbf{m}}$ within an anisotropic chiral (bi-anisotropic) metamaterial. In the general case of a bi-anisotropic material, the induced dipole moments on each metamaterial unit cell or inclusion are given by

$$\begin{bmatrix} \tilde{\mathbf{p}} \\ \tilde{\mathbf{m}} \end{bmatrix} = \begin{bmatrix} \tilde{\alpha}_{ee} & \tilde{\alpha}_{em} \\ \tilde{\alpha}_{me} & \tilde{\alpha}_{mm} \end{bmatrix} \begin{bmatrix} \tilde{\mathbf{E}} \\ \tilde{\mathbf{B}} \end{bmatrix} \tag{28}$$

Here, $\tilde{\alpha}_{ee}$ and $\tilde{\alpha}_{mm}$ are the electric polarizability and magnetic susceptibility respectively, and $\tilde{\alpha}_{em}$, $\tilde{\alpha}_{me}$ relate to the mixed magnetoelectric polarizability. In the case of an isotropic chiral medium the matrix components become scalars, and this reduces to Equation (29). The mixed magnetoelectric polarizability $\tilde{\alpha}_{em}$ is highly dependent on the chirality parameter; if $\tilde{\kappa} = 0$ then the material is achiral and $\tilde{\alpha}_{em} = 0$, when $\tilde{\kappa}$ changes sign $\tilde{\alpha}_{em}$ also changes sign.[220]

$$\begin{bmatrix} \tilde{\mathbf{p}} \\ \tilde{\mathbf{m}} \end{bmatrix} = \begin{bmatrix} \tilde{\alpha}_{ee} & i\tilde{\alpha}_{em} \\ -i\tilde{\alpha}_{em} & \tilde{\alpha}_{mm} \end{bmatrix} \begin{bmatrix} \tilde{\mathbf{E}} \\ \tilde{\mathbf{B}} \end{bmatrix} \tag{29}$$

Due to the complexity in quantifying the chirality parameter from structural properties, analytical models are relatively scarce. A common prototypical model of a chiral medium is an isotropic (randomly oriented) and homogenous material of omega inclusions (**Figure 12**a).[222]

In Tellegen's relations, the chirality parameter $\tilde{\kappa}$ of such a medium can be found by solving Maxwell's equations for the particle, and is given by Oh and Hess[223] as:

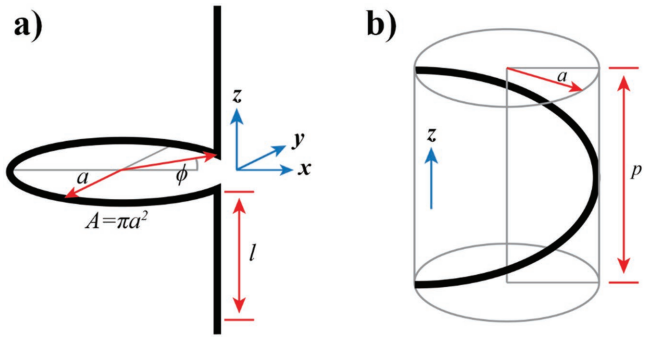

Figure 12. a) Schematic of a chiral "omega" structure. A material consisting of randomly oriented omega structures can be used as a prototypical chiral isotropic medium. b) Schematic of a chiral single-loop helix structure. The ratio between pitch p and radius a can be used to provide a value for the optimal chirality parameter of the effective medium.

$$\kappa = \frac{\Omega_k \omega_0 \omega}{{\omega_0}^2 - \omega^2 - i\omega\gamma}$$
$$\Omega_k = \frac{\mu_0 c_0 \alpha A N}{V_0 \omega_0} \tag{30}$$

The particle has a resonant frequency ω_0 and is driven by a field of frequency ω, with the speed of light in vacuum given by c_0. Here, the system acts as a damped harmonic oscillator where γ is the dissipation constant, $\alpha = l/L$, L is the inductance, l is the length of wire above and below the loop, and A is the cross-sectional area of loop, V_0 is the volume of the unit cell, and N is the number of inclusions per unit cell. This formalism is based on the work of Jaggard et al, in which the constitutive relations of such a medium were analytically investigated.[224] Similar work by Tretyakov et al. discussed such a medium in the context of analytically analyzing the α_{em} and α_{me} chirality parameters linking the induced dipole moments to the incident field (Equation (28)).[222]

Analytical expressions have also been derived for a material consisting of randomly oriented single-loop metallic helix structures (Figure 12b). It was found that for all such helix structures, the chirality parameter depends strongly on the radius and pitch of the helix. The work by Ge et al.[143] is based on the constitutive relation arrangement:

$$\mathbf{D} = \varepsilon \mathbf{E} + i\xi \mathbf{B}$$
$$\mathbf{H} = \mu^{-1} \mathbf{B} - i\xi \mathbf{E} \tag{31}$$

They show that, in this model, the chirality parameter is given by

$$\xi = \frac{NV\omega C}{4} = \frac{NV}{4\omega L} \tag{32}$$

Here, the material contains N inclusions per unit volume, V is the volume enclosed by the loop (given by $\pi a^2 p$ where a is the radius of the loop and p is the pitch), and C and L are the inclusion capacitance and inductance respectively. Interestingly, they find that for such a structure, the maximum chirality is achieved when the ratio $a/p = 1/\sqrt{2\pi} \approx 0.23$, allowing for the design of

chiral nanostructures based on helices to be optimized, in cases where this model acts as an accurate approximation.

4.2. Optical Chirality Parameters

The interaction between a chiral molecule and a chiral electromagnetic field is expected to exhibit a dissymmetry, in that each "handedness" of a chiral field should interact differently with a chiral molecule or nanostructure. A field with a shorter chiral pitch in the local EM field will exhibit a stronger interaction dissymmetry than a less twisted field. It had long been thought that the maximum possible chiral dissymmetry is obtained for a perfectly circularly polarized monochromatic field, however in 2010 Tang and Cohen proposed a setup in which the dissymmetry exceeds that of CPL (referred to as "superchiral light") at the nodes of a chiral standing wave.[225] The strength of the field chirality can be quantified by Lipkin's 00-zilch density,[226] referred to by Tang and Cohen[225] as the "optical chirality" C as given in Equation (33), or rewritten in the form of Equation (34).

$$C = \frac{\varepsilon}{2}\mathbf{E}\cdot(\nabla\times\mathbf{E}) + \frac{1}{2\mu}\mathbf{B}\cdot(\nabla\times\mathbf{B}), \tag{33}$$

which can be rewritten as:

$$C = -\frac{\varepsilon_0\omega}{2}\mathrm{Im}[\tilde{\mathbf{E}}(\mathbf{r})\cdot\tilde{\mathbf{B}}(\mathbf{r})], \tag{34}$$

where $\tilde{\mathbf{E}}$ and $\tilde{\mathbf{B}}$ denote the complex field amplitudes.

This quantity describes the angular momentum of the curl of the optical field[227] and is a conserved property of the field. The authors showed that the enantioselectivity of optical excitation of a molecule is highly dependent on C, and so it stands that such a superchiral field can lead to significant enhancement of the enantioselective excitation of chiral molecules.

The general response of a chiral molecule to a monochromatic electromagnetic field is described by an internal electric dipole moment $\tilde{\mathbf{p}}$ and magnetic dipole moment $\tilde{\mathbf{m}}$ as in Equation (29). For clarity, we rewrite this as in Equation (35).

$$\begin{aligned}\tilde{\mathbf{p}} &= \tilde{\alpha}_{ee}\tilde{\mathbf{E}} - i\tilde{\alpha}_{em}\tilde{\mathbf{B}}\\ \tilde{\mathbf{m}} &= i\tilde{\alpha}_{em}\tilde{\mathbf{E}} + \tilde{\alpha}_{mm}\tilde{\mathbf{B}}\end{aligned} \tag{35}$$

Here, $\tilde{\alpha}_{ee}$ and $\tilde{\alpha}_{mm}$ correspond to $\tilde{\alpha}$ and $\tilde{\chi}$ in references[225] and,[228] α_{ee} is the electric polarizability, α_{mm} is the magnetic susceptibility, and $\tilde{\alpha}_{em}$ is the mixed electric-magnetic polarizability. Physical quantities are obtained from the real parts of Equation (35). For an incident $\tilde{\mathbf{E}} = \tilde{\mathbf{E}}_0 e^{-i\omega t}$ and $\tilde{\mathbf{B}} = \tilde{\mathbf{B}}_0 e^{-i\omega t}$ the rate of excitation of a molecule from right (+) and left (–) CPL is given by Equation (36).[225,228]

$$A^{\pm} = \frac{\omega}{2}\left\langle \mathbf{E}\cdot\dot{\mathbf{p}} + \mathbf{B}\cdot\dot{\mathbf{m}}\right\rangle_t = \frac{\omega}{2}\mathrm{Im}(\tilde{\mathbf{E}}^*\cdot\tilde{\mathbf{p}} + \tilde{\mathbf{B}}^*\cdot\tilde{\mathbf{m}}) \tag{36}$$

Substituting Equation (35) into Equation (36) leads to Equation (37), which can be rewritten in terms of the generalized optical chirality C to give Equation (38).[228] Again, here $\tilde{\alpha}''_{em} = \mathrm{Im}(\tilde{\alpha}_{em})$.

$$A^{\pm} = \frac{\omega}{2}(\alpha''_{ee}\left|\tilde{\mathbf{E}}\right|^2 + \alpha''_{mm}\left|\tilde{\mathbf{B}}\right|^2) \pm \tilde{\alpha}''_{em}\omega\mathrm{Im}(\tilde{\mathbf{E}}^*\cdot\tilde{\mathbf{B}}) \tag{37}$$

$$A^{\pm} \simeq \frac{\omega}{2}(\alpha''_{ee}\left|\tilde{\mathbf{E}}\right|^2 + \alpha''_{mm}\left|\tilde{\mathbf{B}}\right|^2) \pm \tilde{\alpha}''_{em}\frac{2}{\varepsilon}C \tag{38}$$

The time-averaged electric and magnetic energy densities $\langle U_E\rangle_t = \frac{\varepsilon}{4}|\tilde{\mathbf{E}}|^2$ and $\langle U_B\rangle_t = \frac{1}{4\mu}|\tilde{\mathbf{B}}|^2$ can be introduced here, and substituted into Equation (38) to give the rate of excitation in terms of energy density as in Equation (39).

$$A^{\pm} \simeq \frac{2}{\varepsilon}\alpha''_{ee}\omega\left(\langle U_E\rangle_t + \gamma\langle U_B\rangle_t\right) \pm \tilde{\alpha}''_{em}\frac{2}{\varepsilon}C \quad \gamma = \frac{\alpha''_{mm}}{\alpha''_{ee}}\varepsilon\mu = \frac{\alpha''_{mm}}{\alpha''_{ee}}\frac{n^2}{c^2} \tag{39}$$

We can now define the dissymmetry factor g of the chiroptical interaction by Equation (40).

$$g = \frac{A^+ - A^-}{\frac{1}{2}(A^+ + A^-)} \tag{40}$$

In Tang and Cohens paper,[225] the magnetic energy density was disregarded as negligible. Under this assumption, the dissymmetry factor is found to be

$$g = -\frac{\alpha''_{em}}{\alpha''_{ee}}\frac{2C}{\omega\langle U_E\rangle_t} \tag{41}$$

Note that here, under this approximation, the dissymmetry factor splits into properties of the molecule only ($\alpha''_{em}/\alpha''_{ee}$) and properties of the field only ($2C/\omega\langle U_E\rangle_t$), however in the general case the dissymmetry factor cannot be separated in this way and is significantly more complex.[228]

The full expression accounting for magnetic energy density can be simplified by assuming a small dissymmetry factor such that $n^+ \approx n^-$, to give Equation (42).[228] The limitation in chiroptical enhancement is now clear: at regions of low electric energy density, the magnetic energy density is maximized and should not be considered negligible. The γ term in Equation (42) is then the key limiting factor for the dissymmetry enhancement. The energy density terms in the denominator can no longer be reduced to arbitrarily small values in order to continually increase chiral dissymmetry. However, the chiral dissymmetry can still be increased by reducing the total electromagnetic energy density, increasing the structural chirality parameter of the medium, and increasing optical chirality C of the electromagnetic field.

$$g = -\frac{\tilde{\alpha}''_{em}}{\alpha''_{ee}}\frac{2C}{\omega[\langle U_E\rangle_t + \gamma\langle U_B\rangle_t]} \tag{42}$$

4.3. Superchiral Light

In the previous section, we have seen in Equation (41) that enhanced dissymmetry factors can be achieved by taking advantage of different features such as local field intensity, local density of states (LDOS) and local optical chirality of the field. In the first reported experimental demonstration of enhanced enantiomeric selectivity,[18] Hendry et al. used an array of gammadion-shaped plasmonic nanostructures to generate fields with a high value of local optical chirality by localized surface plasmon excitation. The presence of a dielectric layer (molecules on the structure's surface) produced a shift of the local surface plasmon (LSP) resonance wavelength of the nanostructure array. The detection of superchiral light is based on the measurement of the wavelength shift which is attributed primarily to molecules on the surface within regions of strong near-field local optical chirality C. Then, an effective refractive index shift for both LCP and RCP illumination was retrieved and used to determine the dissymmetry factor $g = (n_R - n_L)/(n_R + n_L)$. The measured dissymmetry factor was found to be ~10^6 times greater than those observed by probing the same molecules in solution with LCP and RCP light. The authors point out that the local field enhancement by itself is not sufficient to account for the enhanced chiral response. Due to the symmetry of the metallic structures in this case, plasmon oscillations in different branches are coupled together to generate "superchiral" fields according to the local value of the Lipkins zilch Z^{00} reported in Equation (33), as depicted in **Figure 13**a.

A completely different approach to generating superchiral fields is used by Tang and Cohen. The authors report experimental results based on their original proposal:[229] an imperfect standing wave is formed between mirrors, resulting in superchiral nodes of the field. A thin film of chiral molecules is then held at these nodes. The regions of enhancement were too thin to detect through differential absorption measurements. Instead, a fluorescent chiral compound was used, and differential emission measured. The differential emission enhancement results from suppression of the pure electric dipole transitions due to the lower electric energy density that would otherwise produce a strong achiral background. At the nodes, this achiral background is reduced, and the electric dipole-magnetic dipole transitions responsible for CD become a fractionally larger part of the measured signal. The experiment was repeated without the end mirror, removing the standing wave. The "superchiral" setup resulted in a ≈10 times increase in dissymmetry factor g, however in this case the optical chirality C of the field itself is not uniquely high. The enhanced dissymmetry is born from the low electromagnetic energy density at the nodes of a superchiral standing wave. However, it is worth to note that, thanks to near-field localization effects, the dissymmetry factor enhancement reported by Hendry at al. is several orders of magnitude higher than the one experimentally obtained by Tang and Cohen.

Several works, aiming to find a deeper understanding of the origin of the enhancement of the dissymmetry factor and on the physical meaning of the Lipkins zilch Z^{00}, were devoted to the study of the interaction between chiral fields and matter. For example, Cameron and Barnett argue that Lipkin's zilches have limited physical meaning, since they do not actually have units of angular momentum.[227] Lipkin's zilches describe the angular momentum of the curl of the field, rather than that of the field itself. While Tang and Cohen use Lipkins zilch Z^{000} to explain their experimental results in the context of "superchiral" light, Cameron and Barnett propose that the physical quantity of interest is the ij-infra-zilch "helicity density" N^{000}. They show that, for a monochromatic wave, the time-averaged components of the Lipkin's zilch tensor are proportional to the product of the time-averaged helicity and the square of the driving angular frequency. Therefore, $Z^{000} = N^{000}$ for a plane monochromatic wave. They suggest that this proportionality is the reason for the apparent agreement between Tang and Cohen's theory and experimental results. However, the ij-infra-zilches, thus the helicity-density array, provide a more general description and physically meaningful measure of the chirality of the angular momentum of a field.

Moreover, there has been some debate about the role of orbital angular momentum (OAM) in optical interactions with chiral molecules out of paraxial regime. Indeed, it is established that within the paraxial approximation, the orbital angular momentum of a field cannot probe the chirality of a molecular system. Only spin (polarization) can result in enantioselective excitation of chiral molecules. Nevertheless, in general, the spin and orbital contributions to the total angular momentum cannot be considered separately. Rosales-Guzmán et al. demonstrated that, according to Tang and Cohen's calculations and definitions of the dissymmetry factor, certain beam profiles with OAM can enhance the chiroptical response of molecules in local regions when compared to CPL with no OAM.[230] They consider a coherent superposition of two linearly polarized Bessel beams, with complex amplitudes A and B and indices m = +1 and m = −1 respectively. It is noted that at the center of the Bessel beams, the transverse components of electric and magnetic fields vanish. However, longitudinal components survive.

For the Bessel beams considered, it is shown that the electric and magnetic fields oscillate with a $\pi/2$ relative phase shift and only the longitudinal components do not cancel, resulting in a non-zero value for optical chirality C from Equation (34). The authors show that, if either A or B = 0, then, at the center of the beam, the dissymmetry factor approaches the value of CPL. However, if $|A| \sim |B|$ then strong dissymmetry enhancement exists, at certain polarization angles, dependent on the relative phase shift between the two beams. Additionally, similar to observations by Tang and Cohen, as the amplitudes approach $|A| = |B|$, the total electric field at the center of the beam vanishes while dissymmetry increases. In the configuration proposed by Tang and Cohen, the molecular sample must be located carefully at the node of a standing wave. Here however, the two beams are co-propagating, and, under the right conditions, enhancement exists throughout the entire resulting beam volume, thereby removing the standing wave requirement. Finally, it should be noted that the enhanced dissymmetry in this case is achieved through a reduction of the energy density, like in the work by Tang and Cohen,[229] rather than through an enhancement of the local optical chirality C.

The origin of the enhanced dissymmetry was also investigated by Andrews and Coles,[231,232] using a quantum electrodynamic (QED) approach. They examined a range of possible

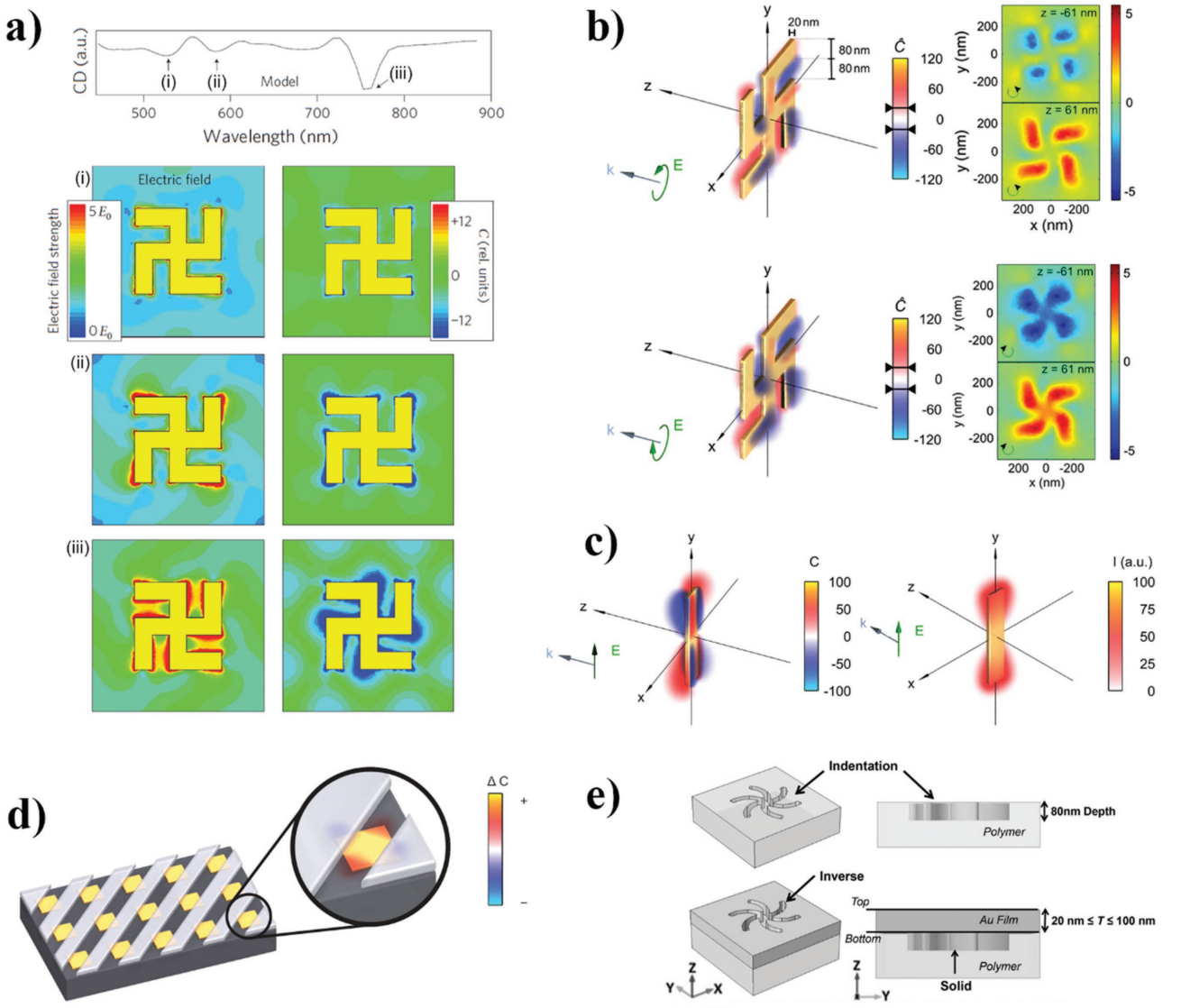

Figure 13. a) Left panels: Time-averaged electric field strength at the wavelengths marked in the top panel, when excited by LCP light. All fields are calculated at the substrate interface of the sample and normalized by the incident electric field (E_0). Right panels: Local optical chirality C, normalized by the magnitudes for LCP plane waves. Adapted with permission.[18] Copyright 2010, Nature Publishing Group. b) Optical chirality enhancement by a planar gammadion structure illuminated with LCP (top) and RCP (bottom) at a wavelength of 2.01 µm. Adapted under the Creative Commons Attribution License from reference[235] c) (Left) Optical chirality induced by a linear plasmonic nanoantenna illuminated with light polarized parallel to the antenna axis under normal incidence at resonance (217 THz). The values have been normalized by the optical chirality of CPL. (Right) The fundamental antenna mode exhibits strongest electric field intensity at the ends of the rod. The distribution differs significantly from the regions with strongest optical chirality. Adapted with permission.[236] Copyright 2012, Optical Society of America. d) Nanostructure geometry proposed for CD type measurements with incident linearly polarized light. When only two opposite corners of the array are accessible by chiral molecules, they experience a non-zero net optical chirality. Adapted with permission.[236] Copyright, 2012, Optical Society of America. e) Hybrid plasmonic "shurikens". Polymer substrate with an indentation that is 80 nm deep (top). A templated plasmonic substrate is produced after depositing Au with a thickness T which is varied from 20 to 100 nm (bottom). The walls of the structure will always have a thin layer of gold hence a continuous film will be formed. Adapted under the terms of the Creative Commons Attribution License.[122]

experimental configurations with attention paid to the setup proposed by Tang and Cohen. They show that the differential absorption rate between molecular enantiomers has two terms: One depending on the difference in the mean number of left- and right-handed photons $\overline{n}_R - \overline{n}_L$ (as expected), and a second term, depending sinusoidally on the distance z from the mirror. It is shown that this second term arises from, and is proportional to, the uncertainty in photon populations $\Delta n_L \Delta n_R$. They therefore claim that this second term is responsible for the enhancements reported by Tang and Cohen. An immediate implication of this is that in systems with precise photon number states, the differential absorption (CD) cannot exceed that of circularly polarized light, under any configuration of beams, since the second term vanishes due to zero uncertainty,

and the first term returns to a maximum at a beam of a single direction of CPL. The results of their study lead the authors to the conclusion that "although radiation states can exhibit additional chiral character by engaging orbital angular momentum, such features cannot produce exceptional signatures of chirality in the associated spectroscopy". Thus, only the optical spin angular momentum is relevant to CD measurements, and so introducing a physically distinct "superchiral" state is, they claim, redundant.

However, a complete QED theory to study chiroptical radiation matter interactions in the near-field has not been developed. From a basic point of view, standard quantization techniques cannot be applied when radiation-matter interactions at the nanoscale, with evanescent, non-propagating fields are considered.[233,234] In the meanwhile, many authors proposed different schemes to combine local field enhancements due to plasmon resonance and near-field patterns with high values of local optical chirality. Schäferling et al.[235] performed an extensive and detailed set of calculations to show that electromagnetic fields with strong optical chirality can be formed in the near-field of chiral plasmonic nanostructures. Their analysis aimed to identify the design principles for obtaining regions of very high local optical chirality. It is interesting to note that regions of positive and negative optical chirality are obtained thanks to localized plasmon excitation both when RCP and LCP incident light is considered (Figure 13b). This result is an indication of the fact that the near-field produced by a plasmonic structure can exhibit regions of high optical chirality even in a system with no geometric chirality at all.

In a further work by the Giessen group,[236] it is demonstrated through numerical simulations that a 3-dimentionally achiral structure, such as a simple metallic rod, driven by a linearly polarized field in the y-direction (along the length of the rod), produces both regions of strong field enhancement and regions of high optical chirality. The authors show that the optical chirality is not just an artefact of local field enhancement; it appears in different regions with respect to the field enhancement, as shown in figure (Figure 13c). Due to the symmetry of the system, the integral of the optical chirality over the whole system vanishes. For this reason, far-field optical chirality must be zero. They propose that the optical chirality forms from the interference between the incident and scattered fields showing that the magnetic component of the incident field, only present in x, interacts with the x-component of the scattered electric dipole field. The alternating sign of the optical chirality is therefore attributed to the distribution of the x-component of the scattered electric dipole field.

This analysis leads to a proposal of a new chiroptical spectroscopy setup, where linearly polarized light excites achiral structures to form alternating regions of local optical chirality. However, regions of a particular sign are blocked by additional features, meaning that doped molecules can only bind to regions of the opposite sign of optical chirality, resulting in a net enantioselectivity (Figure 13d).

Davis and Hendry[237] provided another theoretical and numerical demonstration of local fields of non-zero optical chirality, from a geometrically achiral system. The optical chirality of these local fields largely exceeds that of propagating circularly polarized light. The effect is attributed to interactions between the magnetic component (of the local surface plasmon evanescent field) and the electric component of the incident field. Unlike circularly polarized light, the local chiral fields do not rotate in time. In this sense, the field is spinless, like those described by Rosales-Guzmán.[230] The chirality is again described by longitudinal field components, in this case due to the interaction between the incident and evanescent fields, leading to local regions of non-zero optical chirality. The effects of chiral near-fields produced by plasmonic nanostructures were also experimentally investigated by Meinzer et al,[238] The authors reported measures of the chiral dissymmetry in the enhanced luminescence of achiral molecules in the presence of chiral plasmonic nanostructures. Optical chirality C of the near-field is calculated, and compared to the differential enhancement in photoluminescence between LCP and RCP excitation. Despite the far-field CD of the nanostructures being weak ($\sim 10^{-5}$), the observed near-field dissymmetry is found to be $\sim 10^{-1}$, showing significant enhancement. This enhancement is attributed to the high optical chirality of plasmonic near-fields, exceeding that of CPL.

Similarly, Schäferling et al. proposed plasmonic helix nanoantennas that support chiral eigenmodes.[158] According to the authors' findings, high optical chirality occurs within the volume inside the helices. Molecular chiroptical spectroscopy measurements, within these regions, is expected to provide a 2 orders of magnitude enhancement, compared to probing with CPL.

Thanks to these promising results, several efforts have been devoted to the exploration of possible low-cost applications for disposable and tunable chiroptical devices. For example, Karimullah et al.[122] proposed plasmonic shuriken nanostructures on a polycarbonate substrate. A templating technique (highlighted in Section 3.2) is used to develop a means of rapid production. In this study the nanostructure had a shuriken shape, as depicted in figure (Figure 13e). The thickness of this top film can be varied, and is found to significantly affect the optical properties of the material. In this case, detection of nearby molecules can be performed by measuring the shift in the LSP resonances.[18]

The same structures have been used for the experimental demonstration of enhanced polarimetry for detection of picogram quantities of proteins, utilizing evanescent near-field superchiral regions.[19] The authors attribute the increase in sensitivity to the steep field gradients of the evanescent fields. These gradients enhance the enantioselective quadrupolar molecular excitations. Simulations show the chiral dissymmetry of the local fields to be an order of magnitude greater than that of circularly polarized light.

Beside the promising and stimulating experimental results on superchiral light, the concept should be approached carefully. For example, Finazzi et al. suggest, through FDTD simulations, that for sub-wavelength nanoparticles in real metals, there is a fundamental limitation in their ability to generate local fields of high average optical chirality.[239] Furthermore, in order to realize plasmonic enhancement of chiroptical measurements, the authors propose two methods: either to place molecules in specific regions where the nanostructure generates high optical chirality, or to ignore superchirality entirely and improve sensitivity through the plasmon enhanced local field intensity.

According to Equation (34), regions of high optical chirality require the electric and magnetic fields to be parallel. This condition is not found in propagating plane waves, however it can be easily achieved in evanescent near-field configurations.

Liu et al.[240] show, through simulations, that superchiral fields can form in hotspots created by surface plasmon resonances in achiral nanoparticle dimers. The authors show that the CD is not related to the hotspot intensity in the gap between the nanoparticles. Instead, the CD is found to be related to the optical chirality. Although in some cases, the CD spectrum corresponded well to the extinction spectrum, this was not generally true. Generally, the spectral positions of CD peaks/valleys corresponded well to the spectral positions of local optical chirality peaks/valleys. As a further evidence, experimental data are cited[241] that show how extinction (local intensity) does not correlate well to the measured CD. Liu et al. ran simulations of the expected CD and find those to be in good agreement with the experimental results, highlighting the role of optical chirality. The proposed analysis is in contrast to the mechanism cited by Zhang and Govorov.[242]

Optical chirality has also been discussed, beyond nanoparticles (in the context of propagating surface plasmon waves)[243] and beyond linear optics. Valev et al.[244] showed that both the chiral dissymmetry factor g and the second harmonic polarization $P_i(2\omega)$ are sensitive to the same electric quadrupole terms $q_{ijk} = E_i\nabla_j E_k$. Regions of high optical chirality could therefore correspond to regions of high intensity nonlinear emission. Since second-harmonic generation is highly sensitive to structural chirality, this results in an enhancement in measurable SHG chiroptical effects such as SHG-CD (discussed in Section 5).

To summarize, in very recent years, the superchiral light concept has grown into a fertile topic. Theoretical efforts were devoted to the understanding of optical near-fields that arise from light-matter interactions in chiral nanostructures.[245] It has been pointed out[233,234] that near-field spectroscopy could reveal new and interesting phenomena because in the presence of evanescent and/or longitudinal fields, standard response theory can no longer be applied, and the source and object have to be treated electrodynamically as one system. A clear physical interpretation of the relation between optical chiral density, enhanced dissymmetry, selectivity, and scattering properties could finally lead to the development of optimized characterization techniques for chiral molecules on plasmonic nanostructured templates.

4.4. Negative Refractive Index

Nanomaterials enable the emergence of specific optical properties through design of the material geometry. For instance, such designs could lead to negative refractive index materials. The effects of negative refractive index (NRI) on light travelling through a medium were first described by Veselago,[246] who considered a medium with simultaneously negative permittivity ε and permeability μ. He showed that a plate of negative index material could bring light from a point source close to the material to a second focus some distance behind the plate (**Figure 14**a), and suggested possible applications as a type of lens. The full potential of negative index lensing was later investigated by Pendry, considering both the propagating and evanescent wave contributions to image resolution.[247] Unlike traditional lenses where the evanescent waves decay with no chance of recovery, a negative-index material (NIM) lens amplifies these waves. The ability to restore the amplitude and phase of evanescent and propagating waves respectively results in a "perfect lens", able to image at resolutions beyond the diffraction limit.

Negative refractive index typically relies on simultaneous electric and magnetic resonances. This was first achieved experimentally by creating a composite metamaterial of both electric and magnetic resonators such as split-ring resonators (Figure 14b).[248] The magnetic resonance is provided by the split-ring (left), which acts as an LC (inductor-capacitor) circuit. Incident light drives a current I around the outer ring, forming a current loop and thus acting as an inductor. Charge builds up at the gap in the ring, resulting in a small capacitance acting against the induced current. The combined effect of these results in a magnetic resonance. The inner ring then provides a large capacitive load in the gap between the concentric rings, resulting in a lowered magnetic resonant frequency of the whole split-ring structure.[249] When combined with a simple wire (right) providing an electric resonance via dipole excitation at the same frequency, negative refractive index can be achieved. A wire lattice has a cutoff frequency below which ε is negative and the split-ring achieves negative μ above the SRR frequency. Compared to a single SRR, a double SRR has lower resonance frequency, which helps to achieve a region of spectral overlap, where both ε and μ are negative.[250] This method however can be difficult to scale to shorter wavelengths, due to the composite nature of the inclusions.

An alternative route is to use a chiral metamaterial. It was shown in Section 4.1 that a chiral medium, one with a nonzero chirality parameter κ, causes LCP and RCP waves to propagate through the medium with different refractive indices. Equation (27) shows that if the magnitude of the chirality parameter is high enough such that $|\kappa| > \sqrt{\varepsilon_r \mu_r}$, the refractive index for one handedness of light will become negative.

This mathematical framework was discussed by Tretyakov et al. by considering a medium with a chirality parameter $|\kappa| = \sqrt{\varepsilon_r \mu_r}$. Such a material would achieve "chiral nihility", with simultaneously vanishing ε and μ for one handedness of CPL. Tretyakov et al. also mentioned that a high chirality parameter could cause the effective refractive index to become negative.[251] Pendry presented the larger implications of negative refractive index.[252] He suggested that the design of a negative index perfect lens can be simplified by making use of a chiral resonance, mathematically describing the conditions required to develop such a material. Since achieving negative index in this scheme relies on a large chirality parameter κ, such metamaterials also lead to large chiroptical effects. This makes them well suited for ultra-thin optical components, for instance as CPL absorbers and polarizers.

The idea of constructing an effective medium with negative refractive index has also been theoretically suggested as a way to achieve repulsive Casimir forces. Zhao et al. proposed applications of this concept in nano-levitation, leading to extremely low friction nano-motors.[253] However, it has since been shown

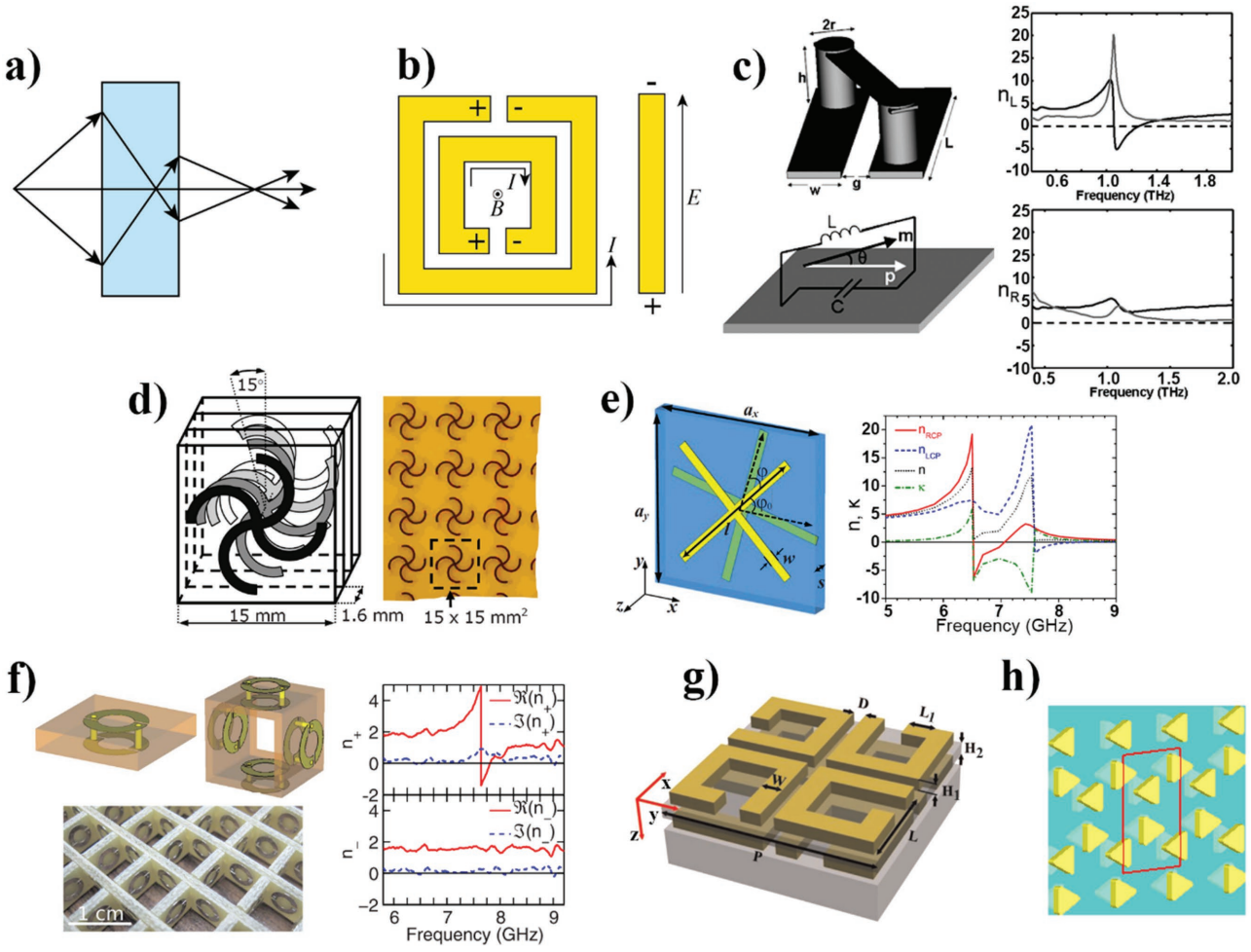

Figure 14. a) As divergent rays of light propagate through a negative refractive index material, they form a focus within the slab, and upon emerging are brought to a second focus behind the slab. This is the basis for using negative index to create a perfect lens. b) Schematic of a split-ring resonator structure based on the negative-index metamaterial demonstrated in ref. [248], showing both magnetic (left) and electric (right) resonators. c) (Left) chiral LC resonator structure. Chirality is introduced in the angle of the cross bar Θ. (Right) Experimentally retrieved refractive index for LCP (top) and RCP (bottom), showing region of negative index for LCP light. Reproduced with permission.[258] Copyright 2009, American Physical Society. d) Chiral "double-S" structure with 3-dimenisioinal chirality due to the angular shift between layers. Reproduced with permission.[259] Copyright 2009, American Physical Society. e) (Left) stacking of achiral cross structures with an angle between layers results in 3-dimenisonal chirality. (Right) Retrieved refractive index from simulations, for LCP (blue) and RCP (red), showing region of negative index for RCP light. Reproduced with permission.[261] Copyright 2009, American Physical Society. f) (Left) PCB grid of chiral split-ring resonators forming a chiral 3D metamaterial. (Right) Experimentally retrieved refractive index for LCP (n_- bottom) and RCP (n_+ top), showing region of negative index for RCP light. Reprinted from[262] with the permission of AIP Publishing. g) Asymmetric chiral split-ring structure analyzed numerically, to show a strong dependence of the chiroptical response on structure geometry. Reprinted from[263] Copyright 2015 with permission from Elsevier. h) Bi-layered metamaterial consisting of triangular elements, numerically analyzed to demonstrate negative index. Reproduced with permission.[265] Copyright 2014, Elsevier.

that a repulsive Casimir would be quite difficult, in such nanomaterials.[254,255] The problem arises because, at the length scales involved, Van der Waals interactions dominate and, consequently, the effective-medium approximations break down. It was later suggested that highly chiral nanomaterials could instead lead to a reduction of Casimir attraction by around 90%, rather than leading to repulsion as originally proposed.[256]

A number of chiral negative-index metamaterials have been demonstrated both numerically and experimentally. Research has focused largely on planar chiral metamaterials in the GHz and THz regime. However, a notable exception is found in experiments by Wiltshire and Pendry,[257] in which the proposal discussed previously by Pendry[252] is realized and experimentally verified to exhibit negative index at ~80 MHz radio frequencies (≈3.7 μm). The chirality parameter was measured directly by examining the magnetic response to an applied electric field across the structure, via the current induced in a wire loop around the center of the structure. Although only a single structure was examined, an isotropic bulk medium consisting of these would exhibit negative-index within the same frequency band.

Zhang et al.[258] demonstrated that chirality can be introduced into the geometry of an LC resonator metamaterial consisting of cross-wires connected between two layers (Figure 14c). The chirality is introduced by tilting the resonator loop out of the plane with its gap. The structure, in this particular geometry,

was found to exhibit negative refractive index in the infrared region (~1 THz, ~300 μm), which was verified through numerical simulations. Around the same time, Plum et al.[259] demonstrated a GHz negative index metamaterial by utilizing multiple stacked layers of a chiral double-S crossed geometry (Figure 14d), revealing a band of negative-index between 5–6 GHz (50–60 mm) for an optimized, 4-layered version of the structure. This principle was further developed by Zhou et al.,[260] where a bi-layered chiral metamaterial based on conjugated gammadion structures was found to exhibit large optical activity and negative index around a 6 GHz (60 mm) resonance, in both experiments and numerical simulations. In both of these examples, the chirality cannot be directly measured. Instead, a parameter retrieval method is used to obtain properties, such as impedance and effective refractive index, from transmission and reflection coefficients (referred to as S-parameters).

Similar work later demonstrated chiral negative index in multi-layered metamaterials that are achiral within a single layer.[261] Two layers of an achiral cross structure, with a rotation between layers (Figure 14e), were shown to exhibit strong polarization rotation and negative index for GHz radiation. Beyond multi-layered planar structures, other three-dimensional geometries have been shown to exhibit negative refractive index, for example a grid of crossed printed circuit board (PCB) strips has been used as substrate for an array of chiral split-ring resonators (Figure 14f).[262] This three-dimensional non-planar metamaterial was experimentally and numerically found to exhibit strong optical rotation and CD in the GHz region, with a band of negative index around 7–8 GHz (≈40 mm).

Fabrication of metamaterials operating at IR and visible wavelengths pose significant challenges even though fabrication techniques are improving. By contrast, in recent years, the availability and efficiency of computational power has increased faster, allowing for a large set of structure geometries to be analyzed and optimized numerically.

The work by Jia et al.[263] provides an example of such simulated optimization. It demonstrates the ability to tune a relatively simple geometric parameter of a metamaterial to maximize the chirality, and achieve negative refractive index, within a desired frequency range. A bi-layered material based on asymmetric split-ring resonators (Figure 14g) was shown to exhibit negative refractive index in the NIR, with a dependence on the geometric parameter responsible for the inclusion asymmetry (L_1 in Figure 14g). By simulating many variations of this structure, the system could be optimized, and also give insight into the underlying mechanism, due to the ability to visualize charge and current density within the material. By optimizing a hollowed out (inverted) split-ring resonator structure, Jia et al. later demonstrated a metamaterial in which LCP and RCP light had five and eight refractive index frequency bands respectively between 100 THz and 900 THz.[264] In addition to using the simulations to optimize chirality, it was also shown that increased ring width and the size of the missing part of the ring (that gives the SRR its name) can blue-shift these resonances.

A wide range of structure types have been numerically investigated and demonstrated negative refractive index. For example, Giloan and Astilean[265] demonstrated negative index in a bi-layered planar metamaterial consisting of triangular gold elements (Figure 14h). Fang et al.[266] demonstrated a less common approach to inducing 3D chirality, by using a trench to "sink" the central region of a gammadion structure, resulting in strong chirality. This again was shown to exhibit strong optical rotation and negative refractive index in NIR radiation. Despite this, designs for chiral NIMs in the visible region remain somewhat elusive. Simulations have demonstrated negative index in achiral[267] and chiral[268] metamaterials through simultaneous resonances, however visible NIMs remain in the early stages of research.

4.5. Chiral Optical Forces

Optical trapping designates methods for capturing, translating or guiding particles with laser light. In the last years, several applications have been developed in physical, chemical, and biological fields, taking advantage of optical forces' capability of pushing,[269] trapping,[270,271] and pulling[272] small molecules as well as micron-sized particles. In general, optical forces can be decomposed into their longitudinal and transverse components, which are parallel and perpendicular to the direction of light propagation, respectively. In particular, transverse or lateral optical forces (LOF) have recently attracted considerable attention through the discovery of unusual light modes with complex field topologies.[273,274] However it has been shown that even for a single linearly polarized plane wave[220] or evanescent wave,[275] a chiral particle near a substrate can be subject to an LOF. The direction of this additional lateral force depends on the chirality of the molecule making it possible to obtain enantiomeric selection by mechanical separation.

In order to obtain an intuitive understanding of the origin of the optical force, we start from the expression of the time-averaged force acting on a dipolar chiral particle:[276]

$$\langle \mathbf{F} \rangle = \frac{1}{2}\mathrm{Re}\left[\left(\nabla \tilde{\mathbf{E}}^*\right)\cdot \tilde{\mathbf{p}} + \left(\nabla \tilde{\mathbf{H}}^*\right)\cdot \tilde{\mathbf{m}} - \frac{ck_0^4}{6\pi}\left(\tilde{\mathbf{p}}\times \tilde{\mathbf{m}}^*\right)\right], \tag{43}$$

where $\mathbf{E} = \frac{1}{2}(\tilde{\mathbf{E}} + \tilde{\mathbf{E}}^*)$ and $\mathbf{H} = \frac{1}{2}(\tilde{\mathbf{H}} + \tilde{\mathbf{H}}^*)$ are the electric and magnetic fields of the electromagnetic wave with vacuum wavenumber k_0 acting on the chiral molecule; the induced electric and magnetic moments of the chiral particle are defined by

$$\begin{bmatrix} \tilde{\mathbf{p}} \\ \tilde{\mathbf{m}} \end{bmatrix} = \begin{bmatrix} \tilde{\alpha}_{ee} & i\tilde{\alpha}_{em} \\ -i\tilde{\alpha}_{em} & \tilde{\alpha}_{mm} \end{bmatrix} \begin{bmatrix} \tilde{\mathbf{E}} \\ \tilde{\mathbf{H}} \end{bmatrix}, \tag{44}$$

where $\tilde{\alpha}_{ee}, \tilde{\alpha}_{em}, \tilde{\alpha}_{mm}$ are complex quantities. Substituting Equation (44) in (43), we obtain:

$$\begin{aligned} \langle \mathbf{F} \rangle = \frac{1}{2}\mathrm{Re}\Big[& \alpha_{ee}\left(\nabla \tilde{\mathbf{E}}^*\right)\cdot \tilde{\mathbf{E}} + \tilde{\alpha}_{mm}\left(\nabla \tilde{\mathbf{H}}^*\right)\cdot \tilde{\mathbf{H}} + i\tilde{\alpha}_{em}\left(\nabla \tilde{\mathbf{E}}^*\right)\cdot \tilde{\mathbf{H}} \\ & - i\tilde{\alpha}_{em}\left(\nabla \tilde{\mathbf{H}}^*\right)\cdot \tilde{\mathbf{E}} - \frac{ck_0^4}{6\pi}\left(\tilde{\alpha}_{ee}\tilde{\mathbf{E}} + i\tilde{\alpha}_{em}\tilde{\mathbf{H}}\right)\times\left(\tilde{\alpha}_{mm}^*\tilde{\mathbf{H}}^* + i\tilde{\alpha}_{em}^*\tilde{\mathbf{E}}^*\right)\Big] \end{aligned} \tag{45}$$

It can be shown that the first and second term of Equation (45) can be written as[220]:

$$\mathrm{Re}\left[\tilde{\alpha}_{ee}\left(\nabla\tilde{\mathbf{E}}^{*}\right)\cdot\tilde{\mathbf{E}}\right]=\frac{1}{2}\alpha'_{ee}\nabla|\mathbf{E}|^{2}+2\omega\mu_{0}\alpha''_{ee}\langle\mathbf{S}\rangle+\frac{2\omega}{\varepsilon_{0}}\alpha''_{ee}\nabla\times\langle\mathbf{L}_{e}\rangle, \quad (46)$$

$$\begin{aligned}\mathrm{Re}\left[\tilde{\alpha}_{mm}\left(\nabla\tilde{\mathbf{H}}^{*}\right)\cdot\tilde{\mathbf{H}}\right]&=\frac{1}{2}\alpha'_{mm}\nabla|\mathbf{H}|^{2}+2\omega\mu_{0}\alpha''_{mm}\langle\mathbf{S}\rangle\\&+\frac{2\omega}{\mu_{0}}\alpha''_{mm}\nabla\times\langle\mathbf{L}_{m}\rangle.\end{aligned} \quad (47)$$

Where $\langle\mathbf{S}\rangle=\frac{1}{2}\mathrm{Re}[\tilde{\mathbf{E}}\times\tilde{\mathbf{H}}^{*}]$ is the time-averaged Poynting vector and

$$\langle\mathbf{L}_{e}\rangle=\frac{\varepsilon_{0}}{4\omega}\mathrm{Im}\left(\tilde{\mathbf{E}}\times\tilde{\mathbf{E}}^{*}\right), \quad (48)$$

$$\langle\mathbf{L}_{m}\rangle=\frac{\mu_{0}}{4\omega}\mathrm{Im}\left(\tilde{\mathbf{H}}\times\tilde{\mathbf{H}}^{*}\right), \quad (49)$$

are the electric and magnetic parts of the time-averaged spin angular momentum (SAM) densities associated with the polarization of light. For the cross-coupling terms, we have:

$$\begin{aligned}\mathrm{Re}\left[i\tilde{\alpha}_{em}\left(\nabla\tilde{\mathbf{E}}^{*}\right)\cdot\tilde{\mathbf{H}}-i\tilde{\alpha}_{em}\left(\nabla\tilde{\mathbf{H}}^{*}\right)\cdot\tilde{\mathbf{E}}\right]&=-\alpha'_{em}\mathrm{Im}\left[\nabla\left(\tilde{\mathbf{H}}\cdot\tilde{\mathbf{E}}^{*}\right)\right]\\&-4\omega^{2}\alpha''_{em}\left[\langle\mathbf{L}_{m}\rangle+\langle\mathbf{L}_{e}\rangle\right]-2\alpha''_{em}\nabla\times\langle\mathbf{S}\rangle\end{aligned} \quad (50)$$

The last part of the equation can be written as:

$$\begin{aligned}&-\frac{ck_{0}^{4}}{6\pi}\left(\tilde{\alpha}_{ee}\tilde{\mathbf{E}}+i\tilde{\alpha}_{em}\tilde{\mathbf{H}}\right)\times\left(\tilde{\alpha}^{*}_{mm}\tilde{\mathbf{H}}^{*}+i\tilde{\alpha}^{*}_{em}\tilde{\mathbf{E}}^{*}\right)\\&=-\frac{ck_{0}^{4}}{6\pi}\Big\{2(\alpha'_{ee}\alpha'_{mm}+\alpha''_{ee}\alpha''_{mm}+\alpha'^{2}_{em}+\alpha''^{2}_{em})\langle\mathbf{S}\rangle\\&-\frac{4\omega}{\varepsilon_{0}}(\alpha'_{ee}\alpha'_{em}+\alpha''_{ee}\alpha''_{em})\langle\mathbf{L}_{e}\rangle\\&-\frac{4\omega}{\mu_{0}}(\alpha'_{mm}\alpha'_{em}+\alpha''_{mm}\alpha''_{em})\langle\mathbf{L}_{m}\rangle\\&-(\alpha'_{mm}\alpha''_{ee}-\alpha'_{ee}\alpha''_{mm})\mathrm{Im}(\tilde{\mathbf{E}}\times\tilde{\mathbf{H}}^{*})\Big\}\end{aligned} \quad (51)$$

Combining equations (46)–(51) we obtain the final expression for the force[277]:

$$\begin{aligned}\langle\mathbf{F}\rangle&=\nabla U+\frac{\sigma}{c}\langle\mathbf{S}\rangle-\alpha''_{em}\nabla\times\langle\mathbf{S}\rangle+c\sigma_{e}\nabla\times\langle\mathbf{L}_{e}\rangle\\&+c\sigma_{m}\nabla\times\langle\mathbf{L}_{m}\rangle+\omega\gamma_{e}\langle\mathbf{L}_{e}\rangle+\omega\gamma_{m}\langle\mathbf{L}_{m}\rangle\\&+\frac{ck_{0}^{4}}{12\pi}(\alpha'_{mm}\alpha''_{ee}-\alpha'_{ee}\alpha''_{mm})\mathrm{Im}\left(\tilde{\mathbf{E}}\times\tilde{\mathbf{H}}^{*}\right)\end{aligned} \quad (52)$$

where:

$$U=\frac{1}{4}\alpha'_{ee}|\mathbf{E}|^{2}+\frac{1}{4}\alpha'_{mm}|\mathbf{H}|^{2}-\frac{1}{2}\alpha'_{em}\mathrm{Im}\left[\left(\tilde{\mathbf{H}}\cdot\tilde{\mathbf{E}}^{*}\right)\right], \quad (53)$$

$$\sigma_{e}=\frac{k_{0}\alpha''_{ee}}{\varepsilon_{0}}, \quad (54)$$

$$\sigma_{m}=\frac{k_{0}\alpha''_{mm}}{\mu_{0}}, \quad (55)$$

$$\sigma=\sigma_{e}+\sigma_{m}-\frac{c^{2}k_{0}^{4}}{6\pi}(\alpha'_{ee}\alpha'_{mm}+\alpha''_{ee}\alpha''_{mm}+\alpha'^{2}_{em}+\alpha''^{2}_{em}), \quad (56)$$

$$\gamma_{e}=-2\omega\alpha''_{em}+\frac{ck_{0}^{4}}{3\pi\varepsilon_{0}}(\alpha'_{ee}\alpha'_{em}+\alpha''_{ee}\alpha''_{em}), \quad (57)$$

$$\gamma_{m}=-2\omega\alpha''_{em}+\frac{ck_{0}^{4}}{3\pi\varepsilon_{0}}(\alpha'_{mm}\alpha'_{em}+\alpha''_{mm}\alpha''_{em}). \quad (58)$$

The first term of the force, $\langle\mathbf{F}\rangle_{grad}=\nabla U$, corresponds to the gradient force. The second term, proportional to the time-averaged Poynting vector modulus, represents the radiation pressure $\langle\mathbf{F}\rangle_{rad}=\frac{\sigma}{c}\langle\mathbf{S}\rangle$. The third, fourth and fifth terms represent the force due to the curl of the time-averaged spin angular momentum (SAM) densities plus the curl of $\langle\mathbf{S}\rangle$ that is recruited by the particle chirality $\alpha''_{em}\,\alpha''_{em}$: $\langle\mathbf{F}\rangle_{curl}=\nabla\times(c\sigma_{e}\langle\mathbf{L}_{e}\rangle+c\sigma_{m}\langle\mathbf{L}_{m}\rangle-\alpha''_{em}\langle\mathbf{S}\rangle)$. The sixth and seventh terms correspond to a force that is originated by the coupling of the particle chirality to SAM densities: $\langle\mathbf{F}\rangle_{chir}=\omega\gamma_{e}\langle\mathbf{L}_{e}\rangle+\omega\gamma_{m}\langle\mathbf{L}_{m}\rangle$. For achiral particles $\gamma_{e}=\gamma_{m}=0$ and this term vanishes. Finally, the last term is related to an alternating flow of the stored energy in the particle, it vanishes for a plane wave, where $\mathrm{Im}(\tilde{\mathbf{E}}\times\mathbf{H}^{*})=0$.

We note that there is a contribution due to the chirality of the particle to $\langle\mathbf{F}\rangle_{grad}$, $\langle\mathbf{F}\rangle_{rad}$ and, $\langle\mathbf{F}\rangle_{curl}$, however they are non-zero also for achiral particles. On the other hand, $\langle\mathbf{F}\rangle_{chir}$ is exclusively related to the chiral response of the particle. Depending on the system under investigation different contributions can arise from different terms.[278,279] For chiral particles, the most interesting property is that the resulting forces and torques are dependent on the handedness, through the terms γ_{e} and γ_{m}, that are both depended on $\tilde{\alpha}_{em}$ in Equation (44). This opens up intriguing possibilities to mechanically separate chiral objects according to their handedness, using chiral light forces.

Different works report both numerical and experimental results showing pulling as well as lateral forces and torques on chiral dipoles and/or on chiral dimers. For example, in reference[220] it is numerically and analytically shown that a lateral force acting on a chiral particle originates from the presence of a substrate, even for a linearly polarized incident light. In this case, the handedness of the particle, in combination with light reflected from the substrate surface, gives rise to a non-zero lateral force. This "sideways" force pushes the particles in different direction depending on their handedness. The authors show that for an incident plane wave propagating along the *x*-direction and polarized along the *z*-direction, in the presence of a substrate, the lateral component of the Poynting vector becomes asymmetric (see **Figure 15**a (ii)) and hence contributes to a lateral radiation pressure. Moreover, the presence of the reflected field from a non-magnetic substrate is responsible for a non-vanishing electric SAM density

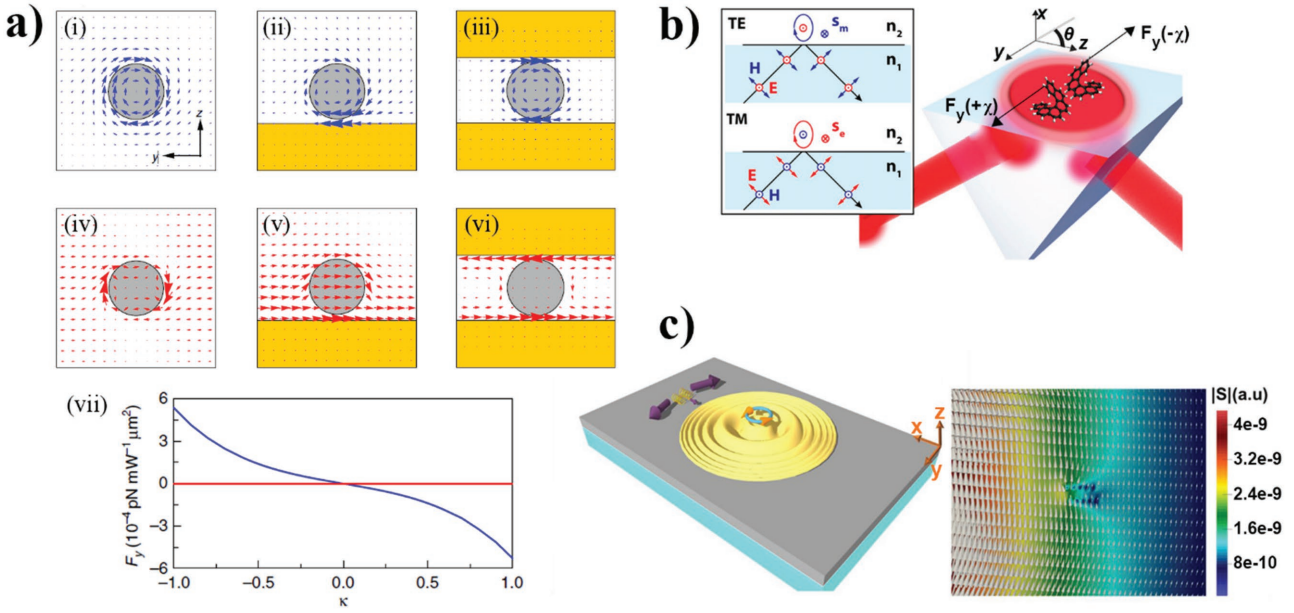

Figure 15. a) Time-averaged Poynting vectors (i) for an isolated chiral sphere, (ii) for a chiral sphere above a gold substrate and (iii) for a chiral sphere sandwiched symmetrically by two gold substrates. Time-averaged electric spin density (iv) for the isolated sphere, (v) for the sphere above a gold substrate and (vi) for the sphere sandwiched by two gold substrates. (vii) Lateral force acting on the chiral sphere above a gold substrate (blue) and sandwiched by two gold substrates (red) as a function of the chirality parameter κ. The blue line shows that the sign of the lateral force F_y depends on κ and it is zero for achiral particles ($\kappa = 0$). The red line indicates the lateral force vanishes in the sandwiched case. Adapted with permission.[220] Copyright 2014, Nature Publishing Group. b) Chirality-dependent lateral forces in an evanescent field. An evanescent field arises as light in a high index medium (n_1) is totally internally reflected at the interface with a low index medium (n_2) at an angle θ beyond the critical angle. Particles in an evanescent field with transverse spin angular momentum experience lateral forces depending on their chiral polarizability, with particles with opposite helicities experiencing lateral forces in oppose directions. (Inset) Totally internally reflected transverse electric (TE) and transverse magnetic (TM) waves give rise to evanescent waves that have transverse spin due to their elliptically polarized magnetic and electric fields. Adapted with permission.[275] Copyright 2015, National Academy of Sciences. c) Schematics of exciting a chiral SPP by a near-field circularly polarized dipole (left). The distribution of the E_z component of a SPP excited by a near-field circular dipole on the x-y plane (right). It is clearly seen that the SPP inherits the circular character of the source. Reproduced with permission.[284] Copyright 2015, American Chemical Society.

(see Equation (48) and Figure 15a (v)), which can also enable the $\langle \mathbf{F} \rangle_{\text{chir}}$ contribution.

According to these basic principles, a chiral optomechanical separation scheme has been experimentally achieved on the micro-scale using circular Bragg reflection.[280] The authors show that material chirality can be sorted in a fluidic environment by chiral light forces. With the aim to downsize this effect to the nanoscale, which is the relevant range for chiral biomolecules, several theoretical proposals have been made. A promising possibility is to use evanescent waves, related to excitation of surface plasmon polaritons. Indeed, it has recently been shown that, under evanescent waves illumination, the interplay between chiral particles and optical SAM produces lateral forces that push in the direction of the SAM vector, or opposite to it, depending on the handedness, as shown in Figure 15b.[275]

The recent developments on enhanced chiral response in the near-field, mediated by excitation of localized surface plasmon polaritons suggest a further development of the potential application of optical forces in chiral systems.[243,281–284]

For example, in reference[281] the authors numerically show that the optical force experienced by a chiral sphere, in relation to a surface plasmon mode, has a component along a direction perpendicular to the plasmon linear momentum. Moreover, this direction depends on the handedness. The physical origin of this lateral force resides in the transfer of electric plasmonic transverse spin angular momentum $\langle \mathbf{L}_e \rangle$ to transverse linear momentum. It is the chirality that mediates this transfer for the particle. The authors consider both dissipative and non-dissipative systems with separate discussion for chiral spheres with either circular dichroism (imaginary part of the chiral parameter κ) or optical rotation (real part of κ) respectively. Moreover, a multipolar analysis was performed to examine the role of quadrupolar contributions. Interesting, in the case of larger particles, the lateral forces reversed sign. This reversal was not observed within the dipolar approximation.

The ability to control near-field properties by using plasmonic nanostructures[225] made it possible to find a connection between optical forces exerted on a chiral molecule (described through its chiral parameter κ) by a sculpted near-field (characterized by the optical chirality C as defined in Equation (33)). In particular, it has been shown that for a system exhibiting optical rotation (real part of κ) the reactive chiral force acting on a chiral molecule can be written as a function of the optical chirality C as:[282]

$$\langle \mathbf{F} \rangle_{\kappa}^{r} = \text{Re}(c\tilde{\kappa}) \frac{c}{\omega} \nabla C. \tag{59}$$

By contrast, the dissipative chiral force, related to circular dichroism (imaginary part of κ) is given as:

$$\langle \mathbf{F} \rangle_{\kappa}^{d} = \mathrm{Im}\,(c\tilde{\kappa})\frac{2}{c}\left(\Phi - \nabla \times \langle \mathbf{S} \rangle\right). \quad (60)$$

Where Φ is the chirality flow, as defined:[225]

$$\Phi = \frac{1}{2}\left\{\mathbf{E} \times (\nabla \times \mathbf{B}) - \mathbf{B} \times (\nabla \times \mathbf{E})\right\}. \quad (61)$$

Alizadeh and Reinhard[283] suggested that bi-anisotropic metamaterials could produce chiral forces and fields. Especially, they investigated the behavior of optical chirality density and optical chirality flow around double split ring resonators (DSRRs). The authors demonstrated that such metamaterials can generate highly localized and enhanced chirality flows, in addition to high gradients of optical chirality. These could serve to enlarge chiral optical forces.

A similar result from the same authors was achieved in a different configuration.[243] The authors demonstrated, both analytically and numerically, that SPPs excited by near-field sources (a circularly polarized dipole) can exhibit rich and nontrivial chiral characteristics. The data showed that excitation of SPPs by a chiral source enhanced the optical chirality not only locally but also as a net result. This configuration has been further investigated by the same authors. In reference[284] they showed that the transverse spin angular momentum of chiral surface plasmon polaritons leads to the emergence of transverse optical forces in opposite directions for chiral objects of different handedness, as schematically shown in Figure 15c. The authors found that the gradient force that arises from the intensity gradient and the scattering force that is the result of the linear momentum transfer of the photon to the particle are comparable. Thus, it could be possible, in principle, to achieve optical separation of chiral biomolecules.

Finally, as another interesting application, a new fabrication method was reported for chiral nanoparticles. This method was based on the optical forces and torque acting on plasmonic structures. In reference[285] it was demonstrated that the orbital angular momentum of light can be transferred on the shape of melted nanostructures. Upon irradiation, helical nanoneedles were produces, whose handedness depended on the helicity of the optical vortex. Although the nanoneedles were rather large in size, similar formation (though achiral) with much smaller size have been achieved with the help of local field enhancements.[286] It should therefore be very straightforward to produce correspondingly small, twisted nanoneedles.

5. Nonlinear Chiroptics

Just as nonlinear optical processes are sensitive tools in probing plasmonic nanostructures, plasmonic nanostructures are of great interest for their ability to enhance nonlinear optical processes. This relationship arises from the fact that nonlinear optical processes can be highly sensitive to symmetry and to surface/interface contributions. This is particularly true for second harmonic generation (SHG), which is forbidden in centrosymmetric materials, within the electric dipole approximation. Nanostructured materials exhibit a very high surface-to-volume ratio and their numerous surfaces/interfaces constitute that many sources for SHG. Moreover, for plasmonic nanostructures, the electromagnetic fields are enhanced precisely at these surfaces/interfaces where they can greatly enlarge the nonlinear response.[287] Additionally, in chiral plasmonic nanostructures, the chirality breaks the centrosymmetry and constitutes another source of SHG. As a consequence of all these enhancements, nonlinear chiroptical effects are more prominent than their linear optical counterparts.[288,289] Importantly, nonlinear chiroptical effects arise through different mechanisms from those in the linear regime, providing complementary information about the chirality of a system. In this section, the basic concepts of SHG in chiral media are reviewed along with nonlinear chiroptical effects, some of which have no linear counterparts.

In the linear optical regime, the induced polarization of a medium can be written as

$$\mathbf{P} = \chi^{(1)} \cdot \mathbf{E}, \quad (62)$$

where $\chi^{(1)}$ is the linear electrical susceptibility and $\mathbf{E}$ is the incident electric field. However, when the incident light is high intensity, usually provided by a laser, the induced polarization can no longer be described linearly. In the resulting nonlinear regime, the material polarization can be expressed in higher order terms as:

$$P_i(\omega) = \chi_{ij}^{(1)} E_j(\omega) + \chi_{ijk}^{(2)} E_j(\omega) E_k(\omega) + \chi_{ijkl}^{(3)} E_j(\omega) E_k(\omega) E_l(\omega) + \ldots, \quad (63)$$

where summation over repeated indices is implied. The terms $\chi_{ijk}^{(2)}$ and $\chi_{ijkl}^{(3)}$ are the second and third order nonlinear susceptibility tensors, respectively. The subscripts i, j, k, and l are such that they can each take any of the three Cartesian directions and ω is the angular frequency. The simplest nonlinear process is SHG, where a component of the material polarization occurs at twice the driving frequency ω and hence radiates at 2ω — the second harmonic. The second harmonic polarization in the electric dipole approximation is given by,[290]

$$P_i(2\omega) = \chi_{ijk}^{(2)} E_j(\omega) E_k(\omega), \quad (64)$$

where i, j, and k are again the Cartesian directions and $\chi_{ijk}^{(2)}$ is a 3rd rank tensor with 27 components each of which is complex.

In the electric dipole approximation, second order optical processes are forbidden in materials with inversion symmetry (i.e., centrosymmetric materials). A material is said to possess inversion symmetry if it is left unchanged by the operation $\mathbf{r} \rightarrow -\mathbf{r}$, where $\mathbf{r}$ is the position vector. That is to say, second order optical processes only occur in non-centrosymmetric media (the property of lacking inversion symmetry). Applying inversion symmetry to the second harmonic polarization, such that[291]

$$P_i(2\omega) = \chi_{ijk}^{(2)} E_j(\omega) E_k(\omega) \rightarrow -P_i(2\omega) = \chi_{ijk}^{(2)} (-E_j(\omega))(-E_k(\omega)), \quad (65)$$

leads to $P_i(\omega) = P_i(\omega) = 0$. Therefore, in the electric dipole approximation, SHG can only occur when inversion symmetry is broken. Accordingly, SHG has been employed as a sensitive tool in the study of surfaces and interfaces, where inversion symmetry is naturally broken. Chiral materials by definition

lack a center of inversion, meaning SHG can provide a sensitive analysis of chirality.

Quantifying all 27 complex components of a material's second order susceptibility tensor is a daunting task. However, it is possible to reduce the number of non-zero independent tensor components by using symmetry arguments, therefore making the task more tractable and rendering physical insight easier to grasp. Firstly, the choice of the experimental geometry can reduce the number of independent components. SHG experiments can be performed with two non-collinear laser beams of the same frequency, (i.e., the beams cross at the sample position). A simpler approach is to generate second harmonic from a single laser beam. If only a single beam is used, then the incident fields $E_j(\omega)$ and $E_k(\omega)$ are essentially indistinguishable and it is possible to freely interchange them. Because the fields are indistinguishable, the indices j and k in the susceptibility can be permuted and, therefore, the number of independent tensor components is reduced from 27 to 18.

According to Neumann's principle, the symmetry of a crystal can also be applied to its physical properties.[292] We can chose a Cartesian coordinate system, such that the *z*-direction points along the surface normal and the *x*- and *y*-directions lie in the plane of the sample surface. For a surface that is isotropic and achiral, the second harmonic susceptibility can be expressed as

$$\chi^{(2)}_{achiral}(2\omega) = \begin{pmatrix} 0 & 0 & 0 & 0 & \chi_{xxz} & 0 \\ 0 & 0 & 0 & \chi_{yyz} & 0 & 0 \\ \chi_{zxx} & \chi_{zyy} & \chi_{zzz} & 0 & 0 & 0 \end{pmatrix}, \tag{66}$$

where $\chi_{zxx} = \chi_{zyy}$ and $\chi_{xxz} = \chi_{yyz}$ which leaves only 3 non-zero independent components. For a surface that is isotropic and chiral, the second harmonic susceptibility becomes

$$\chi^{(2)}_{chiral}(2\omega) = \begin{pmatrix} 0 & 0 & 0 & \chi_{xyz} & \chi_{xxz} & 0 \\ 0 & 0 & 0 & \chi_{yyz} & \chi_{yxz} & 0 \\ \chi_{zxx} & \chi_{zyy} & \chi_{zzz} & 0 & 0 & 0 \end{pmatrix}, \tag{67}$$

where $\chi_{xyz} = \chi_{yxz}$ and the all other dependencies are the same as $\chi^{(2)}_{achiral}(2\omega)$.[293] As χ_{xyz} is the only new element introduced when the restriction of chirality is imposed, it is often referred to as the chiral component. It is this chiral component that is responsible for second order nonlinear chiroptical effects, such as second harmonic generation circular difference (SHG-CD) and SHG optical rotation (SHG-OR) in isotropic chiral media.

It is often convenient to work in the coordinate system of the incoming light. This coordinate system is defined by the direction of s-polarization (perpendicular to the plane of incidence), the direction of p-polarization (in the plane of incidence) and the direction of the wave vector of light. The unit vectors for the p- and s-polarization directions are related to the Cartesian system by

$$\begin{aligned} \hat{\mathbf{e}}_s &= \hat{\mathbf{y}}, \\ \hat{\mathbf{e}}_p &= \hat{\mathbf{x}}\cos(\theta) + \hat{\mathbf{z}}\sin(\theta), \end{aligned} \tag{68}$$

where θ is the angle of incidence. The electric fields can now be expressed in their p- and s-polarized components. The general expression for the second harmonic electric field can now be written as[294]

$$E(2\omega) = fE_p^2(\omega) + gE_s^2(\omega) + hE_p(\omega)E_s(\omega), \tag{69}$$

where the coefficients f, g, and h are complex and linear combinations of the tensor components of $\chi^{(2)}_{ijk}$. Fresnel factors can also be taken into account by absorbing them into the coefficients. The expressions of these coefficients depend on the symmetry of the medium, the angle of incidence and the polarization of the SHG signal. For reflected SHG from an isotropic chiral surface the expansion coefficients are given by[295]

$$\begin{aligned} f_s &= -2\sin(\theta)\cos(\theta)\chi_{xyz}, \\ g_s &= 0, \\ h_s &= 2\sin(\theta)\chi_{yyz}, \\ f_p &= \sin(\theta)(\cos^2(\theta)\chi_{zxx} + \sin^2(\theta)\chi_{zzz} - 2\cos^2(\theta)\chi_{xxz}), \\ g_p &= \sin(\theta)\chi_{zxx}, \\ h_p &= -2\sin(\theta)\cos(\theta)\chi_{xyz}. \end{aligned} \tag{70}$$

where the subscripts p and s refer to the polarization components of the SHG signal. It can be seen that f_s and h_p are equivalent and are the only coefficients to singularly depend on the chiral component. All the other coefficients are achiral. It is also possible to directly probe the chiral component of the second harmonic susceptibility. This can be done by using p-polarized light and analyzing the s-polarized SHG signal, thereby selecting only the chiral coefficient f_s that contain the chiral tensor component χ_{xyz}.[296]

Second harmonic generation circular difference (SHG-CD), which is also referred to as SHG-circular dichroism, is the normalized difference between SHG intensities upon illumination with RCP and LCP light. SHG-CD is defined as[297]

$$\text{SHG-CD} = \frac{I_{RCP}(2\omega) - I_{LCP}(2\omega)}{I_{RCP}(2\omega) + I_{LCP}(2\omega)}, \tag{71}$$

where the subscripts RCP and LCP refer to the SHG intensity, for right- and left-circularly polarized light (CPL) incident on the medium. It should be noted that this expression for SHG-CD is normalized between −1 and +1. For a circularly polarized beam the electric field components are related by $E_p(\omega) = \pm iE_s(\omega)$, where the upper and lower sign denote RCP and LCP, from the point of view of the source, looking along the direction of propagation, as the light moves away from the observer. The expression for the second harmonic intensity, when the incident beam is circularly polarized, is given by $I(2\omega) = |-f + g \pm ih|^2 I^2(\omega)$[298] which can then be used to find an expression for the SHG-CD in terms of the expansion coefficients f, g, and h, such that

$$\text{SHG-CD} = \frac{2[(f_{\text{Re}} - g_{\text{Re}})h_{\text{Im}} + (g_{\text{Im}} - f_{\text{Im}})h_{\text{Re}}]}{|f|^2 + |g|^2 + |h|^2 - 2(f_{\text{Re}}g_{\text{Re}} + f_{\text{Im}}g_{\text{Im}})}, \tag{72}$$

where the subscripts Re and Im denote the real and imaginary parts of the coefficients, respectively. It can be seen from this equation that for a circular difference effect to occur, a phase difference between the coefficients is required.

Second harmonic generation optical rotation (SHG-OR, also referred to as SHG-optical activity), is a chiroptical effect whereby linearly polarized light incident on a medium results in an SHG signal whose polarization appears rotated. It can be seen as the nonlinear chiroptical equivalent of OR. However, because it is a background free technique, SHG-OR is usually three orders of magnitude larger than linear OR.[299] SHG-OR can be expressed as[50]

$$\phi_{\text{SHG-OR}} = \tan^{-1}\left[\frac{E_s(2\omega)}{E_p(2\omega)}\right]. \tag{73}$$

For p-polarized incident light this simplifies to,

$$\phi_{\text{SHG-OR}} = \tan^{-1}\left[\frac{f_s}{f_p}\right]. \tag{74}$$

From this it can be seen that SHG-OR depends on the ratio between the chiral and achiral components. The chiral coefficient f_s changes sign between enantiomers while the achiral coefficients do not change sign. Thus, for opposite handed media the SHG-OR changes sign.

A nonlinear chiroptical effect that has no linear counterpart is SHG-linear difference (SHG-LD). Linear difference effects manifest as a change in the SHG efficiency of an isotropic chiral surface when the incident light is linearly polarized at ±45° with respect to the p-polarization direction and is defined as,[297]

$$\text{SHG-LD} = \frac{I_{+45^\circ}(2\omega) - I_{-45^\circ}(2\omega)}{I_{+45^\circ}(2\omega) + I_{-45^\circ}(2\omega)}, \tag{75}$$

where the subscripts +45° and −45° denote the SHG intensity for incident light with the respective orientation of linear polarization. The electric fields of these linear polarizations are related according to $E_p(\omega) = \pm E_s(\omega)$, where the upper and lower signs denote +45° and −45° linear polarization respectively. The SHG intensity for these polarization directions is then given as $I(2\omega) = |f + g \pm h|^2 I^2(\omega)$ which allows the SHG-LD to be expressed in terms of the expansion coefficients,

$$\text{SHG-LD} = \frac{2[(f_{Re} + g_{Re})h_{Re} + (f_{Im} + g_{Im})h_{Im}]}{|f|^2 + |g|^2 + |h|^2 + 2(f_{Re}g_{Re} + f_{Im}g_{Im})}, \tag{76}$$

where the terms are as before and the expression is normalized between −1 and +1. To the best of our knowledge there has yet to be a demonstration of SHG-LD in chiral nanostructures, although work has been done to addresses chirality with linearly polarized light.[300]

Other nonlinear optical processes can be used to study chirality or characterize metallic nanostructures such as sum frequency generation, coherent anti-Stokes Raman spectroscopy and higher harmonic generation.[301–303] Many of these nonlinear optical techniques have been developed during the study of chiral molecules.[304] However, a full description of these effects is beyond the scope of this review and have yet to be widely implemented in the study of chiral metallic nanostructures.

5.1. Nonlinear Chiroptical Materials

Due to the sensitivity of SHG to symmetry and surfaces, it was initially utilized as a tool to characterize nanostructures. For example, surface roughness and defects were studied in regards for their ability to enhance second harmonic generation (SHG),[305,306] because they break the symmetry. This was demonstrated on lithographically fabricated arrays of L-shaped nanoparticles, shown in **Figure 16**a, where the defects can be clearly seen. The symmetry breaking caused by the nanoscale defects was not detectable by linear optical measurements, however investigations using SHG revealed a strong influence on the chiroptical signatures. This highlighted the use of SHG as a powerful tool to study the fabrication quality of nanostructures.

Beyond fabrication quality control, SHG is also very powerful for investigating the chiroptical behavior of plasmonic nanostructures. Valev et al. conducted the first chiroptical investigation of such nanostructures, with SHG microscopy. The authors revealed striking patterns of emission "hotspots", see Figure 16b. The strength and distribution of these hotspots were found to depend on the handedness of the incident circularly polarized light (CPL).[307] In Figure 16b, the SEM images in (i) and (iv) present the geometry of chiral G- and mirror-G-shaped gold nanostructures, respectively. Depending on the direction of CPL (indicated with white arrows) and on the handedness, the hotspot patterns change dramatically, as can be seen in (ii), (iii), (v) and (vi). There is a clear difference depending on the direction of CPL, i.e., an SHG-CD effect is observed. Moreover, this difference reverses with the handedness of the nanostructures, exactly as expected. In a subsequent paper, the location of these SHG hotspots was pinpointed on the surface of the nanostructures and was shown to correspond to regions of enhanced local fields, at the fundamental frequency.[308] The pinpointing was achieved by inducing material deformations (or nanojets[286]) at the hotspot locations, which could subsequently be mapped with scanning probe microscopy and compared to numerical simulations.[309] Such hotspots were later reported in a variety of geometries, for instance O-shaped,[310] U-shaped,[311] and star-shaped[312] nanostructures.

Because SHG is such a highly sensitive technique, the fabrication quality of the nanostructures is crucial. A study of twisted-cross nanodimers, using SHG microscopy, found that fabrication defects could cause relatively large variations in the SHG response between individual nanodimers. However, the SHG-CD between twisted-cross nanodimers was found to be more consistent, highlighting the effectiveness of nonlinear chiroptical difference effects in probing nanostructure quality and symmetry over large arrays.[313]

The influence of fabrication defects can be diminished by the design of the material. This was shown in a study on star-shaped nanostructures.[312] Simulations of the ideal, defect free, star-shape nanostructures demonstrated that local field enhancements were located at the center of the structure and occurred below the resolution limit of SHG microscopy. In arrays of fabricated star-shape nanostructures, the defects were mainly located on the arms of the stars. Despite these defects the SHG-CD response, measured using SHG microscopy, was found to be generally homogenous over the whole array of fabricated star-shaped structures. This was explained by simulations

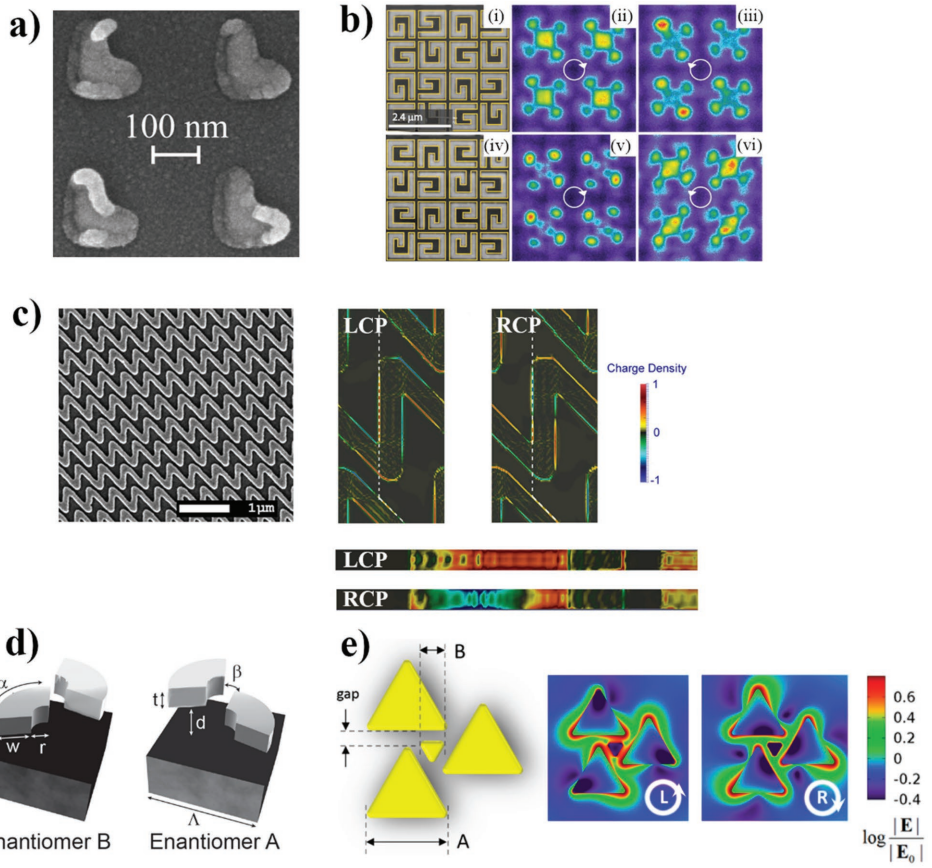

Figure 16. a) SEM image of L-shaped nanoparticles whose SHG response was strongly affected by defects. Adapted with permission.[345] Copyright 2006, Optical Society of America. b) (i) and (iv) SEM images of chiral G-shaped and mirror-G-shaped nanostructures, respectively, where the structures where highlighted with yellow lines. (ii), (iii), (v) and (vi) SHG microscopy images with rainbow color-coded intensity, demonstrating SHG-CD from the "hotspots". The direction of incident CPL is indicated with oriented circles. Reproduced with permission.[50] Copyright 2013, John Wiley and Sons. c) Scanning electron micrograph (SEM) and surface charge density simulations of the N-shape sawtooth metamaterials. (Left) SEM of the N-shaped sawtooth metamaterial. Calculated surface charge density of N-type structure under LCP and RCP illuminations. (Upper right) Simulations of the interface between the structure and the substrate. (Lower right) Simulations of the sides of the nanostructures, as indicated by the white dashed lines above. Adapted under the Creative Commons Attribution License from reference[318] d) Schematic diagrams of 3D twisted arc enantiomers. Reproduced with permission.[320] Copyright 2014, John Wiley and Sons. e) (Left) Geometry of the nanoprism meta-molecule, comprised of four elements. (Right) Calculated electric field distribution of one of the meta-molecule enantiomers under LCP (L) and RCP (R) illumination. Reproduced with permission.[321] Copyright 2015, American Chemical Society.

of the star-shaped structures with defects which demonstrated that the local field enhancements associated with the chirality of the ideal star-shape were stronger than local field enhancements due to defects. Thus, it was demonstrated that nonlinear chiral nanostructures can be carefully engineered to utilize hotspots while reducing unwanted effects from fabrication defects.

Extensions and variations of nonlinear microscopy have been developed. One such example is nonlinear optical localization using electromagnetic surface fields (NOLES) imaging.[314] Chiral bow-tie nanoantennas were investigated using the NOLES imaging technique, in conjunction with continuous-polarization (rotating a quarter-wave retarding plate to scan all polarization states) and SHG-CD measurements, to quantify magnetic dipolar contributions to the nonlinear chiroptical response.[315] Another proposed form of nonlinear microscopy extends polarization dependent measurements to also use cylindrical vector beams, where the state of polarization varies over the beam cross section. Techniques that use these vector beams vector-field nonlinear microscopy.[316] This technique should prove interesting in the study of chiral nanostructures as their optical responses depend strongly on the polarization of the incident beam.

The works discussed so far have used nonlinear microscopy to study the role of enhanced local fields in increasing nonlinear chiroptical responses. In general, local field enhancements are inhomogeneous and can alter a material's response over small areas. The inhomogeneity of the local field can complicate the process of relating measurable macroscopic responses to microscopic mechanisms. It has been shown that local field enhancements due to plasmonic resonances are not strictly necessary to produce strong SHG optical activity (SHG-OA).[317] This was demonstrated by SHG-OR measurements performed off-resonance and at oblique angles on gammadion nanostructures. Despite being off-resonance the nanostructures still displayed strong SHG-OR, comparable to that of nanostructures under resonant excitation, thus demonstrating that plasmonic

resonances are not a prerequisite for strong nonlinear chiroptical responses. The authors claimed that because the measurements were off-resonance, and therefore any local fields would be relatively homogeneous, the SHG response of the nanostructures could be analyzed within the approximation of a thin film.

Recently, SHG has been related to superchiral light. The electric quadrupole polarization at the second harmonic is given by $P_i^Q(2\omega) = \chi_{ijkl} \vdots E_j(\omega)\nabla_k E_l(\omega)$, where a dependence on the gradient of the local electric fields can be seen. Strong gradients are present at local electric field hotspots. The gradients have also been shown to contribute to the chiral dissymmetry factor g from electric dipole-electric quadrupole interactions. These interactions are proportional to $q_{ijk} = E_i\nabla_j E_k$, which is of identical form to the SHG quadrupole contribution.[244] It follows that strong dissymmetry can correspond to both superchiral light and SHG enhancements.

Higher multipole terms, beyond the electric dipole approximation, can contribute significantly to SHG responses, as demonstrated by investigations of chiral sawtooth metamaterials made from N and mirror-N shapes, shown in Figure 16c (left).[318] Continuous-polarization SHG measurements demonstrated signatures of multipolar contributions. The authors then used a nonlinear response tensor to provide a theoretical fit to the continuous-polarization experimental data. Fitting the data found that electric dipole contributions were generally weak, which was attributed to the mirror symmetry in the plane of the sample. It was suggested by the authors that the in-plane mirror symmetry causes electric dipoles on the top and bottom surfaces of the structure to partially cancel each other. This partial cancellation of the electric dipoles results in a reduced local-field enhancement and also a depleted contribution to the SHG. On the other hand, the partial cancellation of the surface electric dipoles creates an inhomogeneous field along the surface normal of the structure, which is beneficial for multipole contributions.

The authors performed simulations of the surface charge density on the N-shape structure illuminated by CPL, shown in Figure 16c (right), to examine the contribution of multipoles to the SHG. Their simulations revealed that illumination with LCP light created stronger local field enhancements compared to illumination with RCP light, which can be seen in the surface charge density simulations labelled LCP in Figure 16c (right). However, because of the symmetrical distribution of the surface charge density from incident LCP light, the emission of multipoles would be hampered. On the other hand, the weaker local fields induced by illumination with RCP light are asymmetric and inhomogeneous which is favorable for multipole sources capable of radiating along the surface normal, resulting in a stronger SHG response.

The spatial distributions of local field enhancements can also play a key role in the SHG response of a material, as demonstrated in studies on Archimedean nanospirals.[319] It was found that the intensity of SHG emission from the Archimedean nanospirals was dependent on the incident polarization and the resulting excited plasmon mode. Nanospirals incident with RCP light established a focusing mode with electrons driven to the central point. The focusing mode creates a single dominant point of SHG emission that is linearly polarized but also rotated with respect to the incident polarization. Conversely, illumination with LCP light appears to cause multiple regions of strong near-field enhancement spread over the entire nanospiral structure. The direction of SHG emission also varied between the spread-out regions of enhancement. It was suggested that the spatial distribution and varying emission direction of the numerous SHG sources caused them to destructively interfere and create a weaker and depolarized response.

Recently a few works have used chiral nanostructures with multiple elements in a unit cell to create images that can only be viewed with SHG-CD. For example, 3D twisted arc metamaterials have been used to create such SHG-CD images.[320] The 3D twisted arc consists of two arcs that are horizontally and vertically offset from one another, as shown in Figure 16d. Utilizing the strong and opposite SHG-CD of the enantiomorphs the authors created a logo which could be imaged with high contrast using SHG microscopy.

This method of creating images with enantiomorphs has also been achieved with 2D meta-molecules, comprised of nano-prisms (triangles) arranged in a chiral fashion, as shown in Figure 16e (left).[321] An image is created by using one enantiomer of the meta-molecule as a background while the opposite enantiomer creates the picture. The subwavelength nature of the individual meta-molecules renders linear imaging methods ineffective. However, because of the high SHG-CD contrast between the meta-molecule enantiomorphs, it is possible to image the picture using circularly polarized SHG microscopy. Simulations of the electric field distribution of one enantiomorph of the meta-molecule, when incident with LCP and RCP light, are shown in Figure 16e (right). The simulations demonstrate that the electric field is highly concentrated in a localized area on the left-handed enantiomer when incident with LCP light. This highly localized field enhancement is suggested to be the origin of a strong SHG response because it allows for coherent SHG emission from a single point. On the other hand, when the left-handed enantiomer is incident with RCP light, the electric field is distributed mainly on the outer edges of the structure. This results in destructive interference in the far-field and causes a weaker SHG response.

Multifunctional nonlinear chiral nanostructures have also been proposed. A chiral metamaterial consisting of two continuous metal films, each with elliptical holes angularly offset from one another, have shown promise for multifunctional applications.[322] Upon illumination with CPL, the minima in the linear transmittance spectrum of the films coincide spectrally with the maximum response in the SHG spectra. The spectral overlap between the transmittance minima and SHG maxima suggests that the increase in SHG conversion efficiency was due to conventional near-field enhancements produced by linear resonances. The continuous nature of the perforated films allows for investigations of their electro-optical properties. It was found that illuminating the films with CPL produces a net current across the structures. The polarity of the current is dependent on the handedness of both the film and the polarization of the incident light. The chiral sensitivity of the current is attributed to the photon drag effect and the authors suggest that similar continuous chiral films could find applications in simultaneously processing chiral information electrically and optically.

From previous work on chiral molecular films, it is known that the anisotropy of a medium and the chirality of the experimental setup can affect to the nonlinear chiroptical response.[323–326] In fact, measurement techniques have been demonstrated to avoid the issue and overcome "false" chiral signals by illuminating the samples at normal incident.[327,328] Yet it is clear that only a full understanding of the interplay between the various contributions to the nonlinear signal will provide full access to the chiral information of arbitrary systems. Comprehensive studies of chiral G-shaped nanomaterials have explicitly addressed the significant effects that anisotropy can have on the SHG chiroptical responses. The anisotropic coupling of plasmon modes to the incident polarization was found to explain azimuthally dependent enhancements of the SHG response of planar G-shape structures.[329] It was also found that anisotropy affected the SHG-OR of four-fold supercell G-shaped nanostructures, as the degree of polarization rotation was dependent on the azimuthal orientation of the sample.[330] Later work examined the effect of anisotropy on the SHG-CD of the supercell G-shape structures and, again, found a strong dependence on sample azimuthal rotation as well as on the angle of incidence, with the SHG-CD even changing sign.[331]

Very recently, influence of anisotropy has been studied in the case of a metamaterial composed of nanohelices with substantially sub-wavelength dimensions ($<\lambda/10$).[168] For the first time, the various rotational anisotropies that affect the SHG-CD signal were clearly identified. The authors performed continuous-polarization measurements for all azimuthal orientations of the metamaterial surface. These measurements provided a map of the anisotropy, from which the different anisotropy contributions to the SHG response were extracted and identified.

Other nonlinear processes such as two-photon luminescence (TPL) and third harmonic generation (THG) have been studied in chiral nano-systems. For example, quantum dots (QDs) have been embedded into 3D twisted arc metamaterials.[332] Embedding the QDs into the metamaterial host enhanced the TPL-CD of the local QD emitters. The observation of TPL-CD was also reported from silver nanoparticles arranged in a chiral fashion on a dielectric helical template.[159] Third harmonic generation circular difference (THG-CD) effects have recently been demonstrated in a chiral metamaterial covered with organic conjugated polymer (PFO).[333] Symmetry selection rules for the THG of nanostructures coated with PFO have been investigated with structures of various symmetries.[334] Theoretical studies of metal-insulator-metal chiral gammadion nanostructures predicted a strong THG-CD response, which could be used in the design of a Fresnel zone plate.[301]

Magneto-chiral effects (see Section 3.8) exist in the nonlinear optical regime as well. Magnetization-induced second harmonic generation[335] (MSHG) is a highly sensitive technique that can probe magnetization down to the atomic monolayer[336,337] at surfaces or even buried interfaces,[338] though care should be taken to avoid artefacts.[339] The technique can be applied to magnetic nanoparticles[340–342] and has been used to study chiral magnetic nanostructures.[343] It was found that switching the direction of magnetic field in nickel G-shaped nanostructures produced the same kind of effect as switching the handedness of gold G-shaped nanostructures.[296]

6. Concluding Remarks and Outlook

Throughout the 19th and 20th century, chirality has been mostly associated with chemistry. However, while chirality can be very useful for understanding molecules, molecules are not ideal for understanding chirality. Ideally, we would like to tune chirality while measuring the chiroptical effects in order to identify the optimal responses and determine the underlying physical processes with certainty. For instance, it would be useful to tune the geometry from one enantiomer to the other, through an achiral state, or from planar 2D chiral systems to 3D chiral systems, over several pitches. However, for complex chiral molecules, it can be extremely difficult to fabricate both enantiomers, let alone to create an achiral form of the molecules and study intermediate configurations. Within this context, chiral metal nanostructures offer an unprecedented flexibility of design. For example, with modern nanofabrication techniques, it is possible to nanostructure a metal surface with virtually any chiral pattern we can conceive of, as well as to morph one shape into another by producing numerous intermediate geometries. Thus, while molecules remain an important focus of chiral plasmonic nanomaterials, the field has achieved sufficient maturity to stand on its own.

Fabrication is an overarching challenge throughout the entire field. For instance, in the case of nanoparticle systems, the majority of work has revolved around using noble metals, such as gold and silver. There is a trend however towards investigating other materials, such as aluminum and magnesium. Such materials possess plasmon resonances that are close to the UV, where many molecules exhibit strong optical activity. An improved molecule-nanoparticle interaction can therefore be expected, yet preparing aluminum nanoparticles is notoriously difficult. In the case of planar chiral nanostructures, electron-beam lithography is widespread tool, but it is expensive and results in very small arrays. There is a need for low-cost, large-scale manufacturing and promising techniques are emerging to meet the challenge. Yet, research is already evolving towards multi-layered chiral systems that are pushing the limits of advanced nanofabrication. The challenge here is to ensure precise alignment of the successive layers. Additionally, free-standing, three-dimensional chiral networks can be observed in nature as photonic crystals that are responsible for the color on the wings of (certain) butterflies. There is a biomimetic trend towards miniaturizing such designs; gyroid networks are prominently emerging at the optical metamaterial scale. It is proving quite difficult though to realize large domains of single gyroid metamaterials. It should be noted that with increasing design complexity, understanding the behavior of the materials also becomes increasingly difficult. The 3D gyroid network is a good illustration of this complexity as, though it is certainly chiral, the handedness depends on the crystallographic directions.

Physical understanding is another overarching challenge. There is no single figure of merit that could be used to compare the behavior of all the various chiral nanostructures. Two chirality parameters though are emerging as very powerful tools: one is geometrical chirality and the other is optical chirality. While the former focusses on the chirality of the structure, the latter focusses on that of light. Geometrical chirality plays a fundamental role in negative refractive index materials. However,

the fabrication of nanostructures for use at optical frequencies remains a barrier to possible applications, together with optical loss. Nevertheless, important progress is being made through numerical simulations. For its part, the research into optical chirality has benefited a lot from the strong keyword "superchiral light". Several exciting systems and mechanisms have been proposed to enhance the chiroptical responses of molecules using superchiral light. However, the term itself is still subject to lively discussion in the research community.

Within this context, helical nanomaterials constitute a convenient test bed for both geometrical and optical chirality parameters. Crucially, there have been some remarkable recent advancements in the fabrication procedures for single nanohelices, rotationally symmetric multiple helices and substantially sub-wavelength nanohelices. We anticipate that this archetypical chiral geometry will be key for the future development of the field, both in the linear and the nonlinear optical regime.

Nonlinear chiroptical materials are emerging as an important direction of research. A chief challenge is to understand the local physical mechanisms that are responsible for strong nonlinear chiral hotspots, in order to enable meaningful nonlinear light-molecule interactions. Equally important is the need for a rigorous theory of nonlinear optics, for chiral metamaterials that would enable us to benefit from higher order multipolar contributions. Overall, compared to linear optics, nonlinear optics of chiral systems is in its infancy. For instance, there is no clear link between the geometrical parameters of chiral materials and the nonlinear susceptibility tensors. And while a connection has been established between the quadrupolar contributions to optical chirality and the quadrupolar contributions to SHG, the specific ways to benefit from the connection are unclear. The interplay between chirality and anisotropy is also not as well understood in nonlinear optics as it is in the linear case.

For linear and nonlinear systems, extrinsic chirality can complicate the intrinsically chiroptical response. This is especially true for the more complex, 3D geometries. Disentangling the two is a challenge, yet, when well separated, these effects could lead to applications where the intrinsic chirality is enhanced or reduced by varying the experimental geometry. An intriguing application would be to construct easily tunable chiroptical devices.

By contrast, any applications of magnetochiral effects seem far in the future. These effects have been elusive for over a hundred years and the research into related materials is just beginning. An interesting avenue in this direction is to explore the relationship to toroidal chirality, however it should be pointed out that the magnetochiral effects reported so far are very weak.

Weak signals are also a chief obstacle for realizing the potential of surface enhanced Raman optical activity. Due to the low signal-to-noise ratio, artefacts constitute a major nuisance. Nevertheless, just as Raman scattering has benefited tremendously from surface enhancements, we believe that Raman optical activity stands to greatly benefit from plasmonic nanoparticles.

In this review, we also sought to attract attention to another area that is still underdeveloped but is growing rapidly, namely the use of chiral optical forces. So far, there have been several theoretical investigations of the topic but few experimental realizations. Yet the theory is very attractive and we believe that this area will grow. Potential applications can be envisioned in chiral separation, where selective optical forces could distinguish between chiral molecules/nanoparticles and sort them by handedness.

In recent years, DNA origami has become a fascinating tool for exploring the chiroptical effects in plasmonic nanostructures. DNA offers remarkable precision for the 3D assembly of nanoparticles. The fact that the molecule is itself chiral is both a blessing and a curse. On the one hand, it is highly convenient to study this particular molecule's chiroptical enhancements due to plasmonics. On the other hand, it complicates the study of additional chiral molecules or of the chiral nanoparticle assembly itself. Whatever our predictions though, surprising new directions of research are bound to emerge from this captivating playset, such as, for instance, the monitoring of the actuation of nanorobots.

To conclude, we have seen that the field of chiral plasmonic nanoparticles is emerging as an exciting area of scientific research rich in possibilities.

Acknowledgements

V.K.V. acknowledges support from the Royal Society through the University Research Fellowships. J.T.C. acknowledges funding from the Royal Society. D.C.H. acknowledges funding from the EPSRC Centre for Doctoral Training Grant No. EP/L015544/1, EPSRC Centre for Doctoral Training in Condensed Matter Physics (CDT-CMP). J.T.C. and C.K. contributed equally to this work.

Conflict of Interest

The authors declare no conflict of interest.

Keywords

chirality, metamaterials, nanophotonics, plasmonics, superchiral light

Received: February 24, 2017
Revised: June 28, 2017
Published online: August 1, 2017

[1] W. T. B. Kelvin, *Baltimore Lectures on Molecular Dynamics and the Wave Theory of Light*, C.J. Clay And Sons, London, UK, **1904**.
[2] V. Saranathan, C. O. Osuji, S. G. J. Mochrie, H. Noh, S. Narayanan, A. Sandy, E. R. Dufresne, R. O. Prum, *Proc. Natl. Acad. Sci.* **2010**, *107*, 11676.
[3] V. Sharma, M. Crne, J. O. Park, M. Srinivasarao, *Science* **2009**, *325*, 449.
[4] S. Vignolini, E. Moyroud, B. J. Glover, U. Steiner, *J. R. Soc. Interface* **2013**, *10*, 20130394.
[5] I. Čorić, B. List, *Nature* **2012**, *483*, 315.
[6] D. L. Lewis, A. W. Garrison, K. E. Wommack, A. Whittemore, P. Steudler, J. Melillo, *Nature* **1999**, *401*, 898.
[7] M. E. Franks, G. R. Macpherson, W. D. Figg, *Lancet* **2004**, *363*, 1802.
[8] F. Kamarei, P. Vajda, F. Gritti, G. Guiochon, *J. Chromatogr. A* **2014**, *1345*, 200.
[9] D. J. Cordato, L. E. Mather, G. K. Herkes, *J. Clin. Neurosci.* **2003**, *10*, 649.

[10] Sekhon, *J. Mod. Med. Chem.* **2013**, *1*, 10.
[11] L. Keszthelyi, *Q. Rev. Biophys.* **2017**, *4*, 473.
[12] J. Bailey, *Science* **1998**, *281*, 672.
[13] S. Pizzarello, *Acc. Chem. Res.* **2006**, *39*, 231.
[14] K. Soai, T. Shibata, H. Morioka, K. Choji, *Nature* **1995**, *378*, 767.
[15] M. Klussmann, H. Iwamura, S. P. Mathew, D. H. Wells, U. Pandya, A. Armstrong, D. G. Blackmond, *Nature* **2006**, *441*, 621.
[16] L. Pasteur, *Ann. Chim. Phys.* **1848**, *24*, 442.
[17] J.-B. Biot, *Ann. Chim. Phys.* **1850**, *28*, 99.
[18] E. Hendry, T. Carpy, J. Johnston, M. Popland, R. V. Mikhaylovskiy, A. J. Lapthorn, S. M. Kelly, L. D. Barron, N. Gadegaard, M. Kadodwala, *Nat. Nanotechnol.* **2010**, *5*, 783.
[19] R. Tullius, A. S. S. Karimullah, M. Rodier, B. Fitzpatrick, N. Gadegaard, L. D. D. Barron, V. M. M. Rotello, G. Cooke, A. Lapthorn, M. Kadodwala, *J. Am. Chem. Soc.* **2015**, *137*, 8380.
[20] M. J. J. Urban, C. Zhou, X. Duan, N. Liu, *Nano Lett.* **2015**, *15*, 8392.
[21] D. Schamel, M. Pfeifer, J. G. Gibbs, B. Miksch, A. G. Mark, P. Fischer, *J. Am. Chem. Soc.* **2013**, *135*, 12353.
[22] M. Khorasaninejad, W. T. Chen, A. Y. Zhu, J. Oh, R. C. Devlin, D. Rousso, F. Capasso, *Nano Lett.* **2016**, *16*, 4595.
[23] J. K. Gansel, M. Wegener, S. Burger, S. Linden, *Opt. Express* **2010**, *18*, 1059.
[24] W. Li, Z. J. Coppens, L. V. Besteiro, W. Wang, A. O. Govorov, J. Valentine, *Nat. Commun.* **2015**, *6*, 8379.
[25] R. Farshchi, M. Ramsteiner, J. Herfort, A. Tahraoui, H. T. Grahn, *Appl. Phys. Lett.* **2011**, *98*, 162508.
[26] C. Wagenknecht, C. Li, A. Reingruber, X. Bao, A. Goebel, Y.-A. Chen, Q. Zhang, K. Chen, J. Pan, *Nat. Photonics* **2010**, *4*, 549.
[27] J. F. Sherson, H. Krauter, R. K. Olsson, B. Julsgaard, K. Hammerer, I. Cirac, E. S. Polzik, *Nature* **2006**, *443*, 557.
[28] A. Guerrero-Martínez, J. L. Alonso-Gómez, B. Auguié, M. M. Cid, L. M. Liz-Marzán, *Nano Today* **2011**, *6*, 381.
[29] A. O. Govorov, Y. K. Gun'ko, J. M. Slocik, V. a. Gérard, Z. Fan, R. R. Naik, *J. Mater. Chem.* **2011**, *21*, 16806.
[30] A. Ben-Moshe, B. M. Maoz, A. O. Govorov, G. Markovich, *Chem. Soc. Rev.* **2013**, *42*, 7028.
[31] Y. Wang, J. Xu, Y. Wang, H. Chen, *Chem. Soc. Rev.* **2013**, *42*, 2930.
[32] W. Jing, L. Shuang, Z. Chun, X. Huibi, Y. Xiangliang, *Prog. Chem.* **2011**, *23*, 669.
[33] H. Liu, X. Shen, Z.-G. Wang, A. Kuzyk, B. Ding, *Nanoscale* **2014**, *6*, 9331.
[34] L. Wu, W. Zhang, D. Zhang, *Small* **2015**, *11*, 5004.
[35] J. Kumar, K. G. Thomas, L. M. Liz-Marzán, *Chem. Commun.* **2016**, *52*, 12555.
[36] J. Kaschke, M. Wegener, *Nanophotonics* **2016**, *5*, 510.
[37] Z. Wang, F. Cheng, T. Winsor, Y. Liu, *Nanotechnology* **2016**, *27*, 412001.
[38] J. Govan, Y. K. Gun'ko, in *Nanoscience*, Vol. *3*, The Royal Society of Chemistry, London, UK, **2016**, pp. 1–30.
[39] F. P. Milton, J. Govan, M. V. Mukhina, Y. K. Gun'ko, *Nanoscale Horiz.* **2016**, *1*, 14.
[40] N. Papasimakis, V. A. A. Fedotov, V. Savinov, T. A. A. Raybould, N. I. I. Zheludev, *Nat. Mater.* **2016**, *15*, 263.
[41] N. Papasimakis, V. A. Fedotov, K. Marinov, N. I. Zheludev, *Phys. Rev. Lett.* **2009**, *103*, 93901.
[42] A. Ghosh, P. Fischer, *Nano Lett.* **2009**, *9*, 2243.
[43] A. G. G. Mark, J. G. G. Gibbs, T.-C. Lee, P. Fischer, *Nat. Mater.* **2013**, *12*, 802.
[44] D. Schamel, A. G. Mark, J. G. Gibbs, C. Miksch, K. I. Morozov, A. M. Leshansky, P. Fischer, *ACS Nano* **2014**, *8*, 8794.
[45] J. G. Gibbs, P. Fischer, *Chem. Commun.* **2015**, *51*, 4192.
[46] M. P. Moloney, Y. K. Gun'ko, J. M. Kelly, *Chem. Commun.* **2007**, *7345*, 3900.
[47] S. D. Elliott, M. P. Moloney, Y. K. Gun'ko, *Nano Lett.* **2008**, *8*, 2452.
[48] J. E. Govan, E. Jan, A. Querejeta, N. A. Kotov, Y. K. Gun'ko, *Chem. Commun.* **2010**, *46*, 6072.
[49] A. L. Nafie, *Applications of Vibrational Optical Activity*, Wiley, Chichester, UK, **2011**.
[50] V. K. Valev, J. J. Baumberg, C. Sibilia, T. Verbiest, *Adv. Mater.* **2013**, *25*, 2517.
[51] S. Zhang, H. Wei, K. Bao, U. Håkanson, N. J. Halas, P. Nordlander, H. Xu, *Phys. Rev. Lett.* **2011**, *107*, 1.
[52] A. O. Govorov, Z. Fan, P. Hernandez, J. M. Slocik, R. R. Naik, *Nano Lett.* **2010**, *10*, 1374.
[53] J. M. Slocik, A. O. Govorov, R. R. Naik, *Nano Lett.* **2011**, *11*, 701.
[54] P. J. Stephens, *Wiley Interdiscip. Rev. Comput. Mol. Sci.* **1985**, *1*, 748.
[55] T. B. Freedman, X. Cao, R. K. Dukor, L. a Nafie, *Chirality* **2003**, *15*, 743.
[56] H. Takechi, O. Arteaga, J. M. Ribo, H. Watarai, *Molecules* **2011**, *16*, 3636.
[57] C. Helgert, E. Pshenay-Severin, M. Falkner, C. Menzel, C. Rockstuhl, E. B. Kley, A. Tünnermann, F. Lederer, T. Pertsch, *Nano Lett.* **2011**, *11*, 4400.
[58] M. Esposito, V. Tasco, F. Todisco, A. Benedetti, I. Tarantini, M. Cuscunà, L. Dominici, M. De Giorgi, A. Passaseo, *Nanoscale* **2015**, *7*, 18081.
[59] M. Decker, R. Zhao, C. M. M. Soukoulis, S. Linden, M. Wegener, *Opt. Lett.* **2010**, *35*, 1593.
[60] T. Narushima, S. Hashiyada, H. Okamoto, *ACS Photonics* **2014**, *1*, 732.
[61] K. Chaudhari, T. Pradeep, *Appl. Phys. Lett.* **2014**, *105*, 203105.
[62] L. Silvestroni, *Electronic and Magnetic Properties of Chiral Molecules and Supramolecular Architectures*, Springer Berlin Heidelberg, Berlin, Heidelberg, Germany, **2011**.
[63] S. A. Maier, *Plasmonics: Fundamentals and Applications*, Springer US, Boston, MA, **2007**.
[64] J. M. Luther, P. K. Jain, T. Ewers, A. P. Alivisatos, *Nat. Mater.* **2011**, *10*, 361.
[65] H. Jeong, A. G. Mark, M. Alarcón-Correa, I. Kim, P. Oswald, T.-C. Lee, P. Fischer, *Nat. Commun.* **2016**, *7*, 11331.
[66] B. Shanker, A. Lakhtakia, *J. Phys. D. Appl. Phys.* **1993**, *26*, 1746.
[67] M. Vrancken, G. A. E. Vandenbosch, *IEEE Trans. Microw. Theory Tech.* **2003**, *51*, 216.
[68] Y. Schols, G. A. E. Vandenbosch, *IEEE Trans. Antennas Propag.* **2007**, *55*, 1086.
[69] "Lumerical Solutions, inc," can be found under http://www.lumerical.com/, **n.d.**
[70] A. F. Oskooi, D. Roundy, M. Ibanescu, P. Bermel, J. D. Joannopoulos, S. G. Johnson, *Comput. Phys. Commun.* **2010**, *181*, 687.
[71] Diffract MOD, RSoft Design Group, http://www.rsoftdesign.com (accessed: July 2017).
[72] K. W. Smith, H. Zhao, H. Zhang, A. Sánchez-Iglesias, M. Grzelczak, Y. Wang, W.-S. Chang, P. Nordlander, L. M. Liz-Marzán, S. Link, *ACS Nano* **2016**, *10*, 6180.
[73] F. Bai, J. Deng, M. Yang, J. Fu, J. Ng, Z. Huang, *Nanotechnology* **2016**, *27*, 115703.
[74] A. Painelli, F. Terenziani, L. Angiolini, T. Benelli, L. Giorgini, *Chem. Eur. J.* **2005**, *11*, 6053.
[75] N. Nishida, Y. Kojima, H. Tanaka, *Chem. Lett.* **2014**, *43*, 1227.
[76] W. Kuhn, *Trans. Faraday Soc.* **1930**, *26*, 293.
[77] N. Berova, L. Di Bari, G. Pescitelli, *Chem. Soc. Rev.* **2007**, *36*, 914.
[78] A. Guerrero-Martínez, B. Auguié, J. L. Alonso-Gómez, Z. Džolić, S. Gómez-Graña, M. Žinić, M. M. Cid, L. M. Liz-Marzán, *Angew. Chemie - Int. Ed.* **2011**, *50*, 5499.
[79] Z. Fan, A. O. Govorov, *Nano Lett.* **2010**, *10*, 2580.
[80] B. Auguié, J. L. Alonso-Gómez, A. Guerrero-Martínez, L. M. Liz-Marzán, *J. Phys. Chem. Lett.* **2011**, *2*, 846.

[81] S. Efrima, *Chem. Phys. Lett.* **1983**, *102*, 79.
[82] S. Efrima, *J. Chem. Phys.* **1985**, *83*, 1356.
[83] H. Kneipp, J. Kneipp, K. Kneipp, *Anal. Chem.* **2006**, *78*, 2853.
[84] S. O. Pour, S. E. J. Bell, E. W. Blanch, *Chem. Commun.* **2011**, *47*, 4754.
[85] M. Sun, Z. Zhang, P. Wang, Q. Li, F. Ma, H. Xu, *Light Sci. Appl.* **2013**, *2*, e112.
[86] J. Xia, Y. Feng, L. Zhu, Z. Zhang, L. Xia, L. Liu, *Plasmonics* **2014**, *9*, 673.
[87] J. Koktan, H. Sedláčková, I. Osante, C. Cativiela, D. Díaz Díaz, P. Řezanka, *Colloids Surf. A, Physicochem. Eng. Asp.* **2015**, *470*, 142.
[88] S. O. Pour, L. Rocks, K. Faulds, D. Graham, V. Parchansky, P. Bour, E. W. Blanch, *Nat Chem* **2015**, *7*, 591.
[89] B. M. Maoz, R. van der Weegen, Z. Fan, A. O. Govorov, G. Ellestad, N. Berova, E. W. Meijer, G. Markovich, *J. Am. Chem. Soc.* **2012**, *134*, 17807.
[90] A. O. Govorov, Z. Fan, *ChemPhysChem* **2012**, *13*, 2551.
[91] H. S. Oh, S. Liu, H. Jee, A. Baev, M. T. Swihart, P. N. Prasad, *J. Am. Chem. Soc.* **2010**, *132*, 17346.
[92] Z. Fan, A. O. Govorov, *Nano Lett.* **2012**, *12*, 3283.
[93] L. Y. Y. Wang, K. W. W. Smith, S. Dominguez-Medina, N. Moody, J. M. M. Olson, H. Zhang, W. S. S. Chang, N. Kotov, S. Link, *ACS Photonics* **2015**, *2*, 1602.
[94] A. O. Govorov, *J. Phys. Chem. C* **2011**, *115*, 7914.
[95] X. Yin, M. Schäferling, B. Metzger, H. Giessen, *Nano Lett.* **2013**, *13*, 6238.
[96] H. Wang, Z. Li, H. Zhang, P. Wang, S. Wen, *Sci. Rep.* **2015**, *5*, 8207.
[97] L. Chuntonov, G. Haran, *Nano Lett.* **2011**, *11*, 2440.
[98] M. Liu, D. a Powell, I. V. Shadrivov, M. Lapine, Y. S. Kivshar, *Nat. Commun.* **2014**, *5*, 4441.
[99] S. Toroghi, C. Lumdee, P. G. Kik, in *Proc. SPIE* (Ed.: M. I. Stockman), **2013**, p. 88091M.
[100] R. Ogier, Y. Fang, M. Svedendahl, P. Johansson, M. Käll, *ACS Photonics* **2014**, *1*, 1074.
[101] M. Hentschel, M. Schäferling, T. Weiss, N. Liu, H. Giessen, *Nano Lett.* **2012**, *12*, 2542.
[102] M. E. Layani, A. Ben Moshe, M. Varenik, O. Regev, H. Zhang, A. O. Govorov, G. Markovich, *J. Phys. Chem. C* **2013**, *117*, 22240.
[103] M. C. di Gregorio, A. Ben Moshe, E. Tirosh, L. Galantini, G. Markovich, *J. Phys. Chem. C* **2015**, *119*, 17111.
[104] M. Kuwata-Gonokami, N. Saito, Y. Ino, M. Kauranen, K. Jefimovs, T. Vallius, J. Turunen, Y. Svirko, *Phys. Rev. Lett.* **2005**, *95*, 1.
[105] B. Bai, Y. Svirko, J. Turunen, T. Vallius, *Phys. Rev. A* **2007**, *76*, 23811.
[106] O. Arteaga, J. Sancho-Parramon, S. Nichols, B. M. Maoz, A. Canillas, S. Bosch, G. Markovich, B. Kahr, *Opt. Express* **2016**, *24*, 2242.
[107] S. Wu, Z. Zhang, Y. Zhang, K. Zhang, L. Zhou, X. Zhang, Y. Zhu, *Phys. Rev. Lett.* **2013**, *110*, 1.
[108] S. Zu, Y. Bao, Z. Fang, *Nanoscale* **2016**, *8*, 3900.
[109] B. Hopkins, A. N. Poddubny, A. E. Miroshnichenko, Y. S. Kivshar, *Laser Photon. Rev.* **2016**, *10*, 137.
[110] H. Okamoto, T. Narushima, Y. Nishiyama, K. Imura, *Phys. Chem. Chem. Phys.* **2015**, *17*, 6192.
[111] T. Narushima, S. Hashiyada, H. Okamoto, *Chirality* **2016**, *28*, 540.
[112] T. Narushima, H. Okamoto, *Phys. Chem. Chem. Phys.* **2013**, *15*, 13805.
[113] T. Narushima, H. Okamoto, *J. Phys. Chem. C* **2013**, *117*, 23964.
[114] S. Hashiyada, T. Narushima, H. Okamoto, *J. Phys. Chem. C* **2014**, *118*, 22229.
[115] F. Alali, Y. H. Kim, A. Baev, E. P. Furlani, *ACS Photonics* **2014**, *1*, 507.
[116] M. Decker, M. Ruther, C. E. E. Kriegler, J. Zhou, C. M. M. Soukoulis, S. Linden, M. Wegener, *Opt. Lett.* **2009**, *34*, 2501.
[117] N. Liu, H. Liu, S. Zhu, H. Giessen, *Nat. Photonics* **2009**, *3*, 157.
[118] X. Xiong, W.-H. Sun, Y.-J. Bao, M. Wang, R.-W. Peng, C. Sun, X. Lu, J. Shao, Z.-F. Li, N.-B. Ming, *Phys. Rev. B* **2010**, *81*, 75119.
[119] Z. Li, R. Zhao, T. Koschny, M. Kafesaki, K. B. Alici, E. Colak, H. Caglayan, E. Ozbay, C. M. Soukoulis, *Appl. Phys. Lett.* **2010**, *97*, 81901.
[120] M. Hentschel, T. Weiss, S. Bagheri, H. Giessen, *Nano Lett.* **2013**, *13*, 4428.
[121] C. Jack, A. S. Karimullah, R. Leyman, R. Tullius, V. M. Rotello, G. Cooke, N. Gadegaard, L. D. Barron, M. Kadodwala, *Nano Lett.* **2016**, *16*, 5806.
[122] A. S. Karimullah, C. Jack, R. Tullius, V. M. Rotello, G. Cooke, N. Gadegaard, L. D. Barron, M. Kadodwala, *Adv. Mater.* **2015**, *27*, 5610.
[123] K. Hannam, D. A. Powell, I. V. Shadrivov, Y. S. Kivshar, *Phys. Rev. B* **2014**, *89*, 125105.
[124] Z. Wu, Y. Zheng, *Adv. Opt. Mater.* **2017**, *5*, 1700034.
[125] Y. Zhao, M. a. Belkin, A. Alù, *Nat. Commun.* **2012**, *3*, 870.
[126] Y. Zhu, X. Hu, Z. Chai, H. Yang, Q. Gong, *Appl. Phys. Lett.* **2015**, *106*, 91109.
[127] Y. Cui, L. Kang, S. Lan, S. Rodrigues, W. Cai, *Nano Lett.* **2014**, *14*, 1021.
[128] M. M. Hossain, M. Gu, *Laser Photon. Rev.* **2014**, *8*, 233.
[129] S. Vignolini, N. A. Yufa, P. S. Cunha, S. Guldin, I. Rushkin, M. Stefik, K. Hur, U. Wiesner, J. J. Baumberg, U. Steiner, *Adv. Mater.* **2012**, *24*, OP23.
[130] A. Radke, T. Gissibl, T. Klotzbücher, P. V. Braun, H. Giessen, *Adv. Mater.* **2011**, *23*, 3018.
[131] G. Kenanakis, A. Xomalis, A. Selimis, M. Vamvakaki, M. Farsari, M. Kafesaki, C. M. Soukoulis, E. N. Economou, *ACS Photonics* **2015**, *2*, 287.
[132] L. A. Ibbotson, A. Demetriadou, S. Croxall, O. Hess, J. J. Baumberg, *Sci. Rep.* **2015**, *5*, 8313.
[133] J. D. Kraust, *Proc. I.R.E.* **1949**, *37*, 263.
[134] M. Esposito, V. Tasco, F. Todisco, M. Cuscunà, A. Benedetti, D. Sanvitto, A. Passaseo, *Nat. Commun.* **2015**, *6*, 6484.
[135] I. Tinoco, M. P. Freeman, *J. Phys. Chem.* **1957**, *61*, 1196.
[136] W. Kauzmann, *Quantum Chemistry: An Introduction*, Academic Press, San Diego, CA, **1957**.
[137] I. Tinoco Jr., R. W. Woody, *J. Chem. Phys.* **1964**, *40*, 160.
[138] D. Moore, I. Tinoco, *J. Chem. Phys.* **1980**, *72*, 3396.
[139] E. U. Condon, W. Altar, H. Eyring, *J. Chem. Phys.* **1937**, *5*, 753.
[140] Z.-Y. Zhang, Y.-P. Zhao, *Appl. Phys. Lett.* **2007**, *90*, 221501.
[141] Z.-Y. Zhang, Y.-P. Zhao, *Appl. Phys. Lett.* **2011**, *98*, 83102.
[142] Y. Li, R. Ho, Y. Hung, *IEEE Photonics J.* **2013**, *5*, 2700510.
[143] F. Ge, J. Zhu, L. Chen, *Int. J. Infrared Millimeter Waves* **1996**, *17*, 449.
[144] J. J. Maki, A. Persoons, *J. Chem. Phys.* **1996**, *104*, 9340.
[145] F. Hache, H. Mesnil, M. C. Schanne-Klein, *J. Chem. Phys.* **2001**, *115*, 6707.
[146] J. K. Gansel, J. K. Gansel, M. Thiel, M. S. Rill, M. Decker, K. Bade, V. Saile, G. Von Freymann, S. Linden, M. Wegener, *Science* **2011**, *1513*, 1513.
[147] Z. Fan, A. O. Govorov, *J. Phys. Chem. C* **2011**, *115*, 13254.
[148] Z. Zhao, D. Gao, C. Bao, X. Zhou, T. Lu, L. Chen, *J. Light. Technol.* **2012**, *30*, 2442.
[149] J. K. Gansel, M. Latzel, A. Frölich, J. Kaschke, M. Thiel, M. Wegener, *Appl. Phys. Lett.* **2012**, *100*, 2014.
[150] J. George, K. G. Thomas, *J. Am. Chem. Soc.* **2010**, *132*, 2502.
[151] J. H. Singh, G. Nair, A. Ghosh, A. Ghosh, *Nanoscale* **2013**, *5*, 7224.
[152] G. Nair, H. J. Singh, D. Paria, M. Venkatapathi, A. Ghosh, *J. Phys. Chem. C* **2014**, *118*, 4991.
[153] G. Nair, H. J. Singh, A. Ghosh, *J. Mater. Chem. C* **2015**, *3*, 6831.
[154] Z. Y. Yang, M. Zhao, P. X. Lu, Y. F. Lu, *Opt. Lett.* **2010**, *35*, 2588.
[155] C. Song, M. G. Blaber, G. Zhao, P. Zhang, H. C. Fry, G. C. Schatz, N. L. Rosi, *Nano Lett.* **2013**, *13*, 3256.

[156] M. Esposito, V. Tasco, F. Todisco, M. Cuscunà, A. Benedetti, M. Scuderi, G. Nicotra, A. Passaseo, *Nano Lett.* **2016**, *16*, 5823.
[157] J. Kaschke, J. K. Gansel, M. Wegener, *Opt. Express* **2012**, *20*, 26012.
[158] M. Schäferling, X. Yin, N. Engheta, H. Giessen, *ACS Photonics* **2014**, *1*, 530.
[159] H. J. Singh, Saumitra, V. R. Singh, S. K. Sikdar, B. Jayaprakash, A. Ghosh, *ACS Photonics* **2016**, *3*, 863.
[160] M. Esposito, V. Tasco, M. Cuscunà, F. Todisco, A. Benedetti, I. Tarantini, M. De Giorgi, D. Sanvitto, A. Passaseo, *ACS Photonics* **2015**, *2*, 105.
[161] M. Esposito, V. Tasco, F. Todisco, A. Benedetti, D. Sanvitto, A. Passaseo, *Adv. Opt. Mater.* **2014**, *2*, 154.
[162] Y. He, G. K. Larsen, W. Ingram, Y. Zhao, *Nano Lett.* **2014**, *14*, 1976.
[163] G. K. Larsen, Y. Zhao, *Appl. Phys. Lett.* **2014**, *105*, 71109.
[164] G. K. Larsen, Y. He, W. Ingram, E. T. LaPaquette, J. Wang, Y. Zhao, *Nanoscale* **2014**, *6*, 9467.
[165] J. Titus, G. Larsen, Y. Zhao, A. G. U. Perera, *Ann. Phys.* **2016**, *528*, 677.
[166] J. G. Gibbs, A. G. Mark, S. Eslami, P. Fischer, *Appl. Phys. Lett.* **2013**, *103*, 213101.
[167] J. G. Gibbs, A. G. Mark, T.-C. Lee, S. Eslami, D. Schamel, P. Fischer, *Nanoscale* **2014**, *6*, 9457.
[168] D. C. Hooper, A. G. Mark, C. Kuppe, J. T. Collins, P. Fischer, V. K. Valev, *Adv. Mater.* **2017**, *29*, 1605110.
[169] H. Jeong, A. G. Mark, T. Lee, M. Alarcón-Correa, S. Eslami, T. Qiu, J. G. Gibbs, P. Fischer, *Nano Lett.* **2016**, *16*, 4887.
[170] H. Jeong, A. G. Mark, P. Fischer, *Chem. Commun.* **2016**, *52*, 12179.
[171] J. Kaschke, L. Blume, L. Wu, M. Thiel, K. Bade, Z. Yang, M. Wegener, *Adv. Opt. Mater.* **2015**, *3*, 1411.
[172] J. Deng, J. Fu, J. Ng, Z. Huang, *Nanoscale* **2016**, *8*, 4504.
[173] H.-Z. Yao, S. Zhong, *IEEE Photonics J.* **2015**, *7*, 1.
[174] H.-Z. Yao, S. Zhong, *Opt. Commun.* **2015**, *354*, 1.
[175] A. P. Slobozhanyuk, M. Lapine, D. A. Powell, I. V. Shadrivov, Y. S. Kivshar, R. C. McPhedran, P. A. Belov, *Adv. Mater.* **2013**, *25*, 3409.
[176] L. Wang, K. G. Gutierrez-Cuevas, A. Urbas, Q. Li, *Adv. Opt. Mater.* **2016**, *4*, 247.
[177] G. Shemer, O. Krichevski, G. Markovich, T. Molotsky, I. Lubitz, A. B. Kotlyar, *J. Am. Chem. Soc.* **2006**, *128*, 11006.
[178] P. W. K. Rothemund, *Nature* **2006**, *440*, 297.
[179] J. Sharma, R. Chhabra, A. Cheng, J. Brownell, Y. Liu, H. Yan, *Science* **2009**, *323*, 112.
[180] A. J. Mastroianni, S. Claridge, A. P. Alivisatos, *J. Am. Chem. Soc.* **2010**, *131*, 8455.
[181] X. Shen, A. Asenjo-Garcia, Q. Liu, Q. Jiang, F. J. G. de Abajo, N. Liu, B. Ding, *Nano Lett.* **2013**, *13*, 2128.
[182] X. Shen, C. Song, J. Wang, D. Shi, Z. Wang, N. Liu, B. Ding, *J. Am. Chem. Soc.* **2012**, *134*, 146.
[183] A. Cecconello, J. S. Kahn, C.-H. Lu, L. K. Khorashad, A. O. Govorov, I. Willner, *J. Am. Chem. Soc.* **2016**, *138*, 9895.
[184] A. Kuzyk, R. Schreiber, Z. Fan, G. Pardatscher, E.-M. Roller, A. Högele, F. C. Simmel, A. O. Govorov, T. Liedl, *Nature* **2012**, *483*, 311.
[185] R. Schreiber, N. Luong, Z. Fan, A. Kuzyk, P. C. Nickels, T. Zhang, D. M. Smith, B. Yurke, W. Kuang, A. O. Govorov, T. Liedl, *Nat. Commun.* **2013**, *4*, 2948.
[186] A. Kuzyk, R. Schreiber, H. Zhang, A. O. Govorov, T. Liedl, N. Liu, *Nat. Mater.* **2014**, *13*, 862.
[187] Z. Li, Z. Zhu, W. Liu, Y. Zhou, B. Han, Y. Gao, Z. Tang, *J. Am. Chem. Soc.* **2012**, *134*, 3322.
[188] X. Lan, Z. Chen, G. Dai, X. Lu, W. Ni, Q. Wang, *J. Am. Chem. Soc.* **2013**, *135*, 11441.
[189] X. Shen, P. Zhan, A. Kuzyk, Q. Liu, A. Asenjo-Garcia, H. Zhang, F. J. G. de Abajo, A. Govorov, B. Ding, N. Liu, *Nanoscale* **2014**, *6*, 2077.
[190] W. Ma, H. Kuang, L. Xu, L. Ding, C. Xu, L. Wang, N. A. Kotov, *Nat. Commun.* **2013**, *4*, 2689.
[191] X. Wu, L. Xu, W. Ma, L. Liu, H. Kuang, W. Yan, L. Wang, C. Xu, *Adv. Funct. Mater.* **2015**, *25*, 850.
[192] E. Plum, X.-X. Liu, V. A. Fedotov, Y. Chen, D. P. Tsai, N. I. Zheludev, *Phys. Rev. Lett.* **2009**, *102*, 113902.
[193] B. M. Maoz, A. Ben Moshe, D. Vestler, O. Bar-Elli, G. Markovich, *Nano Lett.* **2012**, *12*, 2357.
[194] E. Plum, V. A. A. Fedotov, N. I. I. Zheludev, *J. Opt.* **2011**, *13*, 24006.
[195] T. Cao, C. Wei, L. Mao, Y. Li, *Sci. Rep.* **2014**, *4*, 7442.
[196] L. Hu, Y. Huang, L. Fang, G. Chen, H. Wei, Y. Fang, *Sci. Rep.* **2015**, *5*, 16069.
[197] L. Hu, X. Tian, Y. Huang, L. Fang, Y. Fang, *Nanoscale* **2016**, *8*, 3720.
[198] A. Belardini, M. Centini, G. Leahu, D. C. Hooper, R. Li Voti, E. Fazio, J. W. Haus, A. Sarangan, V. K. Valev, C. Sibilia, *Sci. Rep.* **2016**, *6*, 31796.
[199] A. Belardini, M. Centini, G. Leahu, E. Fazio, C. Sibilia, J. W. W. Haus, A. Sarangan, *Faraday Discuss.* **2015**, *178*, 357.
[200] A. Belardini, M. C. C. Larciprete, M. Centini, E. Fazio, C. Sibilia, D. Chiappe, C. Martella, A. Toma, M. Giordano, F. B. De Mongeot, *Phys. Rev. Lett.* **2011**, *107*, 1.
[201] G. L. J. A. Rikken, E. Raupach, *Nature* **1997**, *390*, 493.
[202] N. Berova, P. L. L. Polavarapu, K. Nakanishi, R. W. W. Woody, *Comprehensive Chiroptical Spectroscopy*, John Wiley & Sons, Inc., Hoboken, NJ, USA, **2012**.
[203] G. L. J. A. Rikken, E. Raupach, *Phys. Rev. E* **1998**, *58*, 5081.
[204] V. Yannopapas, A. G. Vanakaras, *ACS Photonics* **2015**, *2*, 1030.
[205] V. Yannopapas, *Solid State Commun.* **2015**, *217*, 47.
[206] S. Eslami, J. G. Gibbs, Y. Rechkemmer, J. van Slageren, M. Alarcón-Correa, T.-C. Lee, A. G. Mark, G. L. J. A. Rikken, P. Fischer, *ACS Photonics* **2014**, *1*, 1231.
[207] G. Kopnov, G. L. J. A. Rikken, *Rev. Sci. Instrum.* **2014**, *85*, 53106.
[208] D. Szaller, S. Bordács, I. Kézsmárki, *Phys. Rev. B* **2013**, *87*, 14421.
[209] Y. Okamura, F. Kagawa, S. Seki, M. Kubota, M. Kawasaki, Y. Tokura, *Phys. Rev. Lett.* **2015**, *114*, 197202.
[210] S. Tomita, K. Sawada, A. Porokhnyuk, T. Ueda, *Phys. Rev. Lett.* **2014**, *113*, 235501.
[211] A. J. J. Mastroianni, S. A. A. Claridge, A. Paul Alivisatos, A. P. Alivisatos, *J. Am. Chem. Soc.* **2009**, *131*, 8455.
[212] S. J. Tan, M. J. Campolongo, D. Luo, W. Cheng, *Nat. Nanotechnol.* **2011**, *6*, 268.
[213] J. Zhuang, H. Wu, Y. Yang, Y. C. Cao, *J. Am. Chem. Soc.* **2007**, *129*, 14166.
[214] F. Capolino, *Theory and Phenomena of Metamaterials*, CRC Press, **2009**.
[215] A. Ishimaru, S. W. Lee, Y. Kuga, V. Jandhyala, *IEEE Trans. Antennas Propag.* **2003**, *51*, 2550.
[216] J. Lekner, *Pure Appl. Opt. J. Eur. Opt. Soc. Part A* **1999**, *5*, 417.
[217] S. M. Barnett, R. P. Cameron, *J. Opt.* **2016**, *18*, 15404.
[218] J. A. A. Kong, *Electromagnetic Wave Theory*, Wiley, New York, NY, **1986**.
[219] I. V. Lindell, A. H. Sihvola, S. A. Tretyakov, A. J. Viitanen, *Electromagnetic Waves in Chiral and Bi-Isotropic Media*, Artech House, Boston, MA, **1994**.
[220] S. B. Wang, C. T. Chan, *Nat. Commun.* **2014**, *5*, 3307.
[221] C.-W. Qiu, N. Burokur, S. Zouhd, L.-W. Li, *J. Opt. Soc. Am. A, Opt. Image Sci. Vis.* **2008**, *25*, 55.
[222] S. A. Tretyakov, F. Mariotte, C. R. Simovski, T. G. Kharina, J.-P. Heliot, *IEEE Trans. Antennas Propag.* **1996**, *44*, 1006.
[223] S. S. Oh, O. Hess, *Nano Converg.* **2015**, *2*, 24.
[224] D. L. Jaggard, A. R. Mickelson, C. H. Papas, *Appl. Phys.* **1979**, *18*, 211.
[225] Y. Tang, A. E. Cohen, *Phys. Rev. Lett.* **2010**, *104*, 163901.
[226] D. M. Lipkin, *J. Math. Phys.* **1964**, *5*, 696.

[227] R. P. Cameron, S. M. Barnett, A. M. Yao, *New J. Phys.* **2012**, *14*, 53050.
[228] J. S. Choi, M. Cho, *Phys. Rev. A - At. Mol. Opt. Phys.* **2012**, *86*, 1.
[229] Y. Tang, A. E. Cohen, *Science* **2011**, *332*, 333.
[230] C. Rosales-Guzmán, K. Volke-Sepulveda, J. P. Torres, *Opt. Lett.* **2012**, *37*, 3486.
[231] M. M. Coles, D. L. Andrews, *Phys. Rev. A - At. Mol. Opt. Phys.* **2012**, *85*, 1.
[232] D. L. Andrews, M. M. Coles, *Opt. Lett.* **2012**, *37*, 3009.
[233] L. Novotny, in *Prog. Opt.* **2007**, pp. 137–184.
[234] O. Keller, *Quantum Theory of Near-Field Electrodynamics*, Springer, Berlin, Heidelberg, Gemany, **2012**.
[235] M. Schäferling, D. Dregely, M. Hentschel, H. Giessen, *Phys. Rev. X* **2012**, *2*, 31010.
[236] M. Schäferling, X. Yin, H. Giessen, *Opt. Express* **2012**, *20*, 26326.
[237] T. J. Davis, E. Hendry, *Phys. Rev. B* **2013**, *87*, 85405.
[238] N. Meinzer, E. Hendry, W. L. L. Barnes, *Phys. Rev. B* **2013**, *88*, 41407.
[239] M. Finazzi, P. Biagioni, M. Celebrano, L. Duò, *Phys. Rev. B* **2015**, *91*, 195427.
[240] Y. Liu, W. Zhao, Y. Ji, R.-Y. Wang, X. Wu, X. D. Zhang, *EPL Europhys. Lett.* **2015**, *110*, 17008.
[241] R.-Y. R. Y. Wang, P. Wang, Y. Liu, W. Zhao, D. Zhai, X. Hong, Y. Ji, X. Wu, F. Wang, D. Zhang, W. Zhang, R. Liu, X. Zhang, *J. Phys. Chem. C* **2014**, *118*, 9690.
[242] H. Zhang, A. O. Govorov, *Phys. Rev. B* **2013**, *87*, 75410.
[243] M. H. Alizadeh, B. M. Reinhard, *ACS Photonics* **2015**, *2*, 942.
[244] V. K. Valev, J. J. Baumberg, B. De Clercq, N. Braz, X. Zheng, E. J. Osley, S. Vandendriessche, M. Hojeij, C. Blejean, J. Mertens, C. G. Biris, V. Volskiy, M. Ameloot, Y. Ekinci, G. a. E. Vandenbosch, P. a. Warburton, V. V. Moshchalkov, N. C. Panoiu, T. Verbiest, *Adv. Mater.* **2014**, *26*, 4074.
[245] L. V. V. Poulikakos, P. Gutsche, K. M. M. McPeak, S. Burger, J. Niegemann, C. Hafner, D. J. J. Norris, *ACS Photonics* **2016**, *3*, 1619.
[246] V. G. Veselago, *Sov. Phys. Uspekhi* **1968**, *10*, 509.
[247] J. B. Pendry, *Phys. Rev. Lett.* **2000**, *85*, 3966.
[248] R. A. Shelby, *Science* **2001**, *292*, 77.
[249] D. R. Smith, W. J. Padilla, D. C. Vier, S. C. Nemat-Nasser, S. Schultz, *Phys. Rev. Lett.* **2000**, *84*, 4184.
[250] D. R. Smith, *Science* **2004**, *305*, 788.
[251] S. Tretyakov, I. Nefedov, A. Sihvola, S. Maslovski, C. Simovski, *J. Electromagn. Waves Appl.* **2003**, *17*, 695.
[252] J. B. B. Pendry, *Science* **2004**, *306*, 1353.
[253] R. Zhao, J. Zhou, T. Koschny, E. N. N. Economou, C. M. M. Soukoulis, *Phys. Rev. Lett.* **2009**, *103*, 103602.
[254] M. G. Silveirinha, S. I. Maslovski, *Phys. Rev. Lett.* **2010**, *105*, 189301.
[255] M. G. Silveirinha, S. I. Maslovski, *Phys. Rev. A* **2010**, *82*, 52508.
[256] R. Zhao, J. Zhou, T. Koschny, E. N. Economou, C. M. Soukoulis, *Phys. Rev. Lett.* **2010**, *105*, 189302.
[257] M. C. K. C. K. Wiltshire, J. B. B. Pendry, J. V. V. Hajnal, *J. Phys. Condens. Matter* **2009**, *21*, 292201.
[258] S. Zhang, Y. Park, J. Li, X. Lu, W. Zhang, X. Zhang, *Phys. Rev. Lett.* **2009**, *102*, 23901.
[259] E. Plum, J. Zhou, J. Dong, V. A. A. Fedotov, T. Koschny, C. M. M. Soukoulis, N. I. I. Zheludev, *Phys. Rev. B* **2009**, *79*, 35407.
[260] R. Zhao, L. Zhang, J. Zhou, T. Koschny, C. M. M. M. Soukoulis, *Phys. Rev. B* **2011**, *83*, 35105.
[261] J. Zhou, J. Dong, B. Wang, T. Koschny, M. Kafesaki, C. M. M. Soukoulis, *Phys. Rev. B* **2009**, *79*, 121104.
[262] B. Wang, J. Zhou, T. Koschny, C. M. M. Soukoulis, *Appl. Phys. Lett.* **2009**, *94*, 151112.
[263] Y.-P. Jia, Y.-L. Zhang, X.-Z. Dong, M.-L. Zheng, Z.-S. Zhao, X.-M. Duan, *Phys. E Low-dimensional Syst. Nanostructures* **2015**, *74*, 659.
[264] X. Jia, Q. Meng, C. Yuan, Z. Zhou, X. Wang, *Opt. - Int. J. Light Electron Opt.* **2016**, *127*, 5738.
[265] M. Giloan, S. Astilean, *Opt. Commun.* **2014**, *315*, 122.
[266] F. Fang, L. Gao, H. Liao, *J. Mod. Opt.* **2016**, *63*, 190.
[267] K. Song, Q. Fu, X. Zhao, *Phys. Scr.* **2011**, *84*, 35402.
[268] N. Wongkasem, A. Akyurtlu, K. A. Marx, in *2006 IEEE Antennas Propag. Soc. Int. Symp.*IEEE, Piscataway, NJ, **2006**, pp. 757–760.
[269] C. Maher-McWilliams, P. Douglas, P. F. Barker, *Nat. Photonics* **2012**, *6*, 386.
[270] D. G. Grier, *Nature* **2003**, *424*, 810.
[271] A. Ashkin, *Optical Trapping and Manipulation of Neutral Particles Using Lasers*, World Scientific, Singapore, **2006**.
[272] J. Chen, J. Ng, Z. Lin, C. T. Chan, *Nat. Photonics* **2011**, *5*, 531.
[273] M. R. Dennis, K. O'Holleran, M. J. Padgett, in *Prog. Opt.*, Elsevier B.V., **2009**, pp. 293–363.
[274] A. Dogariu, S. Sukhov, J. Sáenz, *Nat. Photonics* **2012**, *7*, 24.
[275] A. Hayat, J. P. B. Mueller, F. Capasso, *Proc. Natl. Acad. Sci. USA* **2015**, *112*, 13190.
[276] P. C. Chaumet, A. Rahmani, *Opt. Express* **2009**, *17*, 2224.
[277] H. Chen, Y. Jiang, N. Wang, W. Lu, S. Liu, Z. Lin, *Opt. Lett.* **2015**, *40*, 5530.
[278] D. S. Bradshaw, D. L. Andrews, *New J. Phys.* **2014**, *16*, 103021.
[279] R. P. Cameron, S. M. Barnett, A. M. Yao, *New J. Phys.* **2014**, *16*, 13020.
[280] G. Tkachenko, E. Brasselet, *Nat. Commun.* **2014**, *5*, 3577.
[281] A. Canaguier-Durand, C. Genet, *J. Opt.* **2016**, *18*, 15007.
[282] A. Canaguier-Durand, J. A. Hutchison, C. Genet, T. W. Ebbesen, *New J. Phys.* **2013**, *15*, 123037.
[283] M. H. Alizadeh, B. M. Reinhard, *ACS Photonics* **2015**, *2*, 361.
[284] M. H. Alizadeh, B. M. Reinhard, *ACS Photonics* **2015**, *2*, 1780.
[285] K. Toyoda, K. Miyamoto, N. Aoki, R. Morita, T. Omatsu, *Nano Lett.* **2012**, *12*, 3645.
[286] V. K. Valev, D. Denkova, X. Zheng, A. I. Kuznetsov, C. Reinhardt, B. N. Chichkov, G. Tsutsumanova, E. J. Osley, V. Petkov, B. De Clercq, A. V. Silhanek, Y. Jeyaram, V. Volskiy, P. A. Warburton, G. A. E. Vandenbosch, S. Russev, O. A. Aktsipetrov, M. Ameloot, V. V. Moshchalkov, T. Verbiest, *Adv. Mater.* **2012**, *24*, OP29.
[287] M. Kauranen, A. V. Zayats, *Nat. Photonics* **2012**, *6*, 737.
[288] T. Petralli-Mallow, T. M. Wong, J. D. Byers, H. I. Yee, J. M. Hicks, *J. Phys. Chem.* **1993**, *97*, 1383.
[289] S. Foerier, I. A. Kolmychek, O. A. Aktsipetrov, T. Verbiest, V. K. Valev, *ChemPhysChem* **2009**, *10*, 1431.
[290] R. W. Boyd, *Nonlinear Optics, 3rd Edition*, Academic Press, San Diego, CA **2008**.
[291] V. K. Valev, *Langmuir* **2012**, *28*, 15454.
[292] R. C. Powell, *Symmetry, Group Theory, and the Physical Properties of Crystals*, Springer New York, New York, NY, **2010**.
[293] T. Verbiest, K. Clays, V. Rodriguez, *Second-Order Nonlinear Optical Characterization Techniques: An Introduction*, CRC Press, Boca Raton, FL, **2009**.
[294] M. Kauranen, T. Verbiest, A. Persoons, *J. Mod. Opt.* **1998**, *45*, 403.
[295] M. Kauranen, T. Verbiest, J. J. Maki, A. Persoons, *J. Chem. Phys.* **1994**, *101*, 8193.
[296] V. K. Valev, A. V. Silhanek, N. Verellen, W. Gillijns, P. Van Dorpe, O. A. Aktsipetrov, G. A. E. Vandenbosch, V. V. Moshchalkov, T. Verbiest, *Phys. Rev. Lett.* **2010**, *104*, 127401.
[297] S. Sioncke, T. Verbiest, A. Persoons, *Mater. Sci. Eng. R Rep.* **2003**, *42*, 115.
[298] J. J. Maki, T. Verbiest, M. Kauranen, S. Van Elshocht, A. Persoons, *J. Chem. Phys.* **1996**, *105*, 767.
[299] J. D. Byers, H. I. Yee, J. M. Hicks, *J. Chem. Phys.* **1994**, *101*, 6233.
[300] V. K. Valev, A. V. Silhanek, N. Smisdom, B. De Clercq, W. Gillijns, O. A. Aktsipetrov, M. Ameloot, V. V. Moshchalkov, T. Verbiest, *Opt. Express* **2010**, *18*, 8286.

[301] C. Zhang, Z.-Q. Li, X. Yang, Z. Chen, Z. Wang, *AIP Adv.* **2016**, *6*, 125014.
[302] C. Steuwe, C. F. Kaminski, J. J. Baumberg, S. Mahajan, *Nano Lett.* **2011**, *11*, 5339.
[303] P. Fischer, K. Beckwitt, F. W. Wise, A. C. Albrecht, *Chem. Phys. Lett.* **2002**, *352*, 463.
[304] P. Fischer, F. Hache, *Chirality* **2005**, *17*, 421.
[305] M. I. Stockman, D. J. Bergman, C. Anceau, S. Brasselet, J. Zyss, *Phys. Rev. Lett.* **2004**, *92*, 57402.
[306] B. Canfield, S. Kujala, K. Jefimovs, J. Turunen, M. Kauranen, *Opt. Express* **2004**, *12*, 5418.
[307] V. K. Valev, N. Smisdom, A. V. Silhanek, B. De Clercq, W. Gillijns, M. Ameloot, V. V. Moshchalkov, T. Verbiest, *Nano Lett.* **2009**, *9*, 3945.
[308] V. K. Valev, A. V. Silhanek, Y. Jeyaram, D. Denkova, B. De Clercq, V. Petkov, X. Zheng, V. Volskiy, W. Gillijns, G. A. E. Vandenbosch, O. A. Aktsipetrov, M. Ameloot, V. V. Moshchalkov, T. Verbiest, *Phys. Rev. Lett.* **2011**, *106*, 226803.
[309] V. K. Valev, W. Libaers, U. Zywietz, X. Zheng, M. Centini, N. Pfullmann, L. O. Herrmann, C. Reinhardt, V. Volskiy, A. V. Silhanek, B. N. Chichkov, C. Sibilia, G. a. E. Vandenbosch, V. V. Moshchalkov, J. J. Baumberg, T. Verbiest, *Opt. Lett.* **2013**, *38*, 2256.
[310] V. K. Valev, B. De Clercq, C. G. Biris, X. Zheng, S. Vandendriessche, M. Hojeij, D. Denkova, Y. Jeyaram, N. C. Panoiu, Y. Ekinci, A. V. Silhanek, V. Volskiy, G. A. E. Vandenbosch, M. Ameloot, V. V. Moshchalkov, T. Verbiest, *Adv. Mater.* **2012**, *24*, OP208.
[311] V. K. Valev, A. V. Silhanek, B. De Clercq, W. Gillijns, Y. Jeyaram, X. Zheng, V. Volskiy, O. A. Aktsipetrov, G. A. E. Vandenbosch, M. Ameloot, V. V. Moshchalkov, T. Verbiest, *Small* **2011**, *7*, 2573.
[312] V. K. Valev, B. D. Clercq, X. Zheng, D. Denkova, E. J. Osley, S. Vandendriessche, A. V. Silhanek, V. Volskiy, P. A. Warburton, G. A. E. Vandenbosch, M. Ameloot, V. V. Moshchalkov, T. Verbiest, *Opt. Express* **2012**, *20*, 256.
[313] M. J. Huttunen, G. Bautista, M. Decker, S. Linden, M. Wegener, M. Kauranen, *Opt. Mater. Express* **2011**, *1*, 46.
[314] J. W. W. Jarrett, M. Chandra, K. L. L. Knappenberger, *J. Chem. Phys.* **2013**, *138*, 214202.
[315] J. W. Jarrett, P. J. Herbert, S. Dhuey, A. M. Schwartzberg, K. L. Knappenberger, *J. Phys. Chem. A* **2014**, *118*, 8393.
[316] G. Bautista, M. Kauranen, *ACS Photonics* **2016**, *3*, 1351.
[317] N. Abdulrahman, C. D. Syme, C. Jack, A. Karimullah, L. D. Barron, N. Gadegaard, M. Kadodwala, *Nanoscale* **2013**, *5*, 12651.
[318] H. Su, Y. Guo, W. Gao, J. Ma, Y. Zhong, W. Y. Tam, C. T. Chan, K. S. Wong, *Sci. Rep.* **2016**, *6*, 22061.
[319] R. B. Davidson, J. I. I. Ziegler, G. Vargas, S. M. M. Avanesyan, Y. Gong, W. Hess, R. F. Haglund, R. B. Davidson II, J. I. I. Ziegler, G. Vargas, S. M. M. Avanesyan, Y. Gong, W. Hess, R. F. Haglund Jr., *Nanophotonics* **2015**, *4*, 108.
[320] S. P. Rodrigues, S. Lan, L. Kang, Y. Cui, W. Cai, *Adv. Mater.* **2014**, *26*, 6157.
[321] R. Kolkowski, L. Petti, M. Rippa, C. Lafargue, J. Zyss, *ACS Photonics* **2015**, *2*, 899.
[322] L. Kang, S. Lan, Y. Cui, S. P. Rodrigues, Y. Liu, D. H. Werner, W. Cai, *Adv. Mater.* **2015**, *27*, 4377.
[323] T. Verbiest, M. Kauranen, Y. Van Rompaey, A. Persoons, *Phys. Rev. Lett.* **1996**, *77*, 1456.
[324] T. Verbiest, M. Kauranen, A. Persoons, *J. Opt. Soc. Am. B* **1998**, *15*, 451.
[325] M. Kauranen, S. Van Elshocht, T. Verbiest, A. Persoons, S. Van Elshocht, T. Verbiest, A. Persoons, *J. Chem. Phys.* **2000**, *112*, 1497.
[326] S. Sioncke, S. Van Elshocht, T. Verbiest, A. Persoons, M. Kauranen, K. E. S. Phillips, T. J. Katz, *J. Chem. Phys.* **2000**, *113*, 7578.
[327] M. J. Huttunen, M. Erkintalo, M. Kauranen, *J. Opt. A Pure Appl. Opt.* **2009**, *11*, 34006.
[328] M. J. Huttunen, M. Virkki, M. Erkintalo, E. Vuorimaa, A. Efimov, H. Lemmetyinen, M. Kauranen, *J. Phys. Chem. Lett.* **2010**, *1*, 1826.
[329] E. A. Mamonov, T. V. Murzina, I. A. Kolmychek, A. I. Maydykovsky, V. K. Valev, A. V. Silhanek, E. Ponizovskaya, A. Bratkovsky, T. Verbiest, V. V. Moshchalkov, O. A. Aktsipetrov, *Opt. Lett.* **2011**, *36*, 3681.
[330] E. A. Mamonov, T. V. Murzina, I. A. Kolmychek, A. I. Maydykovsky, V. K. Valev, A. V. Silhanek, T. Verbiest, V. V. Moshchalkov, O. A. Aktsipetrov, *Opt. Express* **2012**, *20*, 8518.
[331] E. A. Mamonov, I. A. Kolmychek, S. Vandendriessche, M. Hojeij, Y. Ekinci, V. K. Valev, T. Verbiest, T. V. Murzina, *Phys. Rev. B* **2014**, *89*, 121113.
[332] S. P. Rodrigues, Y. Cui, S. Lan, L. Kang, W. Cai, *Adv. Mater.* **2015**, *27*, 1124.
[333] S. Chen, F. Zeuner, M. Weismann, B. Reineke, G. Li, V. K. Valev, K. W. Cheah, N. C. Panoiu, T. Zentgraf, S. Zhang, *Adv. Mater.* **2016**, *28*, 2992.
[334] S. Chen, G. Li, F. Zeuner, W. H. Wong, E. Y. B. Pun, T. Zentgraf, K. W. Cheah, S. Zhang, *Phys. Rev. Lett.* **2014**, *113*, 33901.
[335] K. Sato, K. Takanashi, K. Himi, A. Kirilyuk, T. Rasing, *J. Magn. Magn. Mater.* **2002**, *239*, 351.
[336] M. Nývlt, F. Bisio, J. Franta, C. L. Gao, H. Petek, J. Kirschner, *Phys. Rev. Lett.* **2005**, *95*, 127201.
[337] Q. Y. Jin, H. Regensburger, R. Vollmer, J. Kirschner, *Phys. Rev. Lett.* **1998**, *80*, 4056.
[338] V. K. Valev, A. Kirilyuk, F. Dalla Longa, J. T. Kohlhepp, B. Koopmans, T. Rasing, *Phys. Rev. B* **2007**, *75*, 12401.
[339] V. K. Valev, M. Gruyters, A. Kirilyuk, T. Rasing, *Phys. Status Solidi* **2005**, *242*, 3027.
[340] S. Vandendriessche, V. K. Valev, T. Verbiest, *Appl. Opt.* **2012**, *51*, 209.
[341] O. A. Aktsipetrov, *Colloids Surfaces A Physicochem. Eng. Asp.* **2002**, *202*, 165.
[342] W. Zheng, X. Liu, A. T. Hanbicki, B. T. Jonker, G. Lüpke, *Opt. Mater. Express* **2015**, *5*, 2597.
[343] V. K. Valev, A. V. Silhanek, W. Gillijns, Y. Jeyaram, H. Paddubrouskaya, A. Volodin, C. G. Biris, N. C. Panoiu, B. De Clercq, M. Ameloot, O. A. Aktsipetrov, V. V. Moshchalkov, T. Verbiest, *ACS Nano* **2011**, *5*, 91.
[344] V. K. Valev, *Opt. Photonics News* **2016**, *27*, 34.
[345] B. K. Canfield, S. Kujala, K. Laiho, K. Jefimovs, J. Turunen, M. Kauranen, *Opt. Express* **2006**, *14*, 950.